PLASMONIC NANOSENSORS FOR IMPROVING THE SENSITIVITY OF SURFACE ENHANCED RAMAN SPECTROSCOPY

A Dissertation

Presented to

the Faculty of the Department of Electrical and Computer Engineering

University of Houston

In Partial Fulfillment

of the Requirements for the Degree

Doctor of Philosophy

in Electrical Engineering

by

Pratik Motwani

May 2015

PLASMONIC NANOSENSORS FOR IMPROVING THE SENSITIVITY OF SURFACE ENHANCED RAMAN SPECTROSCOPY

Pratik I Motwani

Approved:

Chair of the Committee
John.C. Wolfe, Professor,
Electrical and Computer Engineering

Co-chair of the Committee
Wei-chuan Shih, Assistant Professor,
Electrical and Computer Engineering

Committee Members:

Lowell.T. Wood, Professor,
Department of Physics

Jiming Bao, Associate Professor,
Electrical and Computer Engineering

Cunjiang Yu, Assistant Professor,
Mechanical Engineering

Suresh Khator, Associate Dean,
Cullen College of Engineering

Badri Roysam, Professor and Chair,
Electrical and Computer Engineering

Acknowledgements

The following dissertation could not have been accomplished without the persistent support of Dr. John Wolfe and Dr. Wei-Chuan Shih. I will always respect Dr. Wolfe for his immense diligence towards research and helping his students achieve success. I would also like to thank Dr. Shih without whom, I would not have been able to apply my ideas and value them the way he has done throughout my degree program. I thank my committee members - Dr. Lowell Wood, Dr. Jiming Bao, and Dr. Cunjiang Yu for their patience and critical assessment of this dissertation. I would like to thank the present and past members of the group at Nanosystem Manufacturing Center (NMC) – Sri Charan Vemula, Hongjie Guo, Mufaddal Gheewala, Ji Qi, Szu-te Lin, Sumit Abhichandani, and Apeksha Awale.

My PhD journey has been a long one and would not have been an enjoyable experience without the unchanging moral support of my roommates, Sumit Abhichandani and Swapnil Chandratre and friends, Apeksha Awale, Mufaddal Gheewala, and Sri Charan Vemula.

I would like to dedicate this dissertation to my parents, Inder Motwani and Beena Motwani, without whom I would not have been here. Their consistent love, patience and prayers has encouraged me to finish this journey successfully.

PLASMONIC NANOSENSORS FOR IMPROVING THE SENSITIVITY OF SURFACE ENHANCED RAMAN SPECTROSCOPY

An Abstract

of a

Dissertation

Presented to

the Faculty of the Department of Electrical and Computer Engineering

University of Houston

In Partial Fulfillment

of the Requirements for the Degree

Doctor of Philosophy

in Electrical Engineering

by

Pratik Motwani

May 2015

Abstract

Over the past four decades, the development of advanced techniques for fabricating metallic nanostructures has reinvigorated interest in using surface-enhanced Raman spectroscopy (SERS) for practical applications in molecular sensing and chemical compositional analysis. Although numerous SERS substrates have been reported, most lack the reproducibility, structural uniformity, high density of strong field regions-*hot spots,* large active area, and low cost required for applications. In this work, SERS substrates that address these issues are developed and characterized.

One of the earliest and simplest SERS substrate was evaporated Au/Ag nano-islands on glass substrates. However, the adhesion of these nano-islands is poor, particularly in aqueous environments. We showed that the use of sputter-deposition, instead of evaporation, provides reliable adhesion and, additionally, a practical way to control nucleation and film growth. By optimizing process conditions, we were able to induce nano-gaps in the films, which are known to be associated with a strong SERS response. In this work, through correlation between the process conditions, film morphology and SERS response, we have been able to obtain enhancement factors (EF) of 5 million, 5 times higher than the best evaporated films.

More recently, nanoporous gold (NPG), a bicontinuous 3-D porous gold structure formed by free corrosion of Au/Ag alloys, has generated considerable interest as a SERS substrate. NPG features a high density of hot spots and a tunable plasmon resonance. The structural evolution of NPG/Au bilayer films and its effects on SERS intensity were

studied in detail. By optimizing pore structure, we were able to increase EF by a factor of 6 over the state-of-the-art; a 75-fold increase was achieved by optimizing the gold-layer thickness. Patterning the NPG film into sub-wavelength disk shaped structures (NPGDs) produces EFs as high as 500 million.

Finally, NPG and patterned gold sensors were formed on optical fiber substrates to explore plasmonics on optical fibers for remote sensing applications. In the first approach, NPG was deposited on fibers with cylindrical and tapered ends. In the second, periodic arrays of gold sensors were fabricated using ion beam proximity lithography, a high throughput approach where many fibers can be patterned simultaneously.

Table of Contents

List of Figures

List of Tables

Chapter 1 - Introduction

1.1 Motivation

Plasmonics is a growing field that circumvents the diffraction limit of light by trapping, manipulating and amplifying light in nanoscale regions. Surface enhanced Raman spectroscopy (SERS) is one of the most significant optical applications of plasmonics because it provides a minimally invasive and multiplexed detection platform that can prove to be very significant for the development of next generation of bio-molecular sensors. In simple terms, SERS is a combination of specifically two fields: *(1) Vibrational Raman spectroscopy and (2) Plasmonics or optical properties of noble metals.* The high enhancement of the Raman signal observed in SERS is due to the high field intensity experienced by a molecule when it is placed in the vicinity of a metallic nanostructure. Spectroscopists call these high intensity regions *hot spots*. The figure of merit of a SERS substrate is enhancement factor (EF), defined as the ratio of the Raman signal experienced by the molecule attached to the metallic nanostructure and the molecule isolated when the incident field strength and wavelength is the same. Although the significance of SERS has been known for almost four decades now, its applications has been limited partly by the lack of available substrates that can provide uniform and reproducible SERS signal intensity over large areas. In recent years, there have been numerous reports [1-5] of SERS substrates that can exhibit very high enhancements of the order of 10^{14}-10^{15}, but the occurrence of this high enhancement is local and extremely rare. These substrates do not exhibit high average enhancements or high enhancements over large areas and thus are used for fundamental studies and are not suited for practical

applications. Hence, the motivation of this work was to develop a new generation of nanostructured substrates that exhibit a high density of *hot spots* over large areas.

Chapter 2 - Surface Enhanced Raman Scattering

2.1 Raman Scattering

Raman scattering is an inelastic type of scattering process between a photon and a scattering molecule typically mediated by the vibration of the molecule. This scattering effect was first experimentally observed by an Indian physicist Sir C.V. Raman in 1928 [13] using sunlight as an optical source, a telescope, color filters and observer's eye as the detector.

2.1.1 Classical Description

In the classical description of Raman scattering, light is considered to be an electromagnetic wave with an oscillating field which when interacts with a molecule causes electrons and nuclei to be displaced. This induces an electric dipole moment in the molecule through its polarizability. Polarizability is determined by the electron cloud's ability to interact with an electric field. As a result, the molecule can radiate at the frequency of the incident light. However, sometimes the molecule can radiate at frequencies shifted from the incident light's frequency. The field strength at these shifted frequencies is extremely weak. Thus, for several decades after the discovery of Raman scattering, the effect could be only observed for molecules in highly concentrated and pure solvents. Some molecules tend to exhibit stronger Raman signals while some tend to be weak. Soft molecules like benzene are considered to be strong Raman scatterers and hard molecules like water are considered to be weak Raman scatterers.

The strength of the dipole moment induced during the light-matter interaction is given by

$$\mu = \alpha E, \tag{1}$$

where α is the polarizability and E is is the strength of the electric field for an incident beam of light. The strength of the electric field can then be expressed as [6]

$$E = E_0 \cos(\vartheta_0 t), \tag{2}$$

where ϑ_0 is the frequency of the incident wave. If a molecule interacts with an electromagnetic field, the transfer of energy from the field to the molecule occurs only when Bohr's frequency condition is satisfied.

The polarizability of the molecule is not constant and it changes with different molecular vibrations. The polarizability however is a function of the instantaneous position of the atoms. Thus, considering the physical displacement of atoms, the polarizability can be approximated using Taylor series expansion. After applying some trigonometric identities with the Taylor series expansion, the strength of the induced dipole moment becomes[6]

$$\mu = \alpha_0 E_0 \cos(2\pi\vartheta_0 t) + \frac{\partial\alpha}{2\partial Q} . E_0 . Q_0 \{\cos[2\pi(\vartheta_0 - \vartheta_{vbr})t] + \cos[2\pi(\vartheta_0 + \vartheta_{vbr})t]\}, \tag{3}$$

where ϑ_{vbr} is the molecular vibration frequency and Q_0 is the vibrational intensity.

Thus from the above equation, we can see that the induced dipole moment radiates at three distinct frequencies which results in the scattered light at these three frequencies. The two shifted frequencies are symmetric with respect to the incident

frequency or ϑ_0, the first frequency component. The first frequency component indicates the elastically scattered process or Rayleigh frequency, while the other two shifted frequencies indicate the inelastically scattered process or the Raman frequencies. The down-shifted frequency or the incident minus the molecular vibration frequency $\vartheta_0 - \vartheta_{vbr}$ is termed as Stokes scattering while the up-shifted or the incident frequency plus the molecular vibration frequency $\vartheta_0 + \vartheta_{vbr}$ is termed as Anti-stokes scattering.

The polarizability, responsible for the intensity of Raman scattered radiation must change in order for the molecule to be a Raman active molecule. This means that the electron cloud of the scattering molecule must change during the vibration. This is considered to be the Raman selection rule. It means that the fundamental vibrational mode of the scattering molecule would be Raman active if the value $\frac{\partial \alpha}{\partial Q} \neq 0$. The Raman scattering cross-section is inversely proportional to the excitation wavelength and can be written mathematically as [6]

$$\sigma \propto \frac{1}{\lambda^4}. \tag{4}$$

If a molecule has a center of symmetry like CO_2 or N_2, it will be Raman active and IR inactive. To summarize, classical mechanics states that Raman effect will occur when a beam of monochromatic light impinges upon a molecule causing a perturbation of its electron cloud and this excites the molecule to a higher vibrational energy state than its ground state or to its first electronic state if there is resonance.

2.1.2 Quantum Description

As we have seen earlier, at the core of Raman scattering lies the idea that molecules vibrate when light is incident on them. This can be explained through a very simple analogy. The atoms in a molecule connected together by bonds can be considered analogous to balls connected by springs. Thus, it becomes apparent that when light is incident on the molecule, it will tend to vibrate. During this light-matter interaction, light can scatter elastically or inelastically from the vibrational quantum states. When an incident photon interacts with a molecule, the molecule absorbs the photon and gets excited to a virtual state, a higher energy level than the ground state but a lower energy level, than its first electronic state. The molecule immediately relaxes back to its ground state or to a higher vibrational level releasing energy in the form of a photon. Most of the scattered photons have the same energy as the energy of the incident radiation which is referred to as elastic scattering or Rayleigh scattering. However, about 1 in 10 million photons will be scattered at energies different from the energy of the incident radiation. This photon is considered to be a Raman photon and the type of scattering process is called as Raman scattering. The energy of the Raman scattered radiation will shift lower or higher depending on the interaction of the incident photon with a molecule in its ground state or its first excited state. At room temperature, molecules are mostly found in the ground state and thus the energy of the Raman scattered radiation will be lower than the incident radiation, a process called as Stokes scattering. Stokes scattering is more frequent type of Raman scattering where the lost energy is applied for the vibration of the molecules. However, sometimes if the molecule is in a higher vibrational level than the ground state, the energy of the Raman scattered radiation is higher than the incident

radiation, a process called as Anti-stokes scattering. Thus, Raman scattering can be simply thought of as a change or a shift in the vibrational energy state of a molecule due to its interaction with an incident photon. The quantum description of different light scattering events will be best explained by a Jablonski diagram shown in Figure 1.

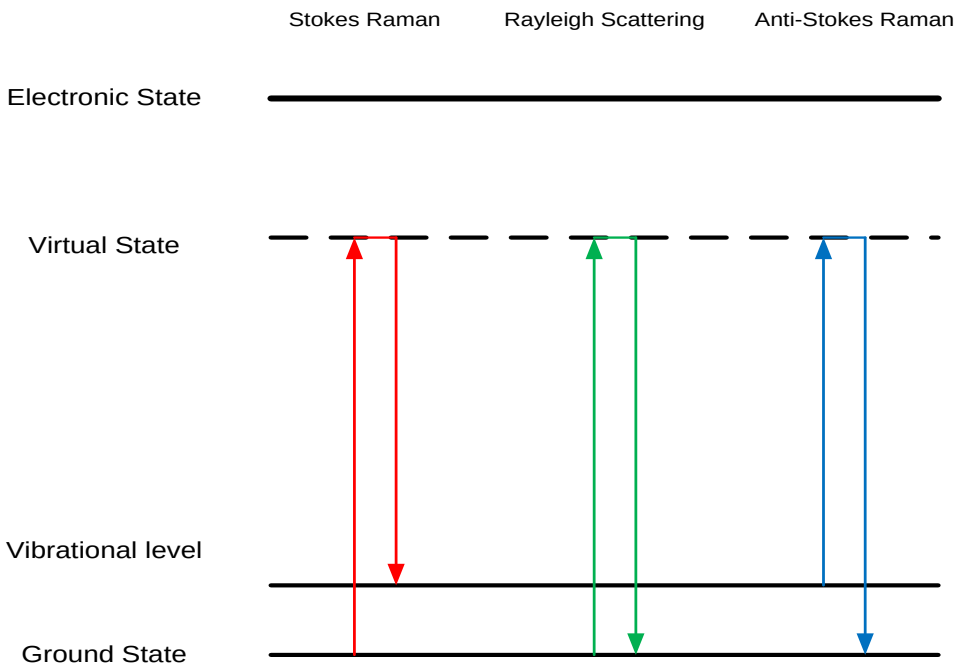

Figure 1. Jablonski Diagram showing the quantum description for Raman scattering.

Usually the amount or the number of scattered photons is proportional to the size of the bond. Organic molecules with large pi bonds tend to scatter more number of photons than molecules containing single bonds. Molecules with electron rich atoms scatter more than other molecules.

In ordinary Raman scattering, the molecule is excited to a virtual energy level which is at a lower energy level than the first electronic state as shown in the Jablonski diagram above. However, if the energy of the incident photon is similar to the difference

in the energy between the ground state of the molecule and its excited electronic state, then the molecule will be excited to its electronic state and the Raman scattering intensity will be 3 to 5 orders of magnitude higher than the normal Raman scattering intensity. This is referred to as Resonance Raman scattering, where the energy of the incident photon matches the electronic transition energy of the molecule. The difference between the energy of the incident radiation and the scattered radiation corresponds to the vibrational energy of a particular molecule. And as the Raman scattered radiation contains information about the energy of the molecular vibration, it effectively contains information about the atoms that the molecule is composed of, the chemical bonds between those atoms or the molecular structure. Therefore, a Raman spectrum is also called as a molecular fingerprint or a fingerprint spectrum. Although Raman scattering provided a high degree of unique structural information about the molecule, its applications were not explored for decades mostly due to two reasons, one was the extremely low scattering cross-section (10^{-30} – 10^{-25} cm^2) with or without the resonance condition which made the Raman scattered signal very weak. And the other reason was the existence of the much stronger fluorescence signal. With the advances in optical instrumentation technology such as lasers and with the discovery of signal enhancing mechanism like SERS [7-9], there was a reinvigorated interest in Raman scattering effect for molecular identification and composition studies. Thus SERS is sometimes also referred to as Surface enhanced "Rescued" spectroscopy.

2.1.3 Discovery of Surface Enhanced Raman Scattering (SERS)

Surface enhanced Raman scattering is one way to increase the enhancement of the Raman scattered signal. The SERS effect was first observed by Fleischmann [7] in 1974,

when they observed an enhanced Raman signal of pyridine molecules in close vicinity of an electrochemically roughened silver electrode. They attributed this enhancement to the increased surface area of the electrode and hence to a higher density of the pyridine molecules on projected surface area of the electrode.

Later on, it was shown that surface area was not the only reason for the high enhancement. This was shown by two independent researchers Van Duyne [8] and Creighton [9], where they recognized that if an assumption is made that the increase in the enhancement of the Raman scattered radiation is mainly due to a surface area increase, then the enhancement should increase only by a factor of 10. However, the enhancement observed for pyridine molecules on roughened silver electrodes was as high as 10^6. Thus, they argued that the Raman scattered radiation was enhanced not just due to an increased surface area effect but because of some unidentified mechanisms occurring close to the surface of roughened electrode.

2.2 Plasmonics and Optical Properties of Metals Suitable for SERS

2.2.1 Optical Properties of Metals Suitable for SERS

The optical properties of metals depend on the presence of free electrons in the conduction band of metals. The optical property of a material is characterized by its dielectric function ($\varepsilon(\omega)$) [15,16]. For metals, the dielectric function is complex. It is known that metals are highly reflective for frequencies up to the visible part of the spectrum and thus do not allow electromagnetic waves to propagate through them. For frequencies in the visible and the near infrared region, metals exhibit field penetration and absorption. The dielectric function of ideal metals can be modeled by a Drude free

electron model without any restoring force (no inter-band transitions and can be expressed as [6,15,16]

$$\varepsilon(\omega) = 1 - \left(\frac{{\omega_p}^2}{\omega^2 + i\gamma\omega}\right), \tag{5}$$

where ω_p is the plasma frequency and γ is the collisional frequency. Since the dielectric function is complex, it can be represented as $\varepsilon = \varepsilon_1(\omega) + i\varepsilon_2(\omega)$, where $\varepsilon_1(\omega)$ is the real part of the dielectric function and is given by

$$\varepsilon_1(\omega) = 1 - \left(\frac{{\omega_p}^2}{\omega^2 + \gamma^2}\right), \tag{6}$$

while $\varepsilon_2(\omega)$ is the imaginary part of the dielectic function and is given by

$$\varepsilon_2(\omega) = \frac{{\omega_p}^2\gamma}{\omega(\omega^2 + \gamma^2)}. \tag{7}$$

If the incident light frequency ω is lower than the plasma frequency ω_p, then the light will be reflected and Re $[\varepsilon(\omega)] < 0$ as can be clearly seen from the equation above. If the incident light frequency is higher than the plasma frequency, then light will propagate through the metal. Most metals have their plasma frequency in the ultra-violet region of the electromagnetic spectrum. However, the plasmon resonance for different metals would vary, since real metals deviate from their free electron behavior. If the light frequency is not too small, the real part of the dielectric function would be negative and the imaginary part of the dielectric function Im $[\varepsilon(\omega)]$ would be small. This would lead to numerous interesting optical effects such as plasmon resonance. The real part of the dielectric function Re $[\varepsilon(\omega)]$ is responsible for plasmon resonance while the imaginary part is responsible for dissipation. Thus, in order to obtain the highest sensitivity, the real

part of the dielectric function Re [ε (ω)] for a particular material should be large and negative, while the imaginary part of its dielectric function Im [ε (ω)] should be small at the same frequency in order to minimize the losses. For metals like gold (Au) and silver (Ag), the real part of the dielectric function is both negative and high in magnitude in the visible spectrum. This is one of the most important optical properties that make both gold and silver extremely suitable for SERS. The dielectric function for the two most common materials (Au and Ag) used for SERS is plotted as shown in Figure 2 below [15].

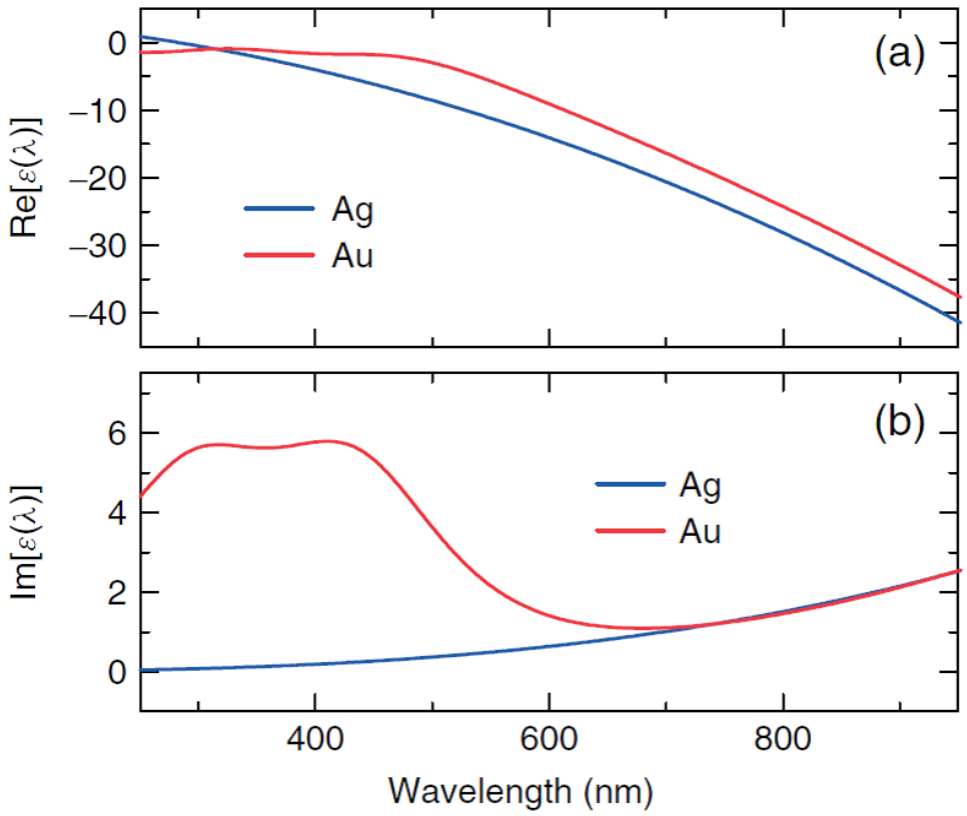

Figure 2. The real (a) and imaginary (b) parts of the dielectric function for the two most common materials used for SERS for a wavelength range of 250- 950 nm. From ref. [15].

Since the imaginary part of gold's dielectric function is high for a wavelength range of $\lambda < 600$ nm, gold exhibits strong absorption in this wavelength range, seen in Figure 2. The difference in optical properties between gold and silver arise due to the occurrence of inter-band transitions in gold. This shifts the strong light scattering for gold to longer wavelength range. Silver, on the other hand exhibits strong light scattering over the entire wavelength range. Gold has comparable optical properties to silver at longer wavelengths since the real and imaginary parts of their dielectric functions exhibit similar response to electromagnetic radiation. For SERS applications, longer wavelengths are preferred since at shorter wavelengths, strong background can interfere with the Raman scattered signal. Also, silver corrodes quickly in ambient conditions. Thus, for practical applications the choice of material depends on the chemical stability of the surface in addition to enhancement factor.

2.2.2 Plasmonics

Plasmonics [17,18] is a growing field of light-matter interactions typically light metal interactions that enable trapping, manipulating and amplifying light in nanoscale regions, far beyond the diffraction limit. Light, when incident on a metallic interface or a metallic nanostructure, causes the free electrons in the metal to oscillate with respect to the excitation frequency. These quanta of collective electron oscillations are called as *plasmons*. This interaction between the electromagnetic radiation and the free electrons in metal gives rise to a high evanescent field on or close to the metal. Thus, in simple terms plasmons are conduction electrons oscillating against the fixed background of positive ions. As described in the previous sub-section, metals that have a negative value for the real component of the dielectric function and a small value for the imaginary component

would exhibit plasmon resonance. Metals like Gold and Silver are most commonly used since they exhibit smallest imaginary component in the visible wavelength range, which would make them strong light scatterers in that range.

Raman spectroscopy, based on plasmonics, is currently one of the most significant techniques for fundamental applications in molecular diagnostics and compositional analysis. The two important types of Plasmon resonances or plasmon modes are: surface Plasmon resonance and localized surface Plasmon resonance.

2.2.2.1 Surface Plasmons

When an electromagnetic radiation or a beam of monochromatic light is incident on the interface between a metal and a dielectric, it can interact with the free electrons of the metal causing them to oscillate. These propagating collective electron oscillations are called as surface plasmons. Due to the interaction of photons with the free electrons of metal, the energy is shared between the photon and the plasmon. Thus, strictly speaking, surface plasmons exist as surface plasmon – polaritrons. In simple terms, surface plasmon-polaritrons exist at the interface between two materials that have opposite signs for the real part of their dielectric function.

Surface plasmon polaritrons exist only for TM polarization. No surface modes exist for TE polarization. In contrast to conventional waveguides, these propagating wave-like electron oscillations decay exponentially in the perpendicular direction on both metal and the dielectric side. However, the field decays much faster on the metal side due to increased damping in metals. Surface plasmon resonance occurs when this collective electron oscillation occurs at the same frequency as the incident radiation. Changes in the

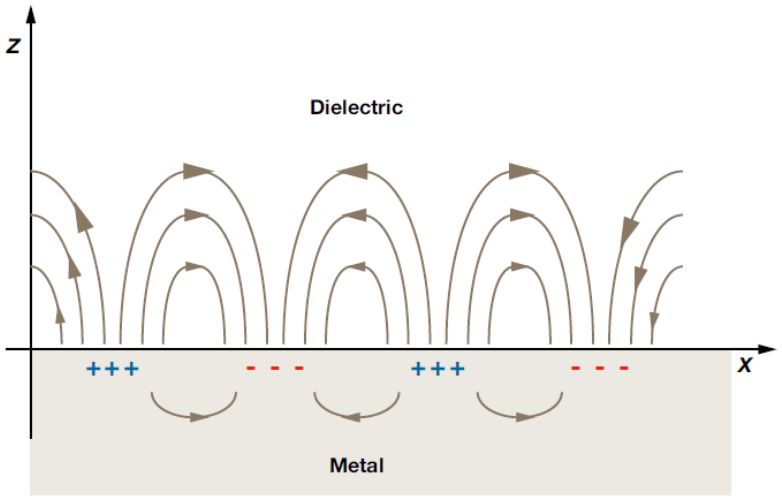

Figure 3. Schematic diagram illustrating Surface plasmon polaritron [19].

refractive index of the dielectric medium can give rise to shifts in the resonance condition which can be manifested as shifts in intensity, shifts in wavelength and shifts in the angle of reflectivity, which can be detected and then applied for various sensing applications. Metals like gold, silver, copper and aluminum exhibit plasmon resonance modes in the visible and the near infrared regions of the electromagnetic spectrum which make them interesting at optical frequencies [15,16,19]. However, gold and silver are most commonly used since they exhibit surface plasmon charge density waves at lower losses than other materials at optical frequencies.

2.2.2.2 Localized Surface Plasmons

Localized surface plasmons are non-propagating coherent charge density oscillations confined near a metallic nano-structure. When light is incident on a metallic nanostructure which consists of heavier positive ions and electrons, it can induce polarization between the conduction band electrons and the positive ions, since the electrons start to displace against the background of fixed positive ions under the

influence of the electric field. This results into the formation of electric dipoles. Localized surface Plasmon resonance occurs when the collective coherent oscillation of the conduction electrons is in resonance with the excitation wavelength. In case of a metallic nanosphere, the curved surface of the particle causes a restoring force that allows resonance to occur at a particular resonant frequency. This causes an enhanced field inside the nanosphere and an enhanced dipolar field outside but very close to the nanosphere surface [20]. The enhanced field gives rise to an enhanced scattering of light and also causes enhanced local electromagnetic field around the nanoparticle or the nano-structure. The enhancement in the field achieved in this way serves as the basis of explaining the intensity enhancement obtained for surface enhanced Raman spectroscopy as well as for other surface enhanced analytical techniques. The frequency and the intensity of these local field enhancements however is dependent on the size and shape distribution of the nano-structure, the type of the material as well as the medium surrounding the structure. Noble metal nanoparticles of gold and silver exhibit least losses in the visible region of the spectrum as discussed earlier and since they have their scattering resonance in the same wavelength range, they are explored the most for surface enhanced spectroscopic techniques. The light-nanoparticle interaction can be understood using a simple quasi-static approximation when the particle size (d) is much smaller than the incident wavelength of light (λ), i.e., $d << \lambda$ [21].

The electric field induced in the metal can be given as

$$E_{in} = \left(\frac{3\varepsilon_m}{\varepsilon + 2\varepsilon_m}\right) \times E_0 \,, \tag{8}$$

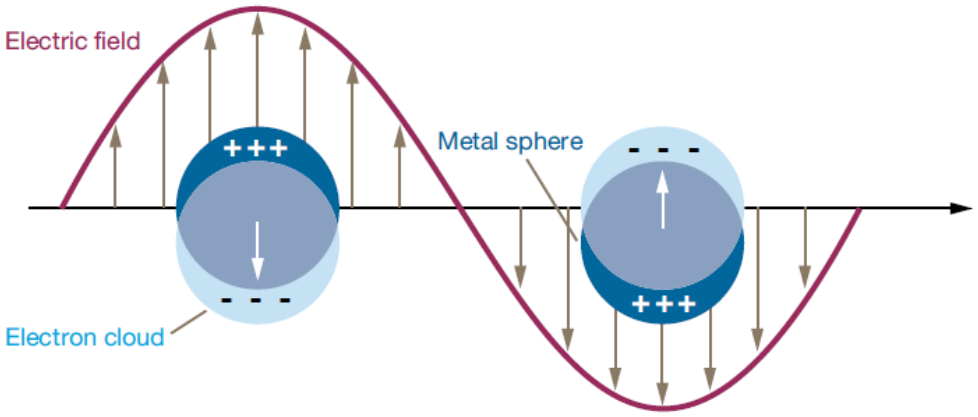

Figure 4. Schematic diagram illustrating localized surface plasmon [19].

where E_0 is the incident electric field, ε is the dielectric function of the particle and ε_m is the dielectric constant of the surrounding medium.

It is apparently seen that the resonance condition will occur when $|\varepsilon + 2\varepsilon_m|$ is minimum which simplifies to

$$Re[\varepsilon(\omega)] = -2\varepsilon_m \,. \tag{9}$$

For a metallic sphere following the drude model of the dielectric function, this will correspond to the frequency$\omega_0 = \frac{\omega_p}{\sqrt{3}}$.

Thus, the real part of the dielectric function has to be negative and equal to -2ε_m to establish a resonance condition, while the imaginary part of the dielectric function should be small at a certain wavelength so as to minimize absorption losses in the metal.

As described earlier, gold exhibits higher absorption losses for the excitation wavelength λ< 600 nm. This exists due to the occurrence of an interband transition for

Gold at ~470 nm. Silver, on the other hand exhibits least amount of losses than any other metal but it exhibits poorer stability due to sulfur and chlorine corrosion when exposed to the environment. Both silver and gold exhibit strong light scattering in the near infrared region of the electromagnetic spectrum. Higher excitation wavelengths are preferable than shorter wavelengths due to strong fluorescence in the shorter wavelength regimes [15,16,19].

2.3 Applications of SERS

Recently, it was shown that in the $5.9 billion molecular spectroscopy market, surface enhanced Raman spectroscopy would grow at the fastest rate over the next decade. SERS is one of the emerging analytical techniques because of its ability in providing unique identification as well as detailed composition along with structural information down to a single molecule level [1-5]. SERS provides a label free and a minimally invasive multiplexed detection platform for the development of next generation of molecular and bio sensing devices. Therefore, SERS is, and can be applied in various applications involving molecular sensing, arts [27-29], biochemistry, bio sensing [31], in-vivo [24] as well as in-vitro glucose monitoring [22,23], tissue imaging [30], chemical warfare agents [25], highly sensitive detection of chemicals i.e. detection of extremely low concentrations, trace detection and compositional analysis of drugs, contaminations [26] etc.

2.4 Mechanisms of SERS

As mentioned before, Raman scattered signal is extremely weak due to its small scattering cross-section compared to Rayleigh scattered light and the light that fluoresce.

However, Raman scattering when combined with the plasmonics of metallic nanostructures can provide significant enhancement in the signal. This offers an opportunity for exploring the wide range of applications of Raman spectroscopy. This new enhancing effect was observed in 1974 by Fleischmann when Raman signal for pyridine was enhanced on a roughened silver electrode and it was termed as Surface enhanced Raman scattering effect. During this time, the authors [7] interpreted the enhancement effect to be the result of increased surface area for the roughened silver electrode. However, later in 1977, two independent research groups led by Van Duyne [8] and Creihgton [9] pointed out that other enhancement mechanisms must exist that can explain increase in enhancement to 10^6 for adsorbed pyridine molecules on roughened silver electrodes. There are mainly two important mechanisms that explain the enhancements observed in SERS, electromagnetic enhancement and the chemical enhancement. After years of debate, EM enhancement was determined to be the dominant enhancement mechanism observed in SERS out of the two [6,15-19,32].

2.4.1 Electromagnetic Enhancement

When an electromagnetic wave interacts with a rough metal surface, it excites the localized surface plasmons resulting in an enhancement of both the incident as well as the Raman scattered radiation. This enhancement mechanism is referred to as Electro-magnetic enhancement of SERS and is the more dominant enhancement mechanism. The field enhancement however, occurs when the molecules are on the nano-structured metal surface or in close vicinity of the metal nano-structures. The enhancement obtained is thus dependent on the distance between the scattering molecule and the metal nanostructure and it decays as the molecule is moved away from the nanostructure. This

decay would become apparent from the equation for the induced field in a metallic nano-sphere. Electromagnetic enhancement mechanism is also dependent on the type of the material, the roughness of the nanostructure, the shape and size of the nanostructure as well as the excitation wavelength.

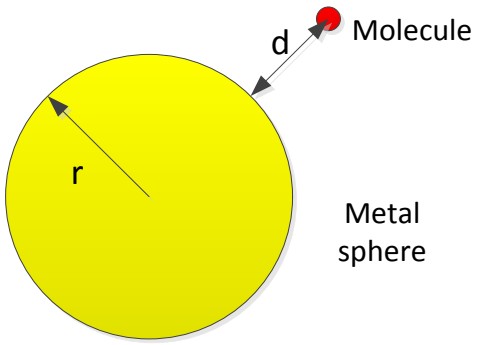

Figure 5. Schematic diagram for understanding the electromagnetic mechanism of SERS enhancements.

The electromagnetic mechanism can be easily understood by observing the field distribution for a molecule close to a simple metallic nanosphere, when irradiated by light. This is shown in the Figure 5 above. When light is incident on a molecule adsorbed on a metallic nanosphere, it causes localized charge density oscillations also called as localized surface plasmons. These oscillations then radiate a dipolar field in the metal sphere [20]. This field strength is dependent on a number of factors which basically decides the enhancements observed for SERS as well.

The dipole field [6,17] induced in the metal sphere is given as

$$E_{sp} = \left(\frac{\varepsilon - \varepsilon_0}{\varepsilon + 2\varepsilon_0}\right) \times \left(\frac{r}{r+d}\right)^3 \times E_0 \,, \tag{10}$$

where E_0 is the incident field strength,

The enhancement of the field is the ratio between the enhancement of the local field and the incident field strength [6,17]

$$E = \frac{E_m}{E_0} = \left(\frac{\varepsilon - \varepsilon_0}{\varepsilon + 2\varepsilon_0}\right) \times \left(\frac{r}{r+d}\right)^3 . \quad (11)$$

The maximum condition is obtained when the denominator in the equation tends to zero or when ε = -2ε_0. This is when the electronic transition of the plasmons is in a matched condition with the excitation wavelength. However, another necessary condition for the resonance condition to be true as mentioned earlier was the requirement for the imaginary part of the dielectric function to be small.

Now, the SERS electromagnetic enhancement factor is given by the product of the enhancement of incident and the scattered fields

$$\text{SERS EF} = |(E_{\text{incident}})|^2 \times |(E_{\text{scattered}})|^2 \quad (12)$$

$$= \left|\left(\frac{\varepsilon_i - \varepsilon_0}{\varepsilon_i + 2\varepsilon_0}\right)\right|^2 \times \left|\left(\frac{\varepsilon_s - \varepsilon_0}{\varepsilon_s + 2\varepsilon_0}\right)\right|^2 \times \left(\frac{r}{r+d}\right)^{12}.$$

Often, the shift in the frequency between the incident and the scattered radiation is very small and thus, effectively the enhancement factor scales as the fourth power of the local field enhancement. The above equation also shows that the enhancement factor is distance dependent and that the enhancement factor decays as the distance between the molecule and the nano structure (d) is increased [19,21,32].

2.4.2 Chemical Enhancement Mechanism of SERS

If the enhancements obtained for SERS could only be explained by the electromagnetic enhancement mechanism, then a strong SERS signal could have been observed for any molecule that is on or in close vicinity of the metallic nanostructure. Thus, the chemical enhancement mechanism is used to account for the enhancements that cannot be explained simply by the EM enhancement mechanism. The chemical enhancement is most commonly called as charge transfer mechanism and it requires the scattering molecule to be chemically bonded or chemisorbed to the nanostructure. This enhancement mechanism is quite independent from the electromagnetic enhancement. Molecules like CO and N_2 have different enhancements under the same experimental conditions and the difference in enhancements is significant (~200). The contribution of the chemical enhancement to the total enhancement obtained for SERS marker molecules, when adsorbed onto a metallic nanostructured substrate is usually only ~10 to 100. However, the contribution is dependent on various factors like the interaction of the bond between the adsorbed molecule and the metal substrate, the coverage of the adsorbed molecules, the electrode potential and also the metallic structure itself. The chemical enhancement mechanism can be explained by resonance Raman mechanism. The resonance Raman mechanism can occur through charge-transfer processes between the metallic nanostructure and the adsorbed molecules. Molecules that are used as SERS markers typically have their lowest electronic excitations near the ultraviolet region i.e. ~300 nm. This puts the electronic transition or the charge transfer excitation to be in the visible spectrum ~600 nm. A resonance condition would then be established if the laser excitation wavelength used is around that wavelength range (633 nm). Thus, the chemical

enhancement mechanism is a small contributor to the overall SERS enhancement effect. It is usually assumed that the contribution to the total SERS enhancement is dominated by electromagnetic enhancement [6,15-19,32].

2.5 Evolution of SERS Substrates

In simple terms, good SERS substrate is one that support plasmon resonances upon suitable excitation. SERS substrates can be classified basically in two categories; (1) Random morphology substrates that were the easiest and the first ones to be explored before the advancements in nanofabrication techniques. These substrates have random morphology and thus they lack reproducibility as well as controllability in terms of their optical response. (2) The other class is the more recent SERS substrates that are fabricated using integrated circuit nanofabrication techniques. These substrates have higher reliability in the SERS signal as well as higher controllability but they are more expensive to fabricate with a low density of hot spots.

2.5.1 Colloidal Nanoparticle and Other Random Morphology SERS Substrates

Roughened Silver electrode was one of the first to be used as a SERS substrate ultimately leading to the discovery of SERS [7,9]. It is one of the most primitive examples of a random morphology substrate. These substrates were first explored by Fleischmann [7]. However, the optical response of these substrates would change from one electrode sample to another. One such substrate is shown in Figure 6(a). Another series of random morphology substrates that generated considerable interest are the vapor phase deposited nano-islands. Evaporated nano-island films is very easy to prepare with sizes smaller than ~50 nm [36], but these films suffer from poor adhesion, even in aqueous environments, which makes them extremely complicated for testing SERS

activity. Moreover, evaporation provides narrow spatial resolution of the deposition process and thus the technique is not scalable to large areas for high manufacturing applications [19].

The second set of random morphology SERS substrates are colloidal metal nanoparticles. The most common colloidal nanoparticles used for SERS are silver and gold. Colloidal nanoparticles have been fascinating researchers for decades. These are the most common substrates for SERS applications, since they are very easily available and can achieve high local enhancements (Figure 6(b)) [57-61]. One colloidal particle however, cannot exhibit high enhancements. If we can have two particles within few nm of each other, then the enhancement can be made very high [19]. This high enhancement occurrence event is extremely rare and thus is not highly applicable, since applications require high sensitivity over the entire substrate area. Colloidal particles when laid out on a substrate, cannot exhibit high average enhancements since their density distribution of hot spots is low.

2.5.2 Lithographically Patterned Substrates

Lithographically patterned SERS substrates can provide high reproducibility and high uniformity in the SERS signal within the substrate and between different substrates. However, the enhancement of the SERS signal when averaged over the entire substrate is low, since the SERS effective area is small. Moreover, these substrates are expensive to fabricate which also limits their applications. One such substrate is shown in Figure 6(c).

2.5.3 Commercial SERS Substrates

The two most often used commercial SERS substrates are 'Klarite®' and 'Randa®' substrates. These substrates are fabricated using conventional techniques like Photo lithography, KOH etching [6], and electrochemical roughening. Klarite® substrate is as shown in Figure 6(d) and Randa® substrate is as shown in Figure 6(e). Klarite® substrate is an evaporated gold substrate coated on KOH etched inverted Silicon pyramidal structures. These structures exhibit enhancements in the order of 10^6. Since the method of fabrication is controlled, these substrates can exhibit uniform and reproducible SERS signal. However, the substrates consist of very low SERS effective areas of only 16 mm^2 that are also very expensive. On the other hand, Randa® substrates are suitable for obtaining high local enhancements and thus they can be used for trace detection of certain molecules. These substrates cannot be used for applications requiring uniform and reproducible SERS signal enhancements. Moreover, the local enhancement for Randa® substrates is only in the order of 10^6. These substrates have low stability which means that they can degrade over time and their effective sensing area is also only 16 mm^2 with a lower density of hot spots.

Thus, SERS substrates that can provide a reliable and a reproducible SERS signal along with high density of hot spots for high average enhancements need to be developed to explore the wide range of SERS applications. This was the major motivation for studies carried out on nanoporous plasmonics in this work.

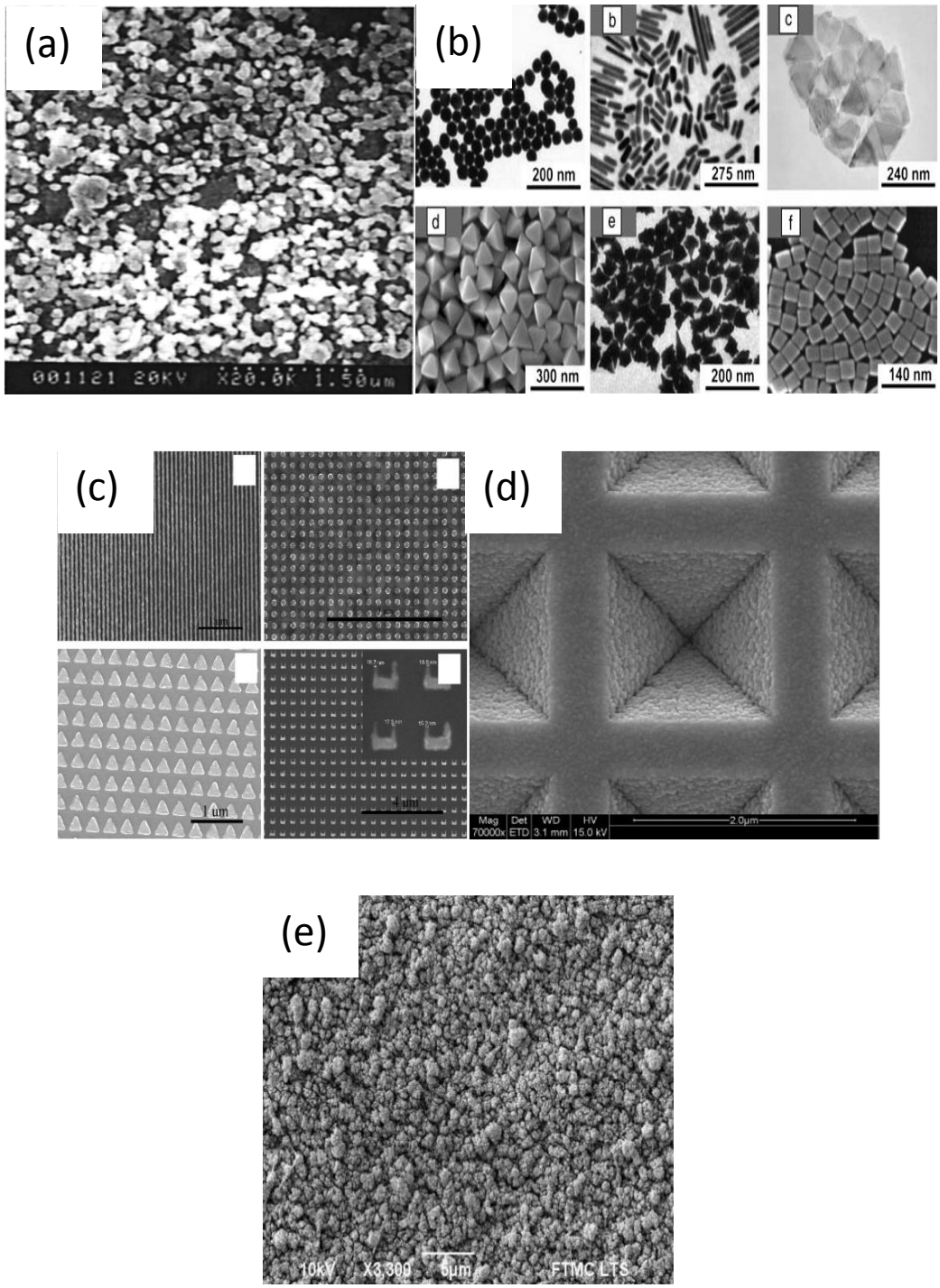

Figure 6. (a) Roughened silver electrode, (b) colloidal nanoparticles, (c) E-beam lithographically defined nanostructures, (d) Klarite® substrates, (e) Randa® substrate.

Chapter 3 - Fabrication and Characterization of SERS-Active Gold Nano-Island Substrates with High SERS Effective Area and Random Morphology

3.1 Introduction

Evaporated thin nano-island films of gold as plasmonic nanostructures have a long history that spans more than two decades. Despite comprehensive efforts by numerous research groups [35,36], reliability in obtaining high gain in the SERS signal output has still not been achieved convincingly. The evaporated gold nano-island substrates, while exhibiting throughput issues lack stability and adhesion even for solvents like water. This makes them extremely complicated to be tested for SERS activity or plasmonic properties. The adhesion and the durability of these substrates were then improved upon by employing a thin adhesion promoter layer of metal like Cr, Ti, or Ni. A thin metal adhesion layer however exhibited optical interference or damping of the signal during SERS measurements. Other research groups led by Rubinstein [35,36] started exploring few other means of improving the adhesion of the evaporated nano-islands. They improved the adhesion by thermally embedding the nano-island structures on glass substrates. This kind of thermal annealing treatment causes gold to diffuse around on the substrate thus enabling nucleation and increase in the size of the already formed islands. The thermal treatment causes an increase in the size of the island structures as well as the pitch, thus leading to changes in the optical properties as compared to the as-deposited nano-island structures. In order to alleviate the issue of adhesion, sputtering was opted over evaporation for the fabrication of thin gold nano-

island substrates. Sputtering also provides a higher control over the nucleation of gold nano-islands.

The films deposited during a sputter deposition process are highly dependent on the flux of the atoms being deposited as well as the flux of the energetic sputter gas particles. However, the flux of the condensing particles can be tweaked through two simple deposition parameters, – pressure and power. Deposition carried out at low pressure exhibit higher flux of the particles and thus continuous films, while deposition carried out at higher pressures exhibit lower flux of the particles and thus island growth. As shown earlier, SERS activity in metallic nano-structures arises at high field regions that are called as hot spots. These hot spots can be nano-scale protrusions, sharp tips, curvatures, and nano-gaps. High pressure sputtering not only gives rise to island growth but it also allows better control of the gaps between the gold nano-islands. Gold nano-islands deposited using sputtering, as an exception to the evaporated gold nano-islands; exhibit a wide range of tunability in their optical properties through simple alteration of the size of the structures and the gaps between them, while in the coating chamber. The fabrication is a single step high throughput process. Using a better approach of sputtering, the nanostructures fabricated were smaller and more uniform than the structures that can be defined using conventional lithographic techniques. The gold nano-island substrates can be tuned in order to determine the dependence of SERS on the near-field excitations, far-field excitations, the shape and sizes of the gold nano-island structures. This can be significant in order to explore these substrates for different types of SERS applications, since the fabrication method is inexpensive and less complicated.

3.2 Fabrication Methodology

3.2.1 Physical Vapor Deposition of Gold Nano Islands

Physical vapor deposition is a vapor phase deposition process wherein the desired vapor generated using physical means condenses on to a thin film. The physical means can be simply heating the desired source material with a hot filament source, electron beam or a photon beam under high vacuum conditions, or physical ejection of atoms from the source material using energetic particles. The latter is termed as Sputtering. Sputtering is simply physically dislodging atoms from a source material or a target when bombarded with energetic non-reactive ions in moderate vacuum conditions. Thus, sputtering is simply a momentum transfer process. The energetic ions are generated using a glow-discharge. The electrons when accelerated by the electric field supplied at the cathode can inelastically collide with argon gaseous atoms introduced in the vacuum coating chamber, thus leading to the generation of argon ions. This is termed as ionization caused by electron impingement. The inelastic collision between the argon gas atoms and the energetic electrons gives rise to the release of two electrons as well. This multiplication of electrons is the principle behind the sustainment of a glow-discharge. The ions formed during electron impingement are then accelerated across the cathode sheath. These energetic ions strike the surface of the target resulting into an atomic collision cascade with the ejection of recoil (a target atom). The kinetic energy with which the ions strike the surface of the target material determines the rate at which the target atoms would escape. This is called as sputter yield. Sputter yield is defined as the number of target atoms ejected per incident ion.

In addition to the ejection of a target atom, a lot of other mechanisms exist during this collision.

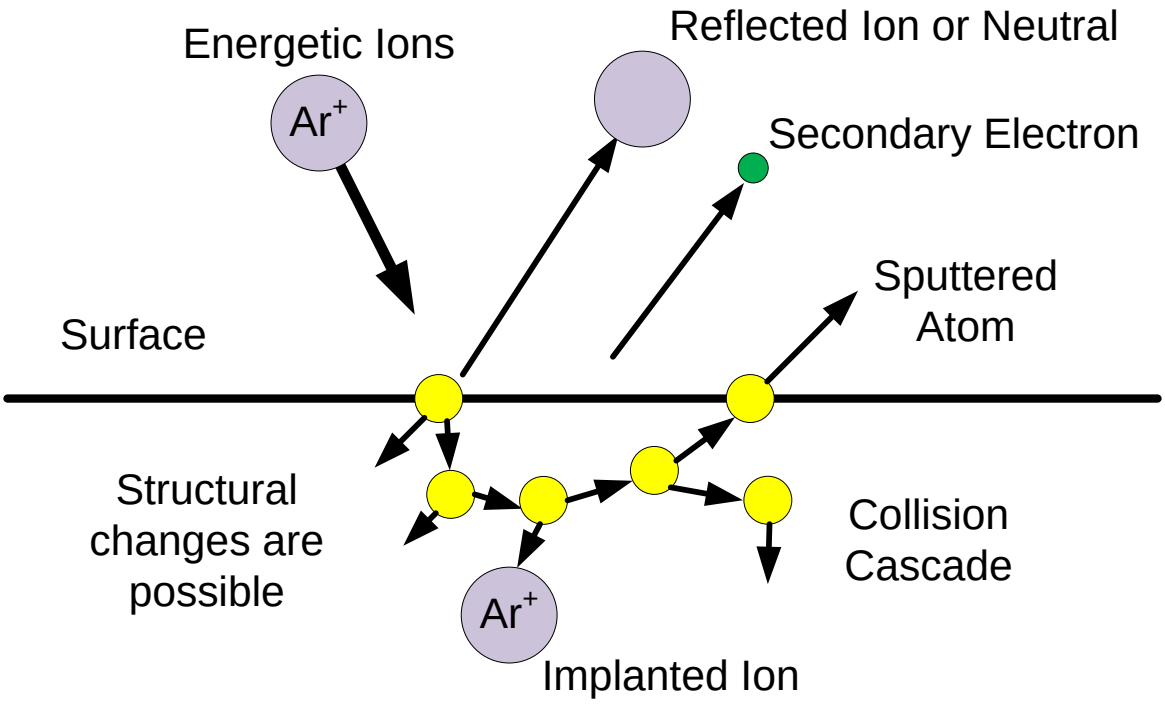

Figure 7. Interaction of energetic ions with surface.

These mechanisms are explained below:

- The ion may be reflected.
- The bombardment of the ion on the target atom might cause the ejection of an electron by the target material which will be referred to as secondary electrons, as to avoid the confusion with the already ionization enabling primary electrons. These secondary electrons are responsible for plasma sustainment as they can counter the various electron depletion processes.

- The high energy impact of ions might cause radiation damage or defects in the target material.
- The ion may also get buried into the target material or may become implanted into the target material.
- Lastly and the most important effect of the ion impact might be the physical ejection of the target atoms after going through a series of collisions. This series of collisions is called as collision cascade as shown in the above figure and the process of ejection is called as sputtering.

Subsequent ejection of the target atoms gives rise to a vapor that can ultimately condense onto the substrate forming a thin film. Since sputtering is a physical dislodgement mechanism of deposition, a reaction between the gas ions and the source material vapor can contaminate the deposited film. Thus, inert gases are opted as the sputtering gas. The choice of which inert gas to use for sputtering depends on the energy transfer ratio between colliding particles with different masses. When considering the energy transfer ratio, it is clear that an atom with a lower molecular weight than the target atom will sputter at a slower rate and sometimes might not sputter at all. Therefore, heavier gases are usually desired in order to achieve better energy transfer between the sputtering ion and the target atom and thus higher throughput. Argon is the optimal choice due to its comparable atomic weight to the target atoms, lower costs and higher availability.

A simple dc diode sputtering configuration looks something like this:

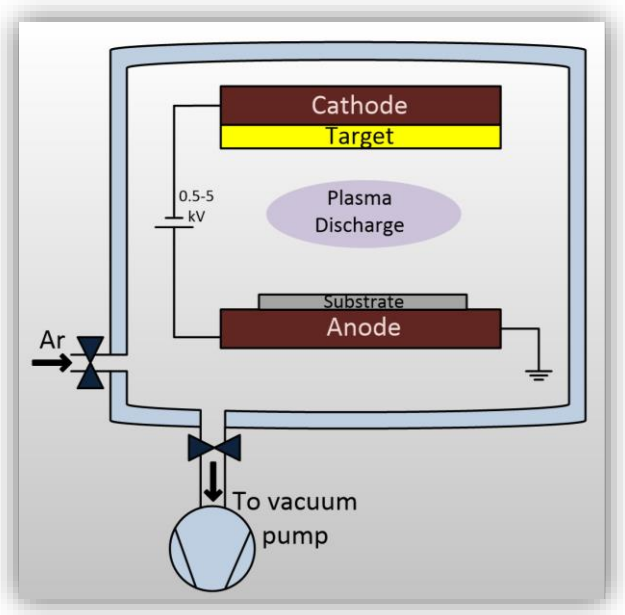

Figure 8. Schematic diagram for a DC diode sputtering system involved in the fabrication of nano-islands.

The sputter target or the material that is desired to be deposited is placed on a copper cathode (a little more than 300 mm^2 in area) supplied with a negative bias. The substrate is placed a few inches away from the target on an electrically grounded anode. This process is performed under vacuum conditions. In simple sputtering configurations, the operating pressure of the system is kept considerably high. Higher operating pressures ensure that more collisions exist between various particles (electrons, ions and neutrals) in a glow-discharge before the electrons lose their energies by colliding with the chamber walls. Thus, for diode sputtering, higher target voltage and higher operating pressure is required in order to sustain the plasma. However, diode sputtering exhibits efficient use of the target material, since the electric field is quite uniform as in a large parallel-plate capacitor. The secondary electrons that are generated during the interaction between

energetic ions and target atoms can bombard the substrate thus significantly raising the temperature of the substrate. Higher operating pressures also enable island growth since the island growth is associated with lower flux of the particles, but it also leads to lower deposition rates. Thus, gold nano-islands were deposited at an operating pressure of 100 mTorr. The current density supplied to the cathode was ~ 0.313 mA/cm^2. Additionally, the gold nano-islands fabricated using high-pressure diode sputtering are isolated units and thus they do not require any additional steps to make them discrete. Sputter deposited thin films usually exhibit smaller grain sizes. Thus, the gold nano-island films deposited using sputtering manifested higher density of island structures than evaporated nano-islands. The deposition rate and the average thickness was estimated using thicker gold films deposited under the same conditions followed by characterization using both surface profilometry as well as Scanning electron microscopy. The deposition rate was estimated to be ~10 nm/min. The gold nano-island substrates that were imaged and characterized are shown in the next section.

3.3 Results and Discussion

3.3.1 High Resolution SEM Characterization and Optical Characterization of Au Nano Island Substrates

The average deposition rate was estimated to be ~10 nm/min. Thin film growth kinetics suggest that a continuous film is formed after the coalescence stage is continued for a significant amount of time. Thus, in order to fabricate isolated gold nano-island structures, the deposition was discontinued at the island growth stage and just at the beginning of the coalescence stage. In order to study the effects of different sizes of the nano-islands on the optical properties of the substrate, gold nano-islands were deposited

at various times. Since sputtering provides a better control over the nucleation of these nano-islands, the size and the spacing between the nano-islands was manipulated in order to induce high field regions or hot spots. The average width of the gold nano-island structures and the spacing between them was estimated using 'ImageJ'. The substrates coated for the shortest time of 30 s have nano-islands with an average width in the range of 5-8 nm with spacing of ~12-14 nm in between them. Thus, using an inexpensive approach of sputtering, it was possible to fabricate structures that were smaller, uniform and denser than that could be fabricated using expensive lithographic techniques.

The surface morphology of gold nano-island structures was studied using a LEO 1525 Scanning electron microscope. The high resolution micrographs for gold nano-islands deposited at different times with different island widths are as shown below in Figure 9. To correlate the size and the pitch distribution of the gold nano-islands on SERS activity, the micrographs were binarized using ImageJ. The particles were then made significantly isolated by choosing an appropriate threshold for the in-built watershed process in ImageJ. The graph in the figure shows the size distribution.

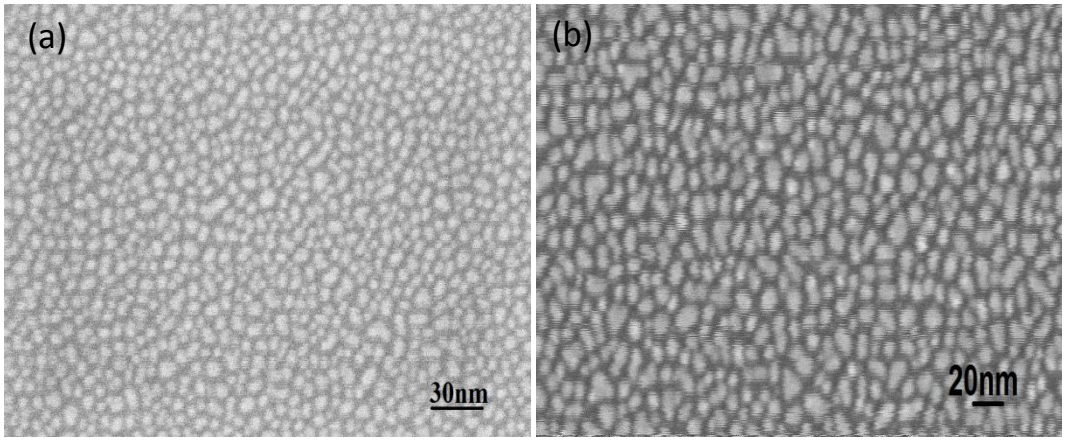

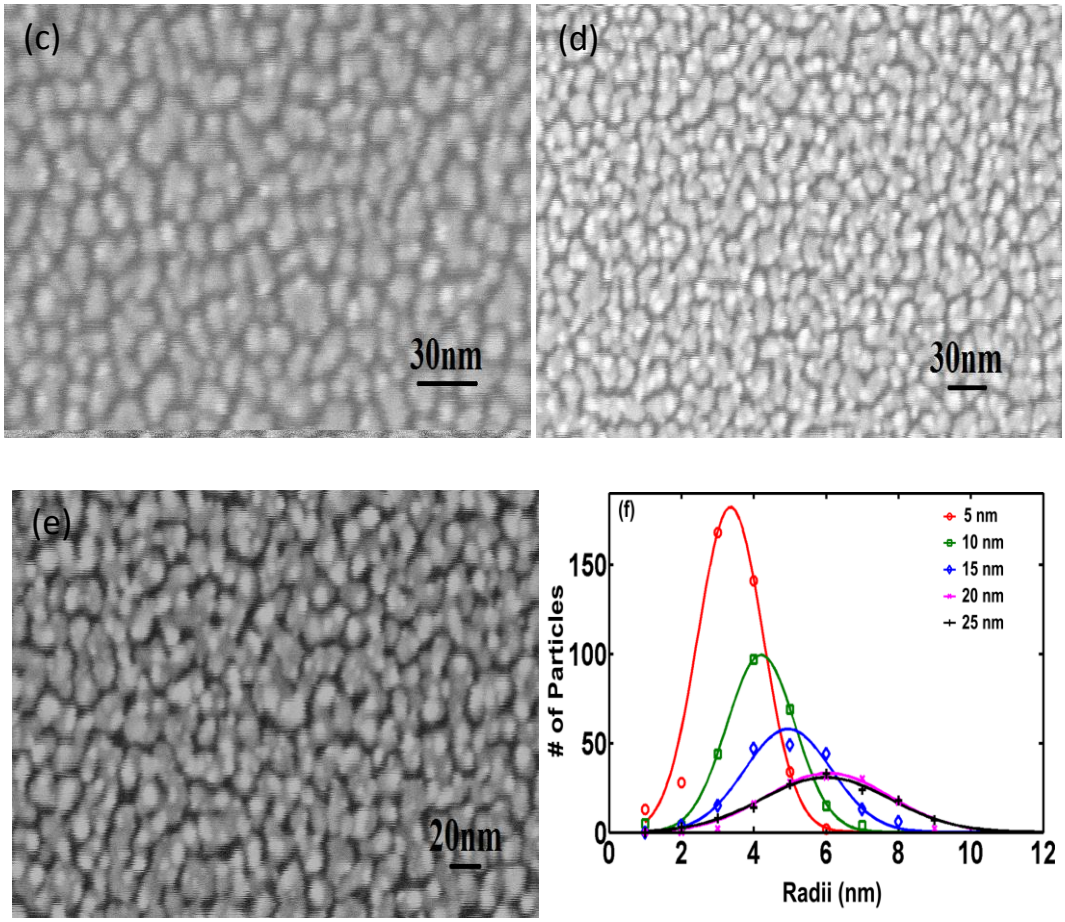

Figure 9. Gold nano-islands deposited at different times (a) 30s, (b) 60s, (c) 90s, (d) 120s, (e) 150s, (f) Size distribution of gold nano-islands [38].

As seen from the above high resolution micrographs, the spacing between the nano-islands decrease as the deposition is continued. The average pitch reduces from ~14 nm for the deposition carried out at the shortest time of 30 s, to ~ 6 nm for the deposition carried out at the longest time of 150 s. It is already known that if two metallic nanoparticles or nanostructures are brought very close to each other, then there exists a coupling of the fields exhibited by the nanostructures. This coupling gives rise to a high field region called as a hot spot. Thus, it can be easily understood that the nano-islands with smaller pitch would exhibit higher SERS activity than the ones with a bigger pitch. The formation of the nano-island structures can be explained by the known mechanism of

thin film growth process. The formation of a thin film is explained by nucleation and growth processes. When the condensable vapor that consists of atoms sputtered from the target material reaches the substrate, the atoms cannot be adsorbed unless they lose energy in the collision with the surface of the substrate. Thus, the atoms when in contact with the substrate can either condense onto the substrate or diffuse around the substrate depending on their binding energies as well as the substrate's temperature. These atoms are quite unstable and thus, they can either re-evaporate or they can bind with other atoms forming clusters, while diffusing across the substrate. The atoms while diffusing around the substrate combine with other singlet atoms leading to the formation of clusters. As the deposition is continued, atoms that arrive at the substrate join with the more stable already formed clusters thus leading to the formation of quasi-stable islands. This is called as the nucleation stage. Since these islands are stable, there will be a less chance for them to re-evaporate and a higher chance for them to get adsorbed onto the substrate. These adsorbed islands exhibit liquid like coalescence and as the deposition is continued further, these islands continue to grow in size and not in number, eventually to coalesce with each other forming a continuous thin film [37].

The structural evolution of the gold nano-islands as fabricated at different times was then correlated with their respective effects on SERS activity. In order to pursue their use for trace detection of bio-molecules and chemicals, their durability had to be tested for different solvents. Since the evaporated gold nano-islands could not even withstand solvents like water [35,36]; the first test was performed with water maintained at a temperature ~90°C. The water was made to flow vigorously on the sample. The samples were then observed under a scanning electron microscope to compare the effects of the

boiling water test. As seen from the high resolution micrographs for the before and after test, we can see that there is no apparent structural change in the morphology of the nano-island structures.

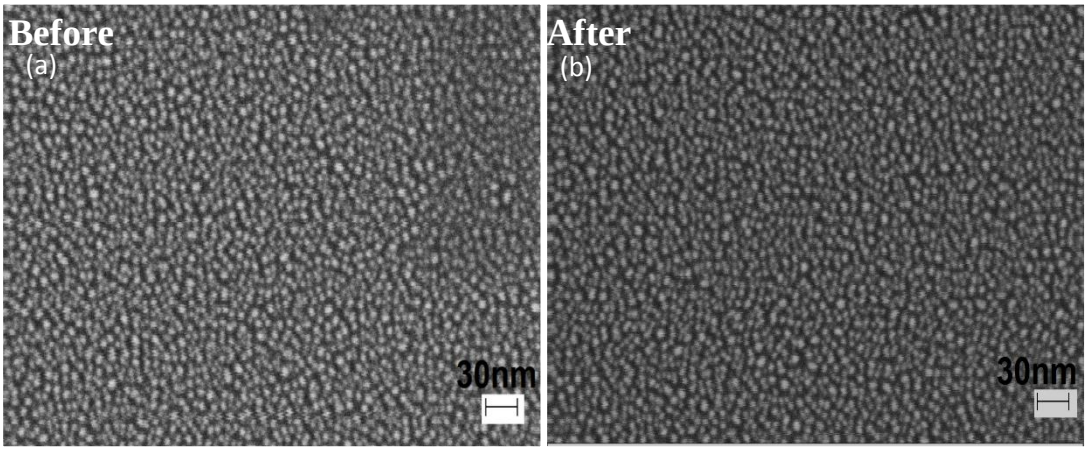

Figure 10. Durability tests of gold nano-island structures on Silicon and glass substrates, (a) before the hot boiling water test, (b) after vigorous rinsing of gold nano-islands in hot boiling water.

In accordance with the optical characterization of the nano-island substrates, an advantage of this technique is that no functionalization of the substrates is required which would otherwise cause optical interference. This is not the case for colloidal solutions of Au or Ag nano particles. Also, an additional advantage of these islands is, their compatibility with thiol groups makes it a lot easier to form self-assembled monolayer of thiophenol groups and also to quantify the number of molecules contributing for SERS when estimating the enhancement factor for the nano-island substrates [13].

Benzenethiol was used as the SERS marker molecule for gold nano-island substrates. The thiol group has a strong chemical affinity towards gold substrates, thus it tends to chemisorb on gold nano-island substrates. The process is called as a chemisorption process. The molecules tend to form a self-assembled monolayer. This is true since chemisorption ceases after all the active adsorption sites on the surface are

filled up by the molecules. The adsorption would still continue but only by the less tightly bound physisorption process. Once the substrates are rinsed vigorously in the solvent, the physisorbed molecules that are less tightly bound would be washed away and monolayer coverage of benzenethiol molecules would thus be obtained. The gold nano-island substrates were dipped in a 5 mM benzenethiol solution with ethanol as the solvent for about 30 minutes and then rinsed in the solvent for about 1 minute vigorously to form a self-assembled monolayer of benzenethiol molecules [40]. The coating of the SERS marker molecules also gave an indication of the durability of gold nano-island substrates.

The SERS measurements of benzenethiol molecules on gold nano-island substrates were carried out using a home built line-scan Raman microscopy system [13,42,62], enabling SERS mapping over 133×133 μm^2 regions with a 1 μm^2 resolution at a spectral resolution of 8 cm^{-1} [42]. A CW titanium:sapphire laser pumped by a diode pumped solid state laser was employed with an output wavelength of 785 nm. The experimental setup is as shown in Figure 11 [13,42,62]. The selection of excitation wavelength as 785 nm ensures that there would be no ambiguity presented by Resonance Raman scattering while using Benzenethiol molecules as SERS marker molecules, due to the absence of an absorption peak for Benzenethiol near that wavelength [40].

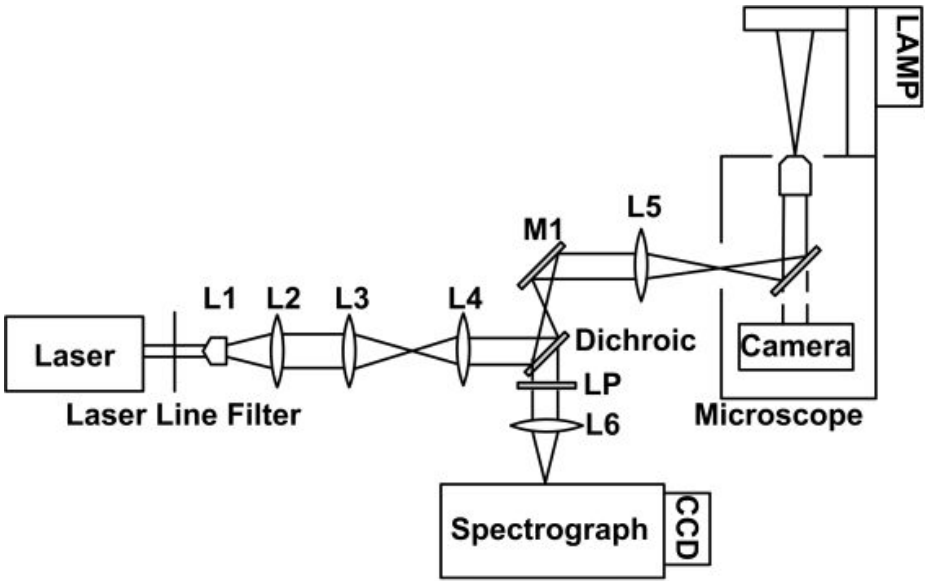

Figure 11. Home built experimental setup for measuring the Raman scattering enhancements.

3.3.2 Estimation of EF

It is often simpler to estimate the enhancement factor experimentally rather than predict the enhancement factor theoretically. Experimentally, the SERS enhancement factor is determined as [19]

$$EF = \frac{I_{SERS}}{I_{NRS}} \times \frac{N_{NRS}}{N_{SERS}}. \tag{13}$$

The EF estimation listed above describes the average Raman enhancement and thus it accounts for the enhancements of both the shifted as well as the incident excitation fields. Here I_{SERS} stands for the intensity or photons/s obtained due to the enhancement from the nano-structured substrate. I_{NRS} is the intensity of the normal Raman signal, N_{SERS} is the number of molecules that are contributing to the SERS activity, N_{NRS} is the number of molecules probed in the excitation volume or the laser spot. The number of molecules contributing to SERS or N_{SERS} is dependent on the roughness of the

nanostructured substrate. As explained earlier, benzenethiol molecules, due to their strong chemical affinity towards gold substrates tend to form a monolayer coverage. Since the density of the thiol molecules is known to be 6.8×10^{14} cm^{-2}, N_{SERS} or the number of contributing molecules can be estimated by calculating the product of the surface density of the molecules, the area of the laser spot and surface area of the nano-island structures. The area of the laser spot was calculated to be 1 μm^2 full-width at half-maximum (FWHM). The surface area factor takes count of the top surface as well as the side walls. The SERS intensity (I_{SERS}) and the normal Raman intensity (I_{NRS}) are estimated in separate experiments.

To estimate N_{NRS}, the excitation volume needs to be determined. Ji et.al., [40] determined this by sandwiching a monolayer of microspheres between two 25 mm × 25 mm glass cover slips, and dispensing a drop of 2 µL neat or 5mM benzenethiol solution into the gap by capillary force. Based on the spreading area of the solution, the average thickness of benzenethiol was estimated to be ~3 µm. Thus, the optical probing depth was ~3 µm and the excitation volume or the optical probing volume was estimated to be ~585.1. Thus, the number of molecules contributing for the normal Raman intensity of benzenethiol was estimated to be 3.4×10^{12}. Also, the normalized count rate for the benzene thiol normal Raman peak of 1583 cm^{-1} was estimated to be 97.7 photons $s^{-1}mW^{-1}$. By comparing the normal Raman peak for neat benzenethiol molecules and the SERS peak of benzenethiol molecules while on gold nano-island substrates, the enhancement factor came out to be around 0.1 million for the nano-islands deposited for 30 s.

Similarly, the enhancement factor was then estimated for nano-islands deposited at various times discussed earlier. The spectra shown in Figure 12 is an average spectra

for nano-islands deposited at various times. The different spectra were compared using two SERS bands – one at 1075 (denoted by a *) and the other at 1575 (denoted by a Δ) [38].

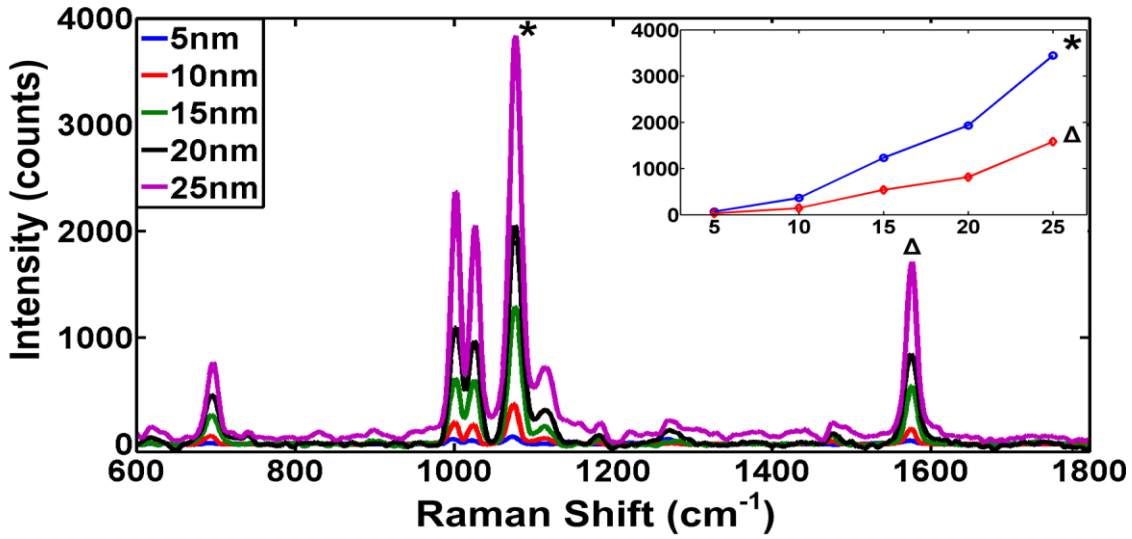

Figure 12. SERS spectra of benzenethiol molecules on gold nano-island substrates deposited at various times. The inset shows the variation of two specific peaks 1075 cm^{-1}(blue curve) and 1575 cm^{-1} (red curve) for the gold nano-island substrates [38].

As seen from the spectra shown above, the EF for the gold nano-islands deposited for 150 s was approximately 50 to 55 times higher (~5.2 million) for the two SERS bands 1075 and 1575 respectively than for the nano-islands deposited for 30 s. Thus, in correlation with high resolution micrographs, we were able to see an improvement in the SERS activity as the pitch of the gold nano-island structures decreased from ~14 nm, for substrates deposited for 30 s to ~6 nm, for substrates deposited for 150 s.

Chapter 4 – Structural Evolution of Nanoporous Gold (NPG) Thin Films on Gold-coated Substrates and its Impact on Surface Enhanced Raman Scattering

4.1 Introduction and Significance of Nanoporous Gold

The key attributes of SERS substrates for molecular sensing applications are a uniform, high-density distribution of intense hot-spots and large active surface area. There have been numerous reports of plasmonic nanostructured substrates recently [12,19,32,33,34], but most of these substrates require the need to search for a hot spot and they lack a higher SERS sensitive area along with lower density of hot spots. Thus, SERS substrates that can exhibit a reliable signal along with better hot spot coverage need to be developed to explore the wide range of SERS applications. In search for new in-expensive materials that can not only exhibit high density distribution of hot spots, but can also have tunable plasmonic properties; we came across Nanoporous gold [50,52,53]. Nanoporous gold (NPG), a bicontinuous 3D porous structure, has generated considerable interest since it promises higher SERS effective area and higher enhancement factors. Nanoporous gold is formed by Spinodal decomposition or a phase separation process [45] wherein the less noble constituent from a binary alloy film is selectively dissolved, which in our case is silver. The process of dealloying will be discussed later in the chapter, while discussing the evolution of nano porosity in NPG. The high enhancement obtained in NPG is attributed to the plasmonic coupling between neighboring ligaments of gold. Additionally, NPG is conductive, biocompatible, and structurally uniform, properties that make it attractive for fuel cell catalysts [46], MEMS devices [47], and low impedance neural probes [43]. Also, NPG was recently shown to exhibit both propagating and non-propagating plasmon resonances, making it an attractive choice for sensing applications.

Nanoporous gold, however, without any structural modification has not shown highly promising improvements in SERS enhancements. Therefore, in order to explore the various significant applications of Nanoporous plasmonics, several research groups [50,51] have shown that the enhancements obtained for NPG can be improved by optimizing the feature sizes or, by structuring them into discrete sub-wavelength patterns, while maintaining their internal 3D bi-continuous network depending on the desired application. We have studied the impact of both, the structural evolution of thin films of NPG and the effect of patterning NPG into discrete disk shaped particles on the SERS activity. This chapter studies the efficacy of NPG as a SERS substrate followed by the evolution of its porous network and in turn its effect on the SERS response. The structural evolution of the NPG network was studied as a first step towards optimizing the performance of structured SERS substrates. Our approach is to quench the dealloying process at various times evaluating SERS response and microstructure at each time. While the evolution of pore size and its effect on SERS response have been reported[53,54] as a function of post-etch thermal treatments; a fundamental study of the dealloying process itself has not been reported.

In this work, NPG films were fabricated by dealloying 75 nm thick, sputtered Au:Ag=28:72 atm% films in 70% concentrated nitric acid solution at room temperature. Micrographs were taken, self-assembled benzenethiol monolayers deposited, and SERS response measured for a series of dealloying times between 2 s and 1 hr.

4.2 Fabrication of NPG

4.2.1 Low Pressure Magnetron Sputter Deposition

Magnetron sputtering works on the principle of using an axial magnetic field near the cathode for secondary electron confinement, enabling sputter deposition at low pressures. The axial magnetic field in case of a planar circular magnetron configuration as seen from Figure 14 is provided by a button magnet in the center and a ring magnet near the edges. Since the target material is placed at the cathode, the use of the magnetic field causes electrons to be confined near the regions of the target material, thus increasing the path of the electrons through less recombination on the walls of the vacuum chamber. This can lead to an increased amount of ionization near the target material. Due to this higher ionization near the target by the confined electrons in case of magnetron sputtering, there is less concern of increasing the collisions by decreasing the mean free path, done by increasing the pressure. Thus, magnetron sputter deposition allows low pressure operation and higher quality of continuous and uniform films. When an electron is subjected to a magnetic field travelling away from the axis of the discharge, it moves in a helical motion. After each revolution of the helix, the electron would return back to the same radial position near the axis of the discharge. In the case of a magnetron assembly, the magnetic field is perpendicular to the applied electric field and parallel to the surface of the cathode, which makes the electrons move in cycloidal motions due to the Lorentz force [37]. If the magnetic field is oriented radially, an $E \times B$ drift is created and the confined electrons move in cycloidal motions along this $E \times B$ radial path. The circular magnetron is placed underneath a water cooled copper cathode surface and it is designed in such a way that the electrons close on themselves. This means that after one

revolution, the electron comes back to its original radial position. Thus, the magnetic field not only confines the electrons within the target region, but also increases the path length of the electrons, while decreasing their velocity towards the wall. Since the electrons keep on revolving around the radial path, the ionization or the ion current density is maximum in this region. This causes the target material to be sputtered mainly from this high density region. This causes a non-uniform utilization of the target material and thus an erosion groove is formed in this region coined as a 'racetrack'. The E × B radial path or the racetrack area of the target, can be seen in Figure 13. Most of the electrons are trapped by the magnetic field. However, some electrons that are travelling along the axis of the discharge will not be affected by the fields and tend to travel in straight trajectories towards the substrate. The electrons that have enough energy to cross the sheath travel in straight trajectories. These energetic electrons can then bombard the substrate and transfer their energy in the form of heat, causing some damage to the substrate. The heat damage due to these high energy electrons can be a serious issue if the substrate to be deposited, is heat sensitive. To get rid of this type of high energy particle bombardment, a magnetic anode can then be placed to trap these electrons and prevent them from damaging the substrate. By placing a magnetic anode on the walls of the chamber, we were able to deposit thin films on flexible substrates with very low melting points.

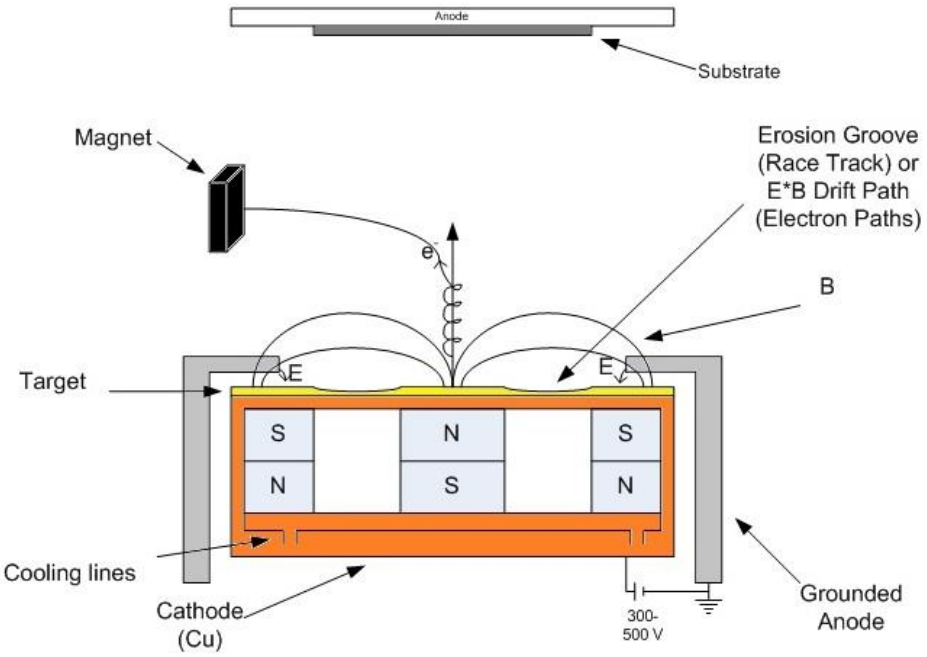

Figure 13. Configuration of the TORUS®axial 2 inch Sputter gun.

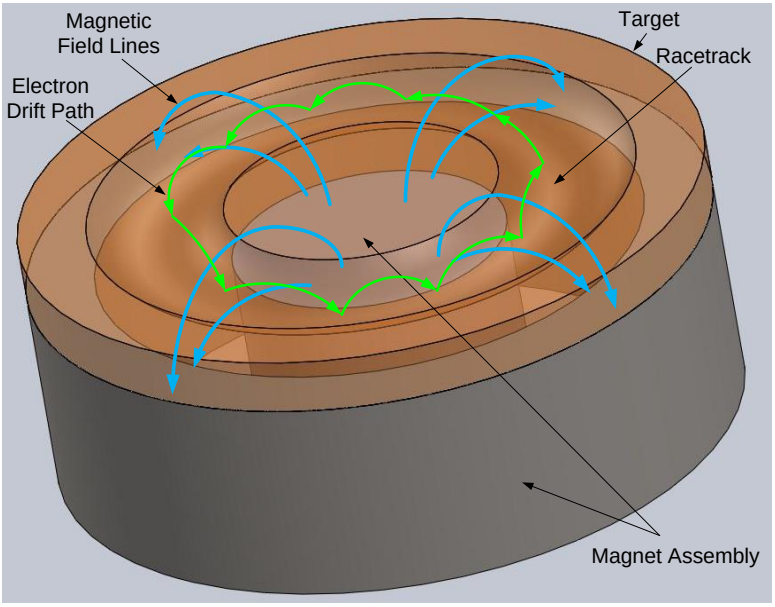

Figure 14. 3D diagram illustrating the drift path (E×B radial path) of electrons confined by the magnetron assembly underneath the target material.

The sputter deposition system that was built and designed for the deposition of noble metals is as shown in Figure 15 and its schematic is shown in Figure 16.

Figure 15. In-house DC magnetron sputter deposition system designed for metal depositions.

Although magnetron sputtering leads to non-uniform target utilization, the recycling of the target material still makes it a better and a less expensive option than other PVD methods. The sputter source for a magnetron sputter deposition system consists of a magnetron assembly, a thermally conductive copper cathode, a ground shield and a clamp to hold the target on top of the cathode as seen in Figure 16 and

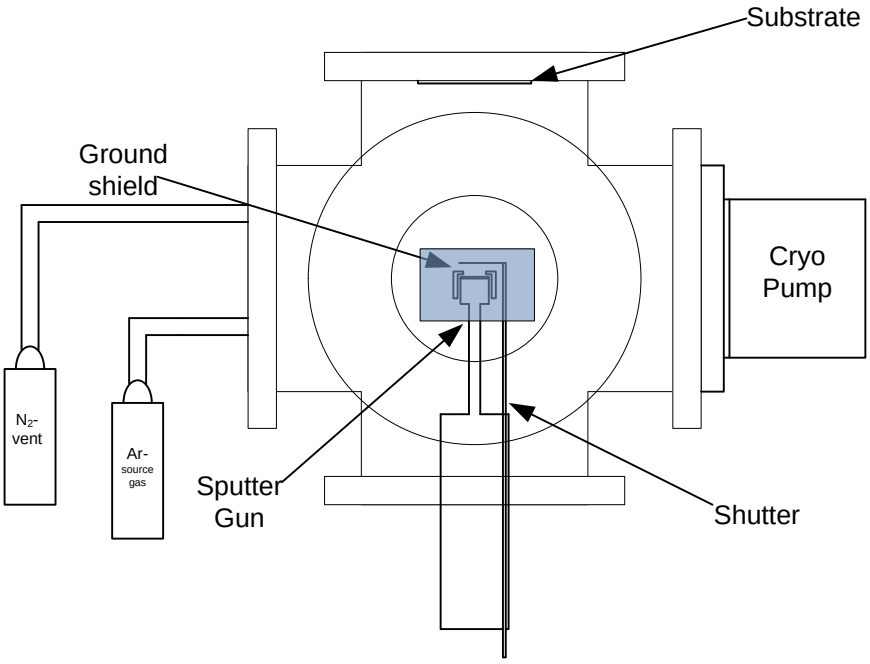

Figure 16 : Schematic showing the different significant accessories for the DC magnetron sputter deposition system developed.

Figure 13. The sputter source is also called as a sputter gun or S-gun. The magnetron assembly is placed underneath a copper cathode assembly. The cathode assembly is cooled throughout the deposition. The configuration of the magnetron assembly looks like as shown in the Figure 14. The figure shows the configuration of the sputter source as well as the configuration of the magnetron assembly. There are certain practical considerations while making a sputtering system. Along with the magnetron assembly, some more features or modifications need to be made for optimum operation as can be seen from Figure 16. The target is surrounded by a shield called as the ground shield. The ground shield has a very important purpose in a sputtering system which is to confine the ion bombardment to the target material and preventing any energetic ion bombardment on the clamps, bolts or anything that can contaminate the film. Thus, the ground shield allows deposition of thin films with high purity by preventing energetic ion sputtering of

any material other than the target material. The same purpose is also achieved by keeping the space between the ground shield and the target material or the cathode lesser than the thickness of the dark space. However, since the thickness of the dark space is dependent on the working pressure, there exist some pressure constraints for the operation of the system. One more feature that can be seen from Figure 16 is the "shutter". The shutter is used to interpolate during the initial period of sputter deposition. This period is called as pre-sputtering period or the cleaning period of the target material. Since the system is exposed to atmosphere while loading and un-loading the substrates and, while replacing the target material, it is quite possible that the target material can get contaminated. Thus, during the pre-sputtering period, in order to not transfer the first few layers of contamination from the target to the substrate, the shutter is used as an interposition between the target and the substrate, thus causing the shutter to be coated with the contaminated layer and not the substrate. This step, as explained above, is thus used as a dry cleaning step where the target material is cleaned while in vacuum conditions just before the deposition, thus preventing any contamination to be deposited on the substrate. Hence, with the help of the shutter and a ground shield, very high purity films can be achieved using magnetron sputtering.

The fabrication process flow is as shown in Figure 16. The cleaned silicon substrates are coated with a soft layer of gold using a home built DC magnetron sputter deposition system. The gold layer is deposited as a supporting layer for the formation of nanoporous gold substrates. The vacuum chamber was pumped down to a base pressure of 8×10^{-7} Torr before the gold deposition and the gold target used was a 99.999% Canadian gold maple leaf.

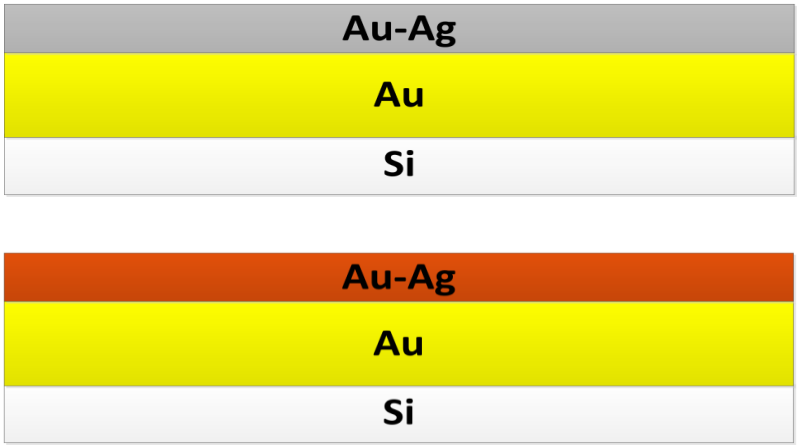

Figure 17. Fabrication process flow for the fabrication of substrate constrained NPG.

4.2.2 Free Corrosion Process for the Formation of NPG

Nanoporous gold is formed by a dynamic pattern formation process [45] wherein the less noble constituent from the alloy material is freely corroded to form a bi-continuous porous structure. The nanoporous network thus formed, is interconnected and random throughout its volume composed almost entirely of the nobler constituent. This process is called as a selective dissolution or a dealloying process. There are two common fabrication methods for dealloying a precursor binary alloy system namely electrochemical dealloying and a free corrosion process. Free corrosion is a simple process, wherein the alloy system is simply submerged in an aqueous acidic solution. We have employed the method of free corrosion process under room temperature conditions, wherein we selectively leech out the less noble constituent using a concentrated acid solution. Several research groups have supported the idea that the porous structure obtained is controlled by a competition between the dissolution of the less noble constituent that causes roughening and the diffusion of nobler atoms that causes smoothening during the dealloying process. Erlebacher in 2001 [45], have reviewed the kinetics of dissolution during the dealloying process using Monte Carlo simulations. The

simulations reveal that there is an analogy between the kinetics of the dissolution process and thin film growth in a vapor phase deposition process. As soon as the silver from the first or the surface layer of the alloy film is dissolved, the gold adatoms formed start to diffuse about and agglomerate to form clusters or islands. Due to this diffusion-controlled coarsening process, continuous active pathways are still existent for the acid to penetrate and etch the less noble material that does not get passivated from the remaining gold. Hence, more gold adatoms are formed due to the dissolution of the exposed alloy film. These newly formed gold adatoms do not form new islands but instead diffuse to the islands that were previously formed, thus increasing the size of the islands and not the number. This ensures that the un-dealloyed material is still exposed to the acid. In the early stages of the dealloying process, the gold islands or clusters that are formed are similar to mounds that are rich in gold at their peaks but still have silver at their bases. Since the silver is still exposed to the acid, these mounds get undercut thus increasing the surface area and ultimately leading to a 3D porosity formation in Nanoporous gold. The general requirement for selective dissolution to occur is related to the initial composition of the nobler constituent. For Au-Ag alloy system, if the initial composition of the nobler constituent (Au) is high, then the etching of the first few layers of Ag from the binary system would cause an enrichment of Au, thus slowing or stopping the dissolution process. Experimental findings from Newman [56] suggested that the parting limit for gold should not exceed 40 atm% and thus for silver, the limit should not exceed 60 atm% for homogenous Au-Ag binary alloy systems.

Nanoporous gold can be either fabricated as free standing leaves or blanket thin films using vapor phase deposition processes. Dealloying alloy leaves can give rise to

crack-free Nanoporous gold films. The leaves during the free corrosion process tend to spread out uniformly due to surface tension. However, since the dealloyed alloy leaves float on the acid solution, they are difficult to handle and can be very fragile. In order to utilize these leaves for various applications, they have to be then transferred to substrates which involves manual handling. Supported/constraint nanoporous gold films tend to exhibit high density of crack defects that can increase or decrease depending on the stress induced by the supporting film. As discussed earlier, dealloying process consists of two competing mechanisms, dissolution of silver from a precursor binary alloy film constrained to a substrate and, surface diffusion of gold adatoms. The dissolution of silver is basically responsible for building up stress in the material during the dealloying process, while the surface diffusion of gold is responsible for relaxing of the stress. Sputtered thin films exhibit higher density of grains with sizes in nanometer scale. Thus, the density of grain boundaries is also high. Also, if the supporting film has a high tensile stress, gold tends to diffuse towards the grain boundaries and relieve the stress that is built up. We were able to optimize the conditions for the deposition of the supporting film in order to minimize the crack defects. This was achieved by decreasing the flux of the particles bombarding on the substrate during the deposition. Effectively, there are two ways to decrease the flux of the bombarding species. One way is to increase the distance between the source and the target, thereby reducing atomic peening during thin film deposition and the other way is to increase the pressure. Both, the increasing target-to-substrate distance and increasing the pressure reduce the flux of the bombarding species by inducing scattering. The optimum pressure was chosen to be 7 mTorr and the source

to substrate distance as 6 inch or 150mm. The power was kept constant at 50 W in order to not reduce the deposition rates by a big factor.

The gold-silver alloy film was then subsequently deposited using the same DC magnetron sputter deposition system with a TORUS® axial 1 inch sputter source. The alloy deposition was carried out using a custom precursor alloy target (Au:Ag= 28:72 atm%). The target was provided by ACI alloys Inc. The gold-silver alloy was deposited at an optimized working pressure of 5 mTorr and the power of 50 W. The composition of the alloy film was sustained during the alloy sputter deposition, as shown by Energy-dispersive X-ray spectroscopy measurements.

The homogenous precursor gold-silver alloy (Au:Ag=28:72 atm%) substrates were then dipped in a 70% concentrated nitric acid solution to selectively leech out the less noble constituent from the alloy or silver in this case, to form nanoporous gold. The dealloying process was carried out under room temperature conditions. The NPG film does not de-laminate in the rinsing step due to the supporting gold layer underneath.

The dealloyed substrates were subjected to rinsing in de-ionized water with vigorous agitation multiple times in order to quench the process completely without causing any further etching. Each substrate was rinsed in de-ionized water for an optimized interval of two minutes in two separate containers vigorously. This vigorous quenching process is significant in obtaining smaller feature sizes and thus, we were able to achieve pore sizes as small as 3 nm under room temperature conditions (smaller than that reported in literature [52-54]) with high reproducibility. The smallest pore size reported in the literature for room temperature conditions is around 15 nm [52-54]. The

nanoporous network thus formed did not change over a period of few months due to an optimized quenching process.

4.3 Significance of NPG for Applications in Molecular Sensing

The key attributes of nanoporous gold, in context of molecular sensing applications, are high density of hot spots, high surface to volume ratio, large SERS effective area, high chemical stability & renewability and tunable plasmonic properties. Through alteration of simple processing parameters, Nanoporous gold can alleviate molecular sieving effect and thus be used for trace detection of molecules with multiple sizes.

4.4 Results and Discussion

4.4.1 Surface Morphology

The surface and cross-sectional morphology of NPG films were studied using a LEO 1525 scanning electron microscope with a resolution limit of 3 nm at an electron energy of 15 keV. As discussed earlier, the cleaned Silicon substrates were coated with an optimized soft gold layer in order to reduce the density of cracks, prominent in the case of supported NPG films. This becomes quite apparent from the high resolution SEM images. The alloy substrates dipped for few seconds in a 70% aqueous nitric acid solution manifested porosity throughout their entire thickness. This can be seen quite clearly from the scanning electron micrographs.

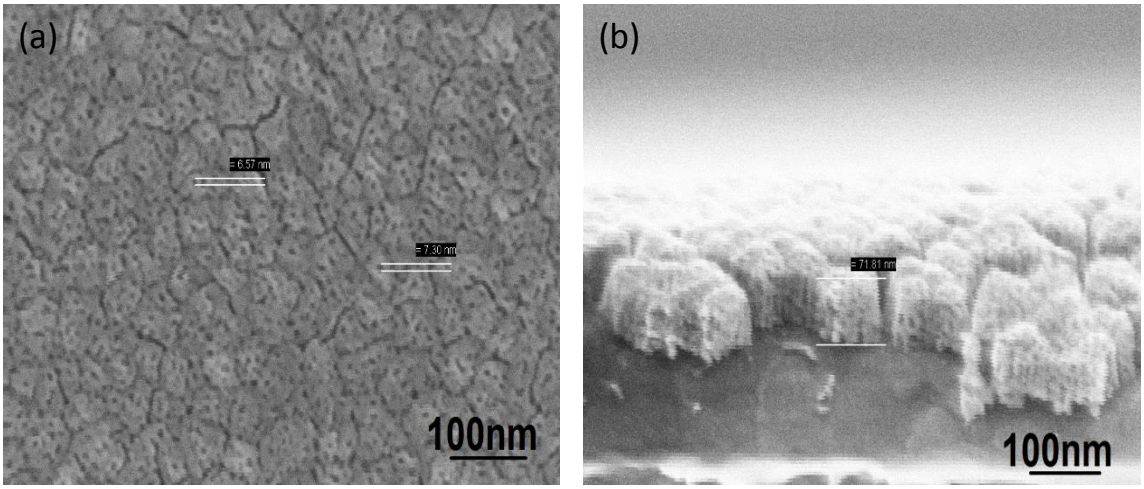

Figure 18. Scanning electron micrographs for NPG films dealloyed for few seconds.

4.4.2 Efficacy of NPG as a SERS Substrate

As it was discussed earlier, since surface enhanced Raman spectroscopy is a distance dependent technique, the Raman signal decays as the distance between the Raman marker molecule and the metallic nano-structured substrate is increased. Thin films of NPG were then coated with chemisorbing thiol molecules that can form monolayer coverage. Since the hydrocarbon chain length for Benzenethiol molecules is short, the distance between the SERS marker molecules and the nano-structured substrate could be kept short. The hydrocarbon chain can be varied depending on the application. Similar to the strong affinity of bulk gold substrates with thiol molecules, nanoporous gold has an additional advantage of being compatible and having strong chemical affinity with the thiol Raman linking molecules. Hence, the nanoporous gold substrates were then dipped in a 5mM benzenethiol (BT) solution with ethanol as the solvent for 30 minutes for the formation of a self-assembled monolayer of Raman active BT molecules, followed by a subsequent rinsing in ethanol for 1 minute [40]. The BT coated substrates

were then tested with an excitation wavelength of 785 nm using a home built line scan Raman microscopy system [42] that allows mapping over 133*133 μm^2 with a resolution of ~1 μm^2 at a spectral resolution of 8 cm^{-1}.

4.4.3 Determination of EF

SERS Enhancement Factor (EF) is a value that characterizes the effectiveness of the SERS substrate by estimating the increase in the intensity obtained for the SERS marker molecules (SERS intensity) when subjected to the fabricated nano-structure as compared to the intensity obtained for neat molecules or the normal Raman intensity. The selection of thiol molecules allows the number of molecules to be quantified quite easily which is one of the important parameters in determining the SERS EF. The most widely used practical definition for the SERS EF is described as

$$EF = \frac{I_{SERS}}{I_{NRS}} \times \frac{N_{NRS}}{N_{SERS}}, \tag{14}$$

where I_{SERS} is the normalized surface enhanced Raman intensity and I_{NRS} is the normalized Raman intensity from the neat BT solution, N_{NRS} is the number of molecules in the scattering or the excitation volume for the neat BT solution and N_{SERS} is the number of molecules contributing to SERS intensity. This analytical estimation gives the average enhancement rather than the maximum enhancement at a particular excitation wavelength.

N_{SERS} is calculated as the product of the roughness factor of the NPG film and the surface density of BT molecules. The BT surface density was assumed to be 6.8 × 10^{14} molecules/cm^2. The roughness factor is defined as the ratio of the chemically active area to the geometrical surface area. To estimate the roughness factor, it was assumed

that the nano-structure is uniform throughout the thickness of the film. The porosity was analyzed using an image analyzing software ImageJ. The high resolution SEM images were then analyzed using ImageJ and the porosity was estimated to be 34%. The roughness factor according to reference [43] is given as

$$R = 3h\beta/r \,, \tag{15}$$

where β is the porosity, h is the thickness of the film and r is the mean pore width. From image analysis, the mean pore width was estimated to be ~7 nm. Thus, the roughness of the film was estimated to be 22 when the thickness of the film is 75 nm. The amplitude of the laser while propagating through a conductor decays exponentially on a length scale which is termed as the skin depth. Due to the skin effect, N_{SERS} also decreases with depth. The effective roughness of the NPG was estimated to be 6.3. This means that the SERS effective area for NPG is about 6.3 times higher than its geometrical surface area. Now, in order to estimate the SERS intensity, three areas of the substrates were scanned by the laser spot width of 1 μm. The number of steps in each area scan was chosen as 100 and thus the area of each scan was 100 × 133 μm^2. The resultant SERS intensity was then normalized to the laser power and the area of the laser spot.

To estimate the normal Raman intensity as well as the molecules in the excitation volume, the procedure as explained earlier, wherein the solution was dispersed inside a channel fabricated using polystyrene microspheres, was carried out. The excitation volume was estimated to be 585.1 μm^3. The number of molecules in the excitation volume was estimated to be 3.4 × 10^{12} molecules. The normal Raman intensity was measured to be 97.7 photons/s/mW for the normal Raman peak of 1584 cm^{-1}. Thus, the average enhancement factor as given from equation 12 was estimated to be 0.62 million.

4.5 Evolution of NPG Microstructure during the Dealloying Process and its Effect on the SERS Response for a Monolayer of Benzenethiol Molecules

Nanoporous gold can exhibit a wide range of tunability through alteration of simple processing parameters that include initial composition of the alloy material, the concentration of acid (in a free corrosion process), time of dealloying and, temperature while or after the dealloying process [43,45,50-54]. The SERS response as measured in the previous section for NPG dealloyed for few seconds was not highly promising; only comparable to the commercially available SERS substrates. However, in order to explore the various significant applications of NPG, several research groups have shown that the SERS sensitivity can be improved through some minor modifications either in the NPG microstructure or by patterning the nanoporous network into discrete standard shapes [50-54]. Here, we report the structural evolution of NPG network and the effect of the evolution on SERS enhancements. This study on the evolution of the porous structure of NPG was then applied to the patterned NPG structures. We were able to experimentally prove the analogy between the diffusion in a thin film vapor phase deposition process and the diffusion of mobile gold adatoms in the dealloying process even after almost all the silver is etched away. We saw that even after the silver is almost completely etched away for thin sputtered films of alloy, the pore morphology is still changing without any external excitation mainly due to the diffusion of the mobile gold adatoms. L.H.Qian [53] reported that the enhancements for NPG can be increased when the pore widths are reduced in size and that the enhancements start to decrease as the pore widths are increased. In contrary to the report by L.H. Qian [53], a research group from Lawrence Livermore (S.O. Kucheyev [54]) observed highest enhancements in the SERS signal for a

pore size of ~250 nm. However, these experiments involved the increase of the pore sizes by using thermal treatment post dealloying. Also, the experiments were conducted on freestanding films that were about 60 μm thick [53] and 300 μm [54] at various temperatures. Contradictorily, we have been able to recover high enhancements even when the enhancements are not being dominated due to the silver content [53] or the roughness in the ligament structures [54]. Instead of post-etch thermal treatments or pre-etch variation in the alloy composition, only the dealloying time was varied to study the correlation between the porous structure and the SERS response. While correlating the porous structure with the SERS response, we were able to obtain feature sizes (~3 nm) smaller than reported in the literature (~15 nm) [52] under room temperature etching conditions. Smaller feature sizes have been shown to be significant for higher detection sensitivities [53], thus the dealloying process was followed by a vigorous quenching process in order to achieve good reproducibility. Thus, sputtered Au:Ag=28:72 atm%, 75nm thin films of alloy supported on a soft thick (~350 nm) gold layer, were dealloyed under room temperature conditions for various times. We observed two distinct regimes in the SERS response for NPG film when it was dealloyed under room temperature conditions for various dealloying times. The surface morphology for the thin films of nanoporous gold was studied using high resolution scanning electron micrographs with a LEO 1525 scanning electron microscope and the effect of these changes on field enhancements were studied using a line-scan Raman microscopy system. The NPG film exhibits a nanoporous network with very small pore sizes for short dealloying times. During the early stages of etching, the dealloying process starts with the attacking of the grain boundaries prominently. The crack defects that are formed due to the effects of

shrinkage and weak grain boundaries penetrate throughout the thickness of the film slicing the film into isolated crystallites with high aspect ratio intercrystallite gaps. The pore size of ~3 nm obtained for short dealloying times, revealed high silver content when measured using Energy dispersive X-ray spectroscopy. The high silver content in these films seems to be responsible for giving out high enhancements as observed in the literature [53]. However, as the dealloying is continued further, the pores start to get bigger and the silver gets almost entirely etched away within about 6 seconds of etching (10 atm% from EDS experiments). Thus, with the increase in the dealloying time, the sizes of the high aspect ratio intercrystallite gaps start to increase. This increase in the size of the gaps, pores, along with the reduced silver content cause the decaying of the SERS enhancements with the increase in the dealloying times.

The effects of shrinkage as well as weak grain boundary etching leading to sliced gold crystallites can be seen quite clearly from the electron micrographs that show the before and after dealloying process images (Figure 19(a) and 19(b) respectively). The high resolution micrograph as seen in Figure 20 demonstrates the initiation for the formation of inter-crystallite gaps and shrinkage effects. Under room temperature conditions, in order to obtain pore sizes smaller than ~10 nm for NPG, the dealloying process was quenched well enough to stop any further dissolution. After the acid dealloying step, the samples were rinsed in DI water multiple times in two different containers with vigorous agitation. The rinsing step was optimized to be 2 minutes in each container of DI water. This is significant for obtaining small feature sizes as it will prevent any further etching, causing no changes in the pore morphology of the nanoporous gold film over a period of few months.

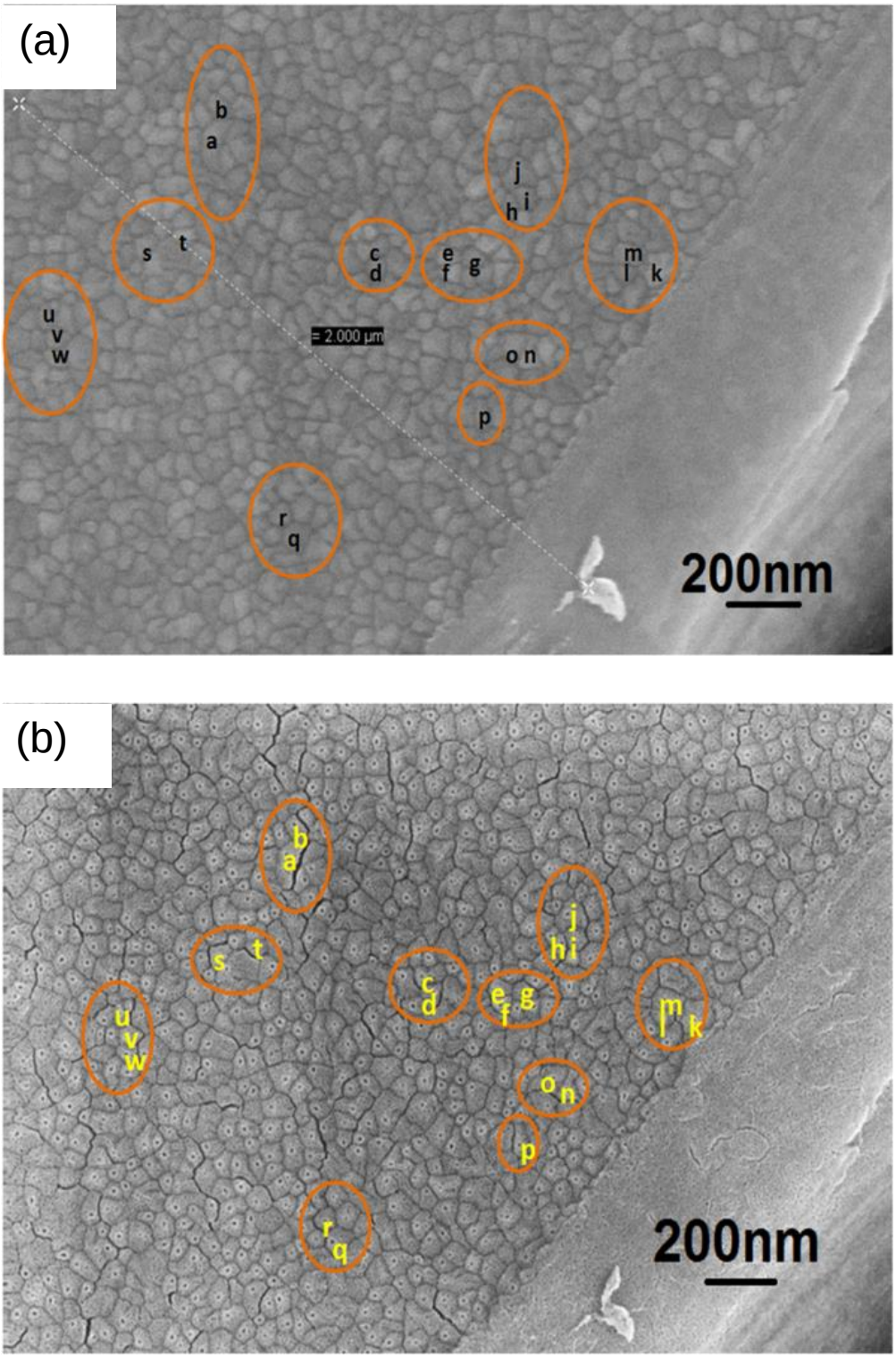

Figure 19. Scanning electron micrographs for (a) As deposited 75 nm sputtered $Au_{28}Ag_{72}$ alloy film on a soft gold film, (b) Identical area after the dealloying process.

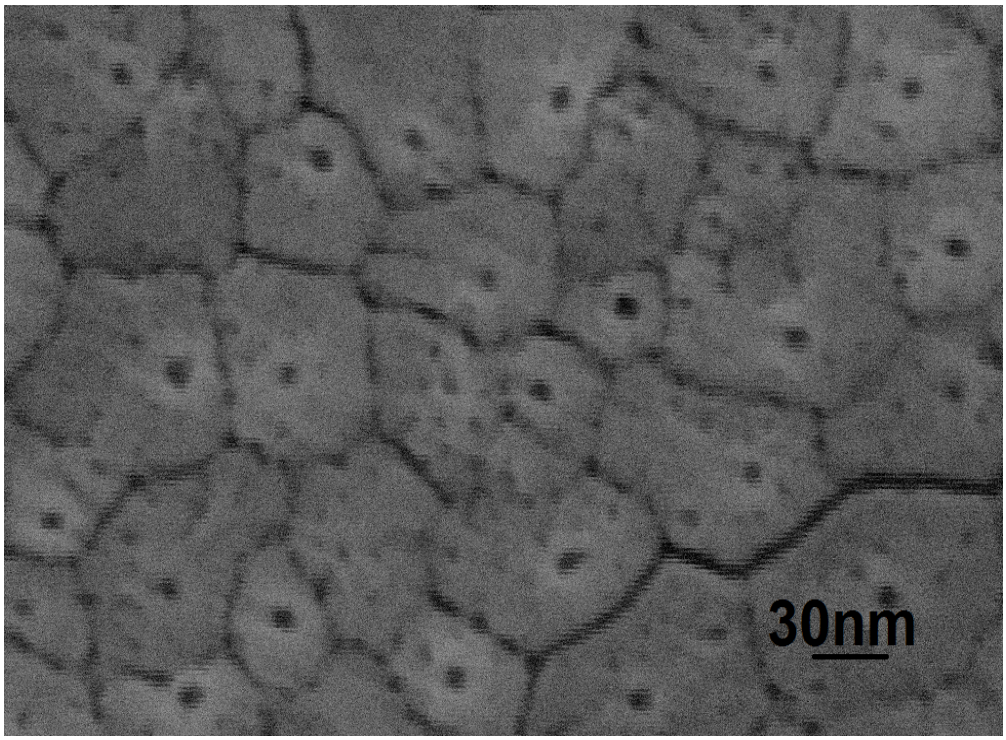

Figure 20. High resolution micrograph showing the effects of shrinkage and weak grain boundary etching.

As we had already seen that NPG has a strong chemical affinity towards thiol group molecules, a self-assembled monolayer of benzenethiol was then subsequently deposited for each pore size by dipping into a 5mM solution of benzenethiol with ethanol as the solvent for 30 minutes followed by rinsing in the solvent for 1 minute. The substrates were then tested for SERS activity using the same home-built line scan Raman spectroscopy system with an excitation wavelength of 785 nm, discussed in an earlier chapter. The SEM images for different dealloying times of NPG film is as shown below in Figure 21 (a) - (i).

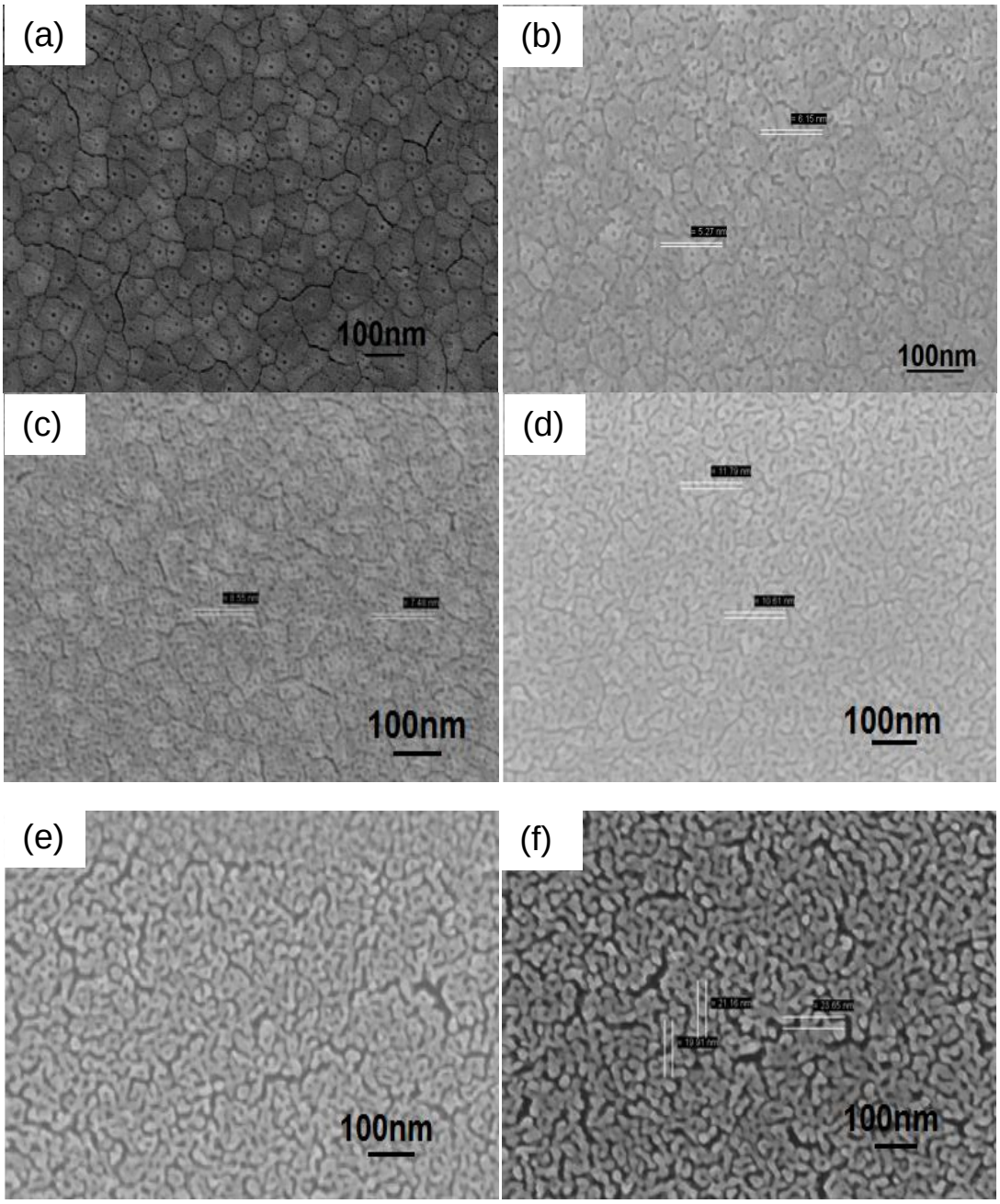
(a)
100nm
(b)
100nm
(c)
100nm
(d)
100nm
(e)
100nm
(f)
100nm

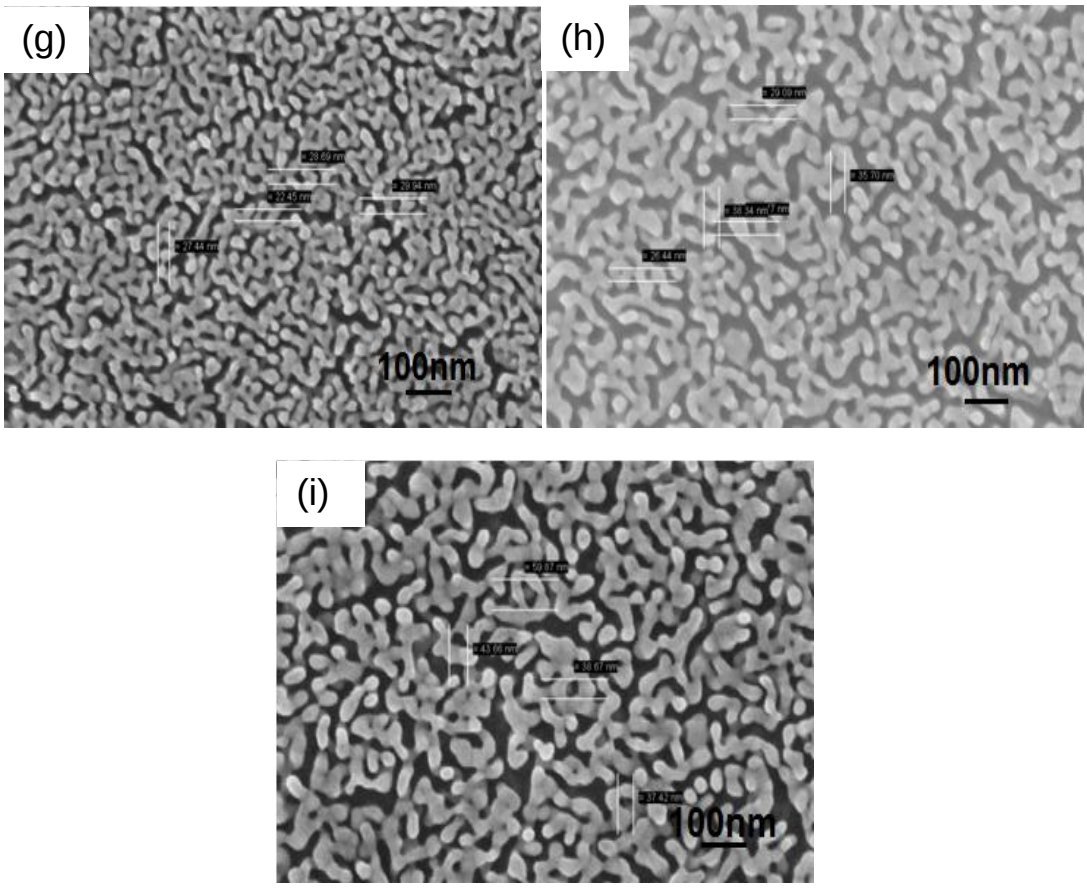

Figure 21. High resolution SEM micrographs for NPG films dealloyed at various specific times from 2s 1hr.

NPG has been shown to exhibit volume shrinkage when one component from an alloy system is selectively removed. NPG films dealloyed at various times from 2s-1hr were then looked at from the side (Figure 22 (a) – (d)), in order to understand the effects of shrinkage, initiation of inter-crystallite gaps during early stages of dealloying and closing of inter-crystallite gaps when the silver is almost completely etched away.

As seen in the scanning electron microscope images in Figure 22, during the early stages of dealloying process, nitric acid attacks the grain boundaries of the alloy film creating vertical crystallites. First a nanoporous network is developed in these crystallites.

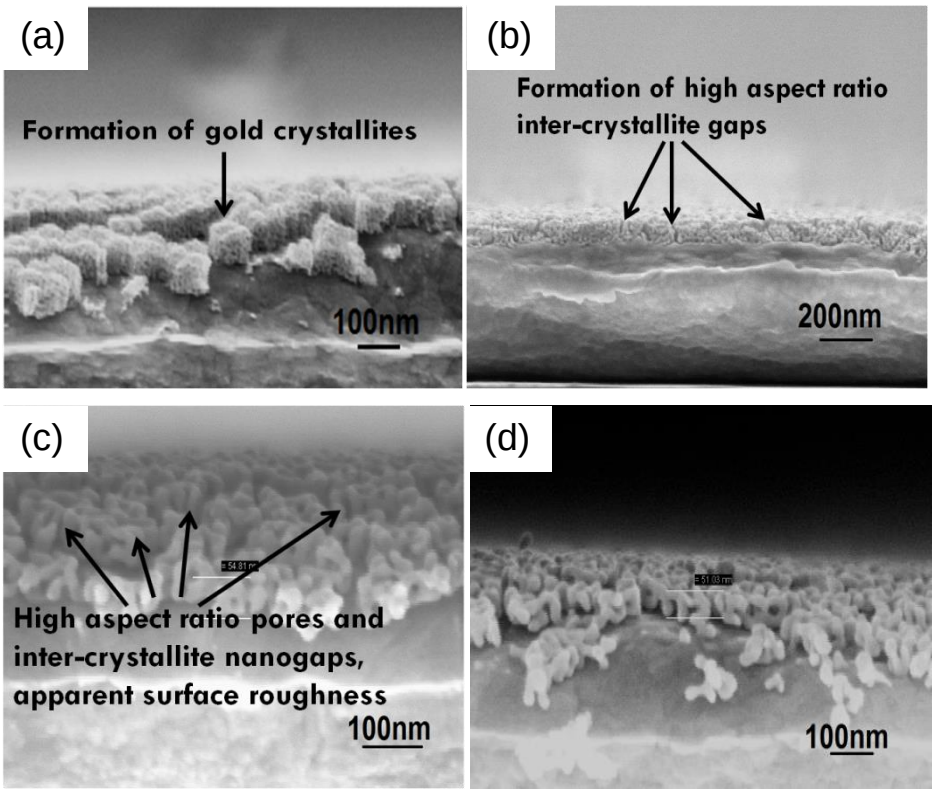

Figure 22 : Cross-sectional views for nanoporous gold showing the formation of gold rich crystallites and high aspect ratio gaps during early stages of etching ((a) & (b)), surface roughness due to continued diffusion of gold atoms in later stages of etching ((c) & (d)).

However, as the dealloying is continued, these crystallites start to shrink and the pore sizes start to increase as silver is simultaneously being etched away. After about one minute of dealloying, the silver is almost completely etched away and due to the continued surface diffusion of gold adatoms, the pores start to close up, while simultaneously shrinking the NPG film. This causes the intercrystallite gaps to become narrower and the crystallites tend to become rounded. This is seen from the cross-section SEM images as seen in Figure 22. The increased surface roughness as well as the formation of high aspect ratio intercrystallite gaps enhance the SERS response for NPG dealloyed for a longer duration. Thus, due to the change in the NPG microstructure, the enhancements are recovered even when the pore sizes are increased. This change in the

NPG structure can be very well explained by the kinetics of dissolution process as reported by Erlecbacher [45]. As reported by the studies, dealloying process is considered to be analogous to a thin film deposition process wherein surface diffusion of gold adatoms formed during the etching of alloy material causes the creation of a random interconnected porous network. In the case of gold nano-islands, when more sputtered gold adatoms arrive at the substrate as the deposition is continued, the islands in order to reach a stable state tend to come closer to each other as their size is continuously increasing. At this time, the islands are getting thicker and due to this their diffusivity is not so high that they can diffuse and coalesce. If the deposition is stopped at this point, the thick islands would be left isolated from each other. These thicker isolated islands give out high enhancements due to the existence of high electric fields in between the islands. This was demonstrated in the previous chapter. Thus, in case of NPG films etched for a longer duration, as more and more gold adatoms diffuse to the nearby gold clusters or the crystallites, the intercrystallite gaps start to narrow down which results into a high SERS response as will be seen during the enhancement factor calculations.

As we have seen earlier, in order to estimate the enhancement factor, the roughness factor which is the ratio of the chemically active area to the geometrical surface area, needs to be calculated. For NPG films, due to random pore morphology, this was done using an image analysis open-source software ImageJ. The pore sizes obtained varied from 3-28 nm for the dealloying times ranging from 2 seconds – 1 hour (Table 1 and Figure 23).

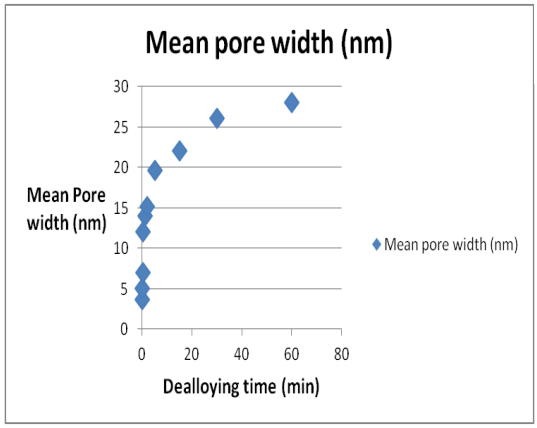

Figure 23 : Mean pore width with various dealloying times.

Table 1. Mean pore width for various specific dealloying times.

Mean pore width (nm)	Dealloying time(min)
3.6	0.033333333
5	0.066666667
7	0.1
12	0.2
14	1
15.08	2
19.6	5
22	15
26	30
28	60

The porosity as well as mean pore sizes as mentioned in the table above was estimated using image analysis from the high resolution SEM images. As it was already discussed, the average EF can be estimated as seen in equation [12] from Chapter 2.

The number of molecules that contribute to the normal Raman intensity as well as the molecules that exhibit SERS intensity for benzenethiol molecules was estimated as described earlier. However, since the number of molecules contributing to SERS activity is dependent on the roughness of the porous structure, this had to be estimated for NPG film dealloyed for each specific time. The enhancement factor (EF) was thus estimated and tabulated for each dealloying time in Table 2.

However, as seen from equation [12] from Chapter 2, enhancement factor is dependent on the number of molecules contributing for the SERS activity (N_{SERS}). N_{SERS} is in turn dependent on the roughness factor of the NPG film. The estimation of the roughness factor involves a high degree of tolerance. Thus, the evolution of the porous structure was

Table 2. Enhancement Factor trend for different specific dealloying times.

Dealloying time(min)	EF (×10^6)
0.033333333	**1.31**
0.066666667	**0.75**
0.1	**0.621**
0.2	**0.49**
1	**1.186**
2	**1.547**
5	**1.8**
15	**2.43**
30	**3.062**
60	**3.3**

correlated with SERS intensity or count rate instead of the enhancement factor for each specific dealloying time. Thus the SERS intensity, normalized with respect to the power and the area of the laser spot, was then plotted with respect to the dealloying time for thin films of NPG as shown in Figure 24. The process of evolving the porous structure of NPG, using the processing parameter of dealloying time, was reproduced for more sets of samples. The response observed across various sets of NPG substrates followed the same trend of high enhancements for the shorter dealloying times, a decaying trend of SERS activity, and an increasing trend of SERS intensity as the gold rich crystallites close in the intercrystallite gaps. The SERS response calculated for two sets of NPG substrates exhibited a maximum error of ~5% as shown in the chart below.

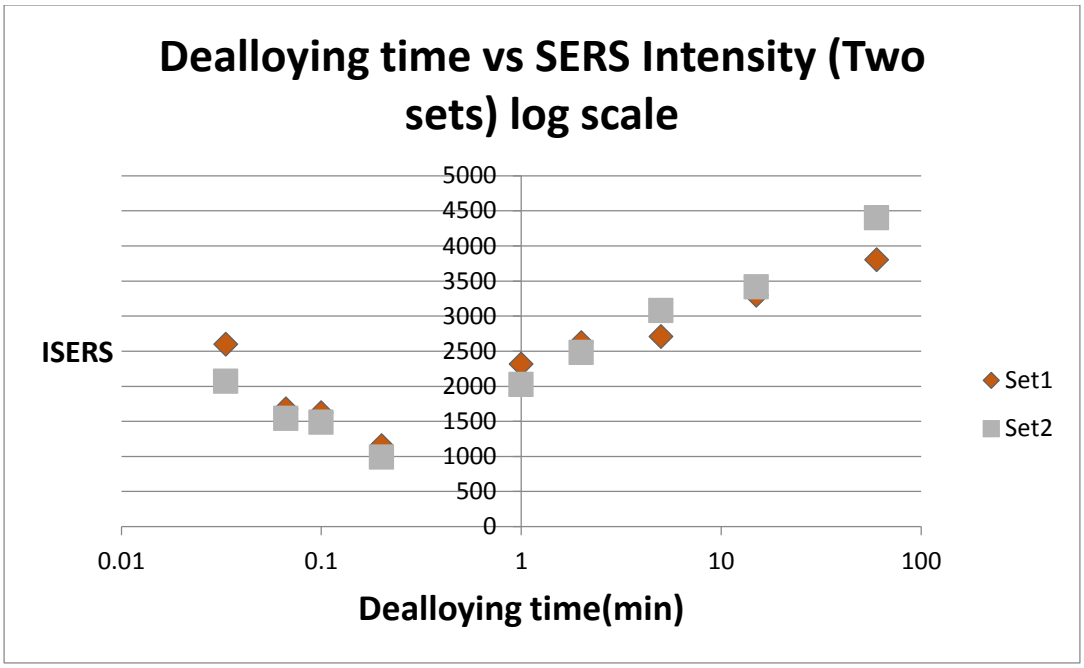

Figure 24. Plot of SERS intensity (A.U.) or count rate with the dealloying time

As explained earlier, the continued etching of NPG films causes high aspect ratio intercrystallite gaps, thus creating higher SERS activity than expected. Hence, as can be seen from the graph of the dealloying time with respect to the SERS intensity, there are two regimes controlling the SERS response in thin films of NPG. The first regime where the SERS response decays, seems to be controlled by the increase in the pore sizes as well as the reduction in silver content while the dealloying time is kept on increasing. After ~1min of dealloying, the SERS response starts to recover as explained earlier by the kinetics of the dissolution process wherein the high aspect ratio intercrystallite gaps as well as the higher surface roughness seem to be contributing to the higher SERS activity. Thus, we were able to achieve ~50 fold higher enhancements than those that were achieved for NPG films dealloyed for few seconds.

For a better understanding of this structural evolution of NPG, the elemental composition of NPG films dealloyed for different times was estimated using Energy Dispersive Spectrometry (JEOL). The composition of silver for various specific dealloying times is as plotted below in Figure 25. The red oval represents the early stages of etching, when the SERS enhancements seem to be dominated by the increase in the pore size, widening of the crack defects as well as the drastic reduction of silver content in the films. The black oval represents the later stages of etching, when the silver is almost completely etched away, and the SERS enhancements seem to be dominated by the inter-crystallite gaps that narrow down as the gold rich crystallites get closer. The random surface roughness due to the rounding up of gold rich crystallites also contributed to the high SERS activity during later stages of etching.

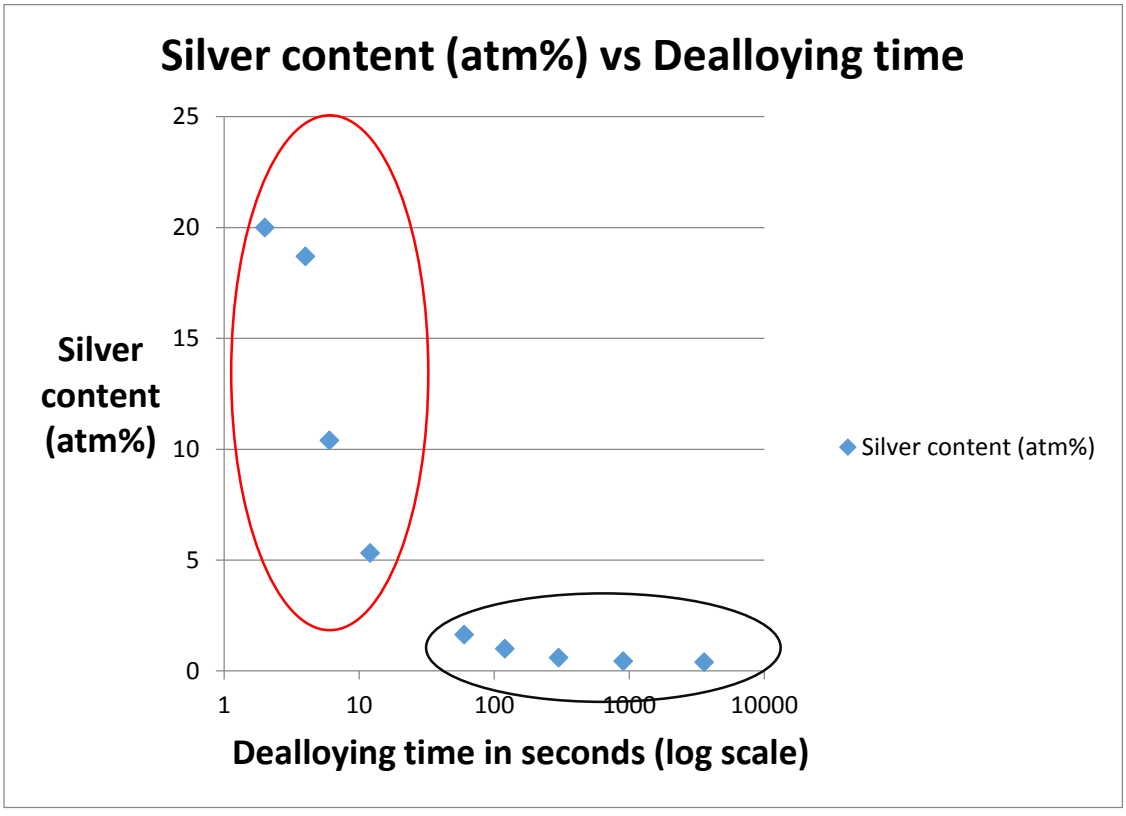

Figure 25. Atomic content of silver measured after dealloying at various times from 2s-1hr.

Chapter 5 - Patterning NPG into Discrete Disk Shaped Structures (NPG Disks) with Extremely High Enhancement Factors

5.1 Significance of NPG and Evolution of Different Types of Revamped NPG Substrates

In the previous section we understood that NPG without any structural modification does not exhibit very high enhancements. This is due to its in-plane structural features as well as smooth ligament surfaces that constrain the localized electromagnetic field strength to less than the limit for SERS-based single molecule detection. There are mainly two routes to enhance the SERS signal from NPG films. One route was discussed in the previous chapter where we were able to achieve a ~50 fold improvement in the enhancements than that reported by other research groups [53,54] through simple pore structure modifications. Another route that we would be discussing in this chapter was to pattern them or structure them into sub-wavelength isolated particles. Several groups have been able to achieve improvements in the enhancements through some structural modifications in the NPG microstructure i.e. by either introducing nanoscale cavities or by structuring the NPG film into discrete periodic patterns while densifying the microstructure. Zhang [50] observed a ~100 fold improvement in the enhancement factor caused by wrinkling the NPG film, an approach that suffers from very wide site to site EF variation as shown in Figure 26. Jiao [51] also achieved a ~100 fold improvement in the EF in mechanically stamped NPG gratings which they attributed to the combined effect of improved light coupling by the grating structure and mechanical densification of the underneath NPG film as shown in Figure

27. Wi [63] reported a 5 fold improvement from electron beam lithographically patterned porous gold disk substrates compared to solid gold disk substrates shown in Figure 28. These porous gold substrates were made using Copper as the less noble constituent of the alloy material. All these techniques still limit the use of NPG as a thin film and they suffer from major disadvantages of durability in context of extending the applications of Nanoporous plasmonics. The thin film modified NPG substrates are limited to applications that can employ planar substrates. In order to put the 3D bi-continuous porosity of NPG film to good use, we have developed a high throughput technique that can fabricate isolated NPG structures capable of integration into other different types of substrate platforms as well.

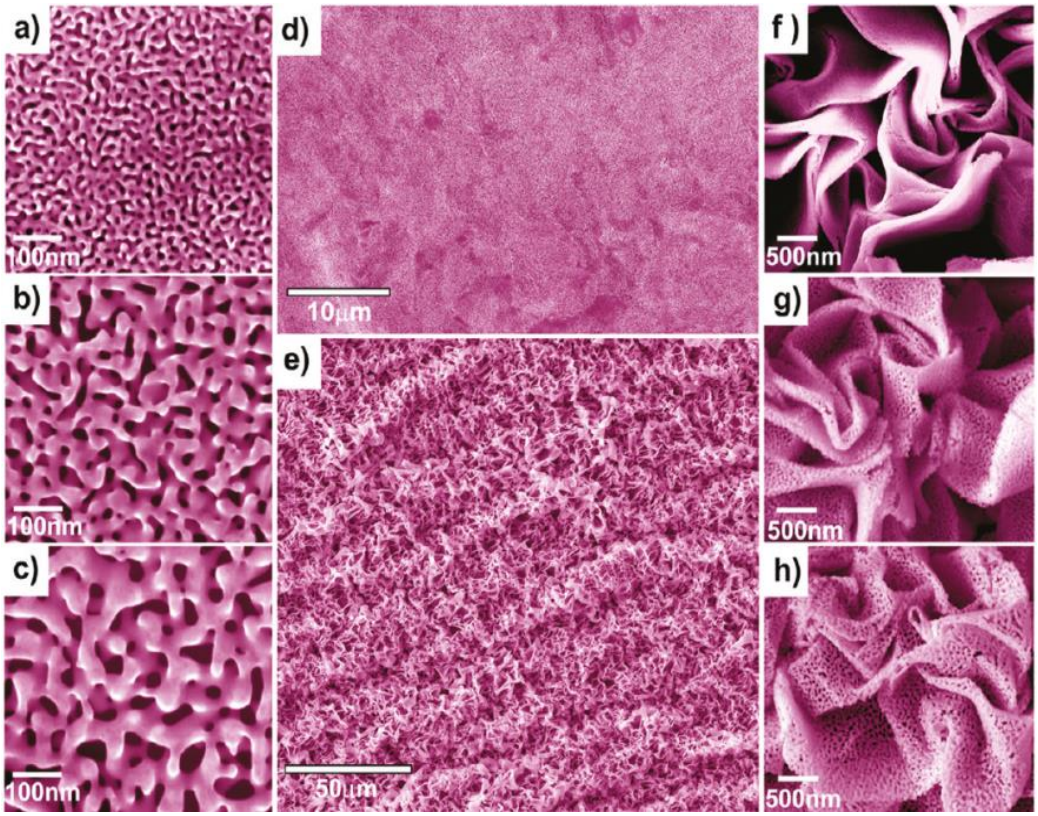

Figure 26. Wrinkled NPG films fabricated by thermal contraction of polymer underneath [50].

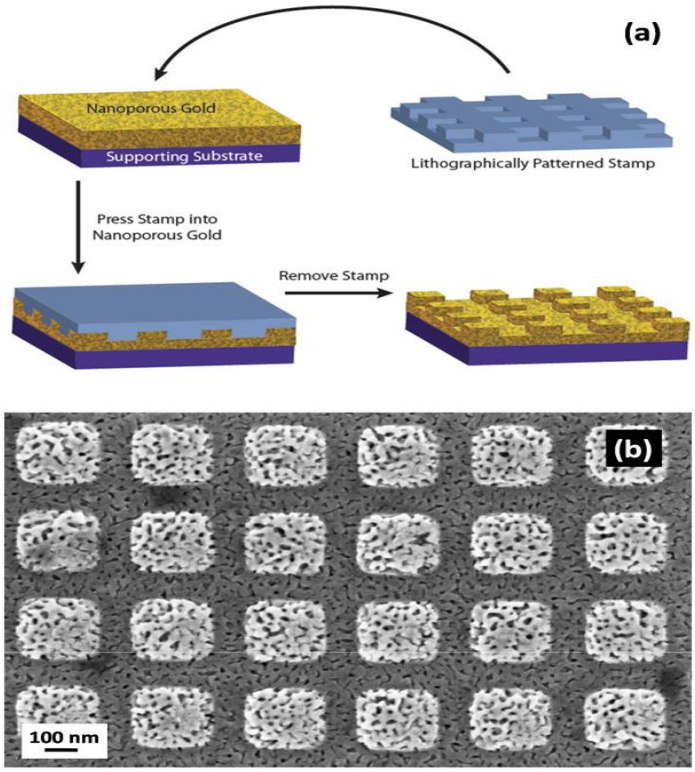

Figure 27. Mechanically stamped NPG films fabricated using Nanoimprint lithography [51].

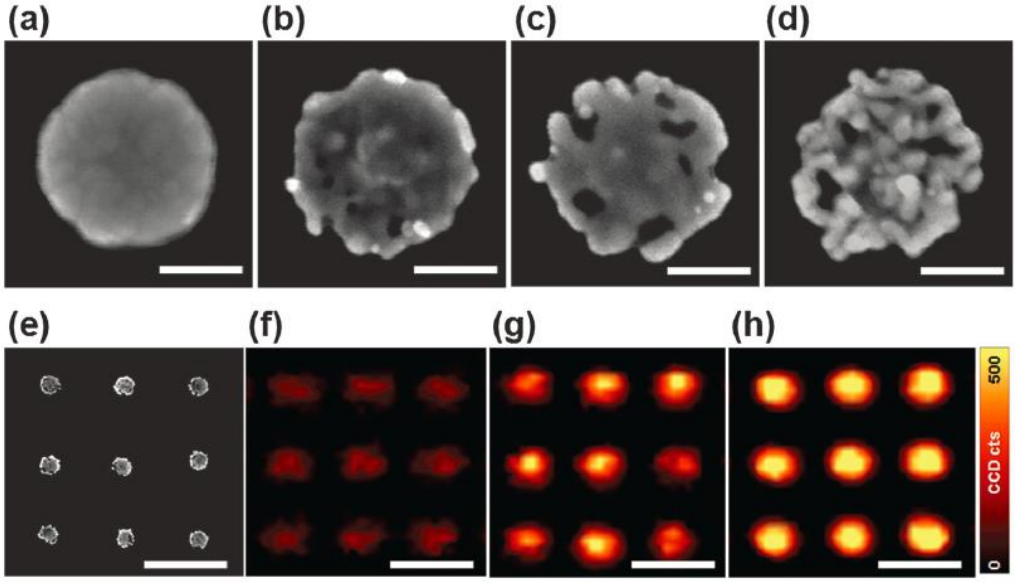

Figure 28. Porous Au nanodisks with multiple internal hot spots.

The most commonly used technique for patterning NPG film is e-beam lithography. Although e-beam lithography can provide highly reproducible SERS scattered signal, since it is a controlled fabrication method, the technique tends to be expensive with low throughput and the substrates fabricated suffer from low enhancements due to low SERS effective area. We however have developed a technique by which nanoporous gold would not be limited only to a thin film, which indeed makes the applications limited, but NPG could be employed and harvested as a novel generation of nanoparticles, thus empowering the applications of the conventional colloidal metal nanoparticles. We have developed and implemented an inexpensive and a high throughput technique coined as natural lithography [55] to pattern thin films of NPG into discrete patterned particles.

5.2 Experimental Methods for the Fabrication of NPG Disks Structures

The fabrication process flow is as shown in Figure 29. The process starts with the cleaning of highly doped silicon substrates. The substrates were cleaned in Buffer HF (10% conc.) for few minutes in order to remove the native oxide. The etching step is followed by a vigorous rinsing step in DI water and Isopropyl alcohol followed by drying in nitrogen. The cleaned substrates were then loaded immediately into the vacuum chamber for the deposition of the first layer or the supporting gold layer for NPG substrate. The gold layer was deposited at a relatively higher optimized pressure of 7 mTorr and a relatively higher source to target distance (152 mm) than for other metal depositions exhibited in the same vacuum chamber. An operating pressure higher than usual was used in order to reduce the flux of the energetic neutral bombardment on the film. The significance of the gold layer deposited at higher operating pressures was

understood in an earlier chapter. As discussed in Chapter 4, supported/constraint NPG films exhibit high density of crack formation due to the stress induced in the film due to volume shrinkage when one component from an alloy system is freely corroded. The purpose of the soft and thick gold layer was to reduce the number of crack defects. The gold sputter source used was a 99.99% pure Canadian maple leaf. Following the deposition of the supporting gold film, the alloy film was deposited using the same dc magnetron sputter deposition system with an alloy target (Au:Ag=28:72 atm%) obtained from ACI alloys.

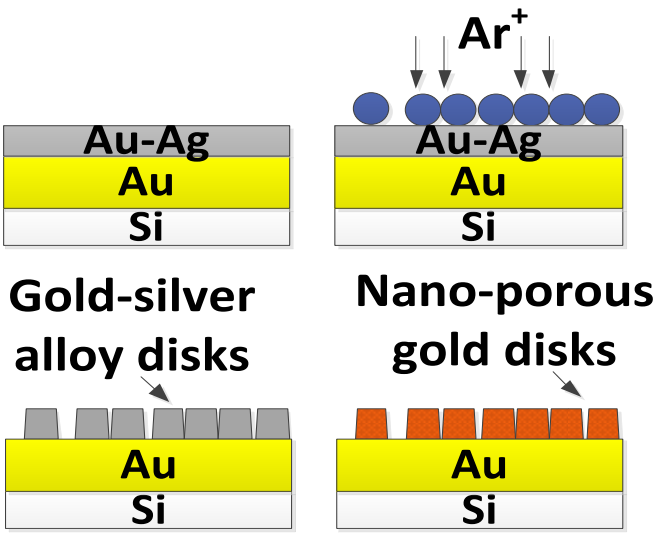

Figure 29. Fabrication process flow for supported/constraint NPG Disk substrates using nanospheres as etch masks.

As it is already known, the most common materials used as SERS substrates are composed of Gold and silver. Thus, SERS tends to be an expensive analytical technique that has limited its applications even though it was first observed about four decades ago. Thus, in order to lower the cost of fabrication, we developed the technique of Natural lithography; wherein polymer nanospheres were used as etch masks to pattern discrete structures composed of NPG as shown in Figure 29. Natural lithography was coined and

discovered in 1980s by Deckman and Dunsmuir [55]. The technique was later renamed as Nanosphere lithography by Van Duyne in 1995 [64]. Natural lithography or Nanosphere lithography is a technique in which spherical colloidal nanoparticles are used to define a large area lithographic mask. The sphere mask could be used as a deposition mask, an etch mask or a mask for printing a resist material using lithography. With the development of new synthesis methods capable of synthesizing different shapes of colloidal particles, this technique can be extended to a series of standard geometrical shapes of nanostructures. We have developed NPG disk shaped structures for which spherical colloidal nanoparticles were used. Polystyrene nanospheres with a diameter of ~500 nm were drop coated on a 75 nm thin alloy film and made to self-assemble. The solution was diluted to a ratio of 1:100 v/v% in DI water and then a 10 µL volume of the solution was drop-coated on the alloy coated substrate. The nanospheres thus coated were then used as etch masks in order to fabricate nano-disk shaped structures by etching through the alloy film. The etching was performed in an Ar plasma environment at an optimized low pressure of 2 mTorr and a RF power of 100 W. Since the spheres were just drop-coated on a hydrophobic metal surface, there seemed to be very little movement of the nanospheres on the alloy surface making the self-assembly difficult. Thus, the coverage of the nanospheres was only about ~30-40% on the entire metal coated substrate. Thus, the density of the nano-disk shaped structures was also quite lesser than desired. Nanosphere lithography requires a better method for the coating of nanospheres. Thus, in order to use spin coating for assembling the nanospheres, a thin hydrophilic oxide parting layer was deposited on top of the alloy coated substrate. The thickness of

the parting layer was chosen to be very thin so as to not increase the faceting in order to obtain disk shaped structures.

The improved fabrication process flow is as shown in the Figure 30.

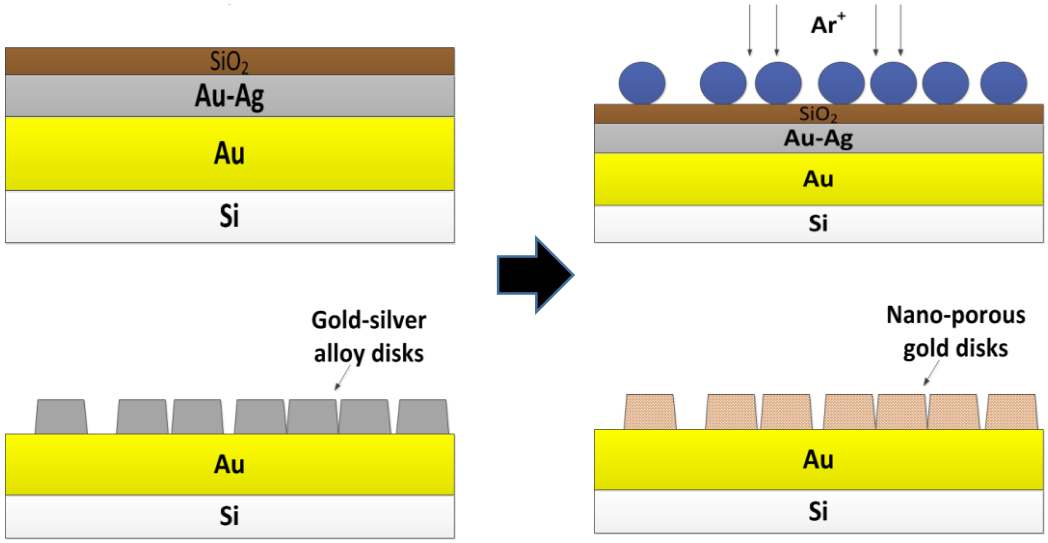

Figure 30. An improved fabrication process flow for the fabrication of periodic NPG Disk substrates with an additional hydrophilic oxide parting layer.

The hydrophilic parting oxide layer was deposited on the alloy surface to facilitate coating of uniform monolayer of hexagonally close-packed polystyrene nanospheres using a spin-coating technique. Spin coating has been known to be used for uniform thin film coatings. The oxide parting layer was deposited using a home-built DC magnetron reactive sputter deposition system with a 2 inch TORUS® axial sputter gun. The chamber was evacuated to a base pressure of 2×10^{-7} Torr and the working pressure and power were optimized to 4 mTorr and 125 W respectively. While depositing dielectric films using a reactive dc sputter deposition, the reaction between the species forming the compound, should be prevented to occur on the target in order to prevent arc discharges. Arcing or arc discharges is basically charge accumulation that occurs when the target gets

contaminated through reactions on its surface. This causes pit formation on the surface of the target that can damage the target for future use. Thus, in order to prevent arcing, a clamp fixture was designed such that the flow of the sputtering gas Argon is the highest close to the target material. Deposition of a dielectric compound material using a reactive dc sputter deposition system is dependent on two competing mechanisms, the reaction of the two vapor species to form the compound and the rate at which the target is being sputtered. Increasing the flow of Argon near the target material makes sure that the sputtering of the target material is the dominant mechanism during the deposition of a dielectric material. This prevents oxygen to build up near the target material. Also, the reaction between the two species was achieved near the substrate and none near the target. Hence, through certain equipment optimizations, arc discharges were completely prevented. Sputtering using a compound target is the easiest way to conserve the composition of the material to be deposited on the substrate. The dielectric material to be deposited was silicon oxide, used as the hydrophilic parting layer. The reactive sputter deposition of the dielectric was performed using silicon as the target material with argon as the sputtering gas and oxygen as the reactive gas. As it is already known that silicon is highly reactive with atmospheric oxygen, a high flow of argon gas was made to flow across the silicon target material preventing any contamination or an insulated layer to be deposited on the target thus keeping the plasma sustained. Thus, when energetic Ar ions bombard the target material, some of them can sputter off silicon atoms. These neutral Si atoms can condense onto the substrate forming a thin film. The oxygen inlet is kept close to the substrate as the reaction is desired to occur near the substrate. Thus, the reactive sputter deposition of SiO_2 in this work was performed using a DC magnetron sputter

deposition using Argon as the sputtering gas and oxygen as the reactive gas. The latex bead (500 nm in diameter) solution was diluted to 1:3 (v/v %) in ethanol before suspension on a silicon wafer coated with oxide. About 10 µL solution was dispensed on the center of the substrate. The spin coating method used consisted of a two-step process, the initial slower speed (500 rpm) was used for dispensing the solution uniformly all over the substrate which is called as the dispense step followed by a final speed of 1500 rpm to reduce the number of voids that may form which is used to thin the film. Thus, uniform hexagonally close packed polystyrene nanospheres as shown in the scanning electron micrograph in Figure 31(a), were obtained using the above mentioned spin coating technique. The densely packed nanospheres were then isolated or reduced using a controlled reactive ion etching process in oxygen chemistry. The reactive ion etching was performed in CCP geometry with a working pressure of 2 mTorr and a power of 100 W. The isolated polystyrene nanospheres were then used as lithographic hard masks for patterning the film underneath. Hence, a planar large area Ar ion milling or Ar sputter etching was performed at a working pressure of 2 mTorr with a RF power of 75 W to form isolated periodic arrays of alloy disks. Using the hydrophilic parting layer of oxide underneath, the nanospheres were removed using an oxide etching buffered HF solution for few seconds. Finally nanoporous gold disks were formed after selective dissolution of silver in 70% concentrated nitric acid under room temperature conditions. Different pore sizes can be obtained for NPG as discussed earlier based on the dealloying time, the initial alloy composition and the temperature. However, the supported and patterned NPGdisk substrates were tested for their effect on SERS response without any significant changes in the pore structure. The pore size studied for NPGD substrates, as seen from

the scanning electron micrograph, was about 7 nm. The morphology as well as the process development fabrication steps is shown in a series of scanning electron micrographs below. The different micrographs are for different important fabrication steps. The micrograph in Figure 31(a) shows a highly homogenous hexagonal close-packing of polystyrene nanospheres at a large scale. Here, the hydrophilic oxide parting layer is very significant. The thin oxide layer (12 nm) enables ~85 - 90 % monolayer coverage using spin coating with high homogeneity. The thicker oxide layer however allows ~ 100% coverage but it comes with a trade-off of the disk shape. The micrograph in Figure 31 (b) shows oxygen plasma reduction of the spheres. The subsequent images show the side view and the top views of the perfectly circular shaped NPGdisks (75 nm thick) sitting on a hexagonal gold pedestal (~150 nm thick). The morphology of the porous network for both patterned (Figure 31 (e)) and unpatterned NPG films (Figure 31 (f)) is exactly similar. The composition for the NPG films was estimated to be <10 % using a JEOL energy dispersive spectrometry system (EDS).

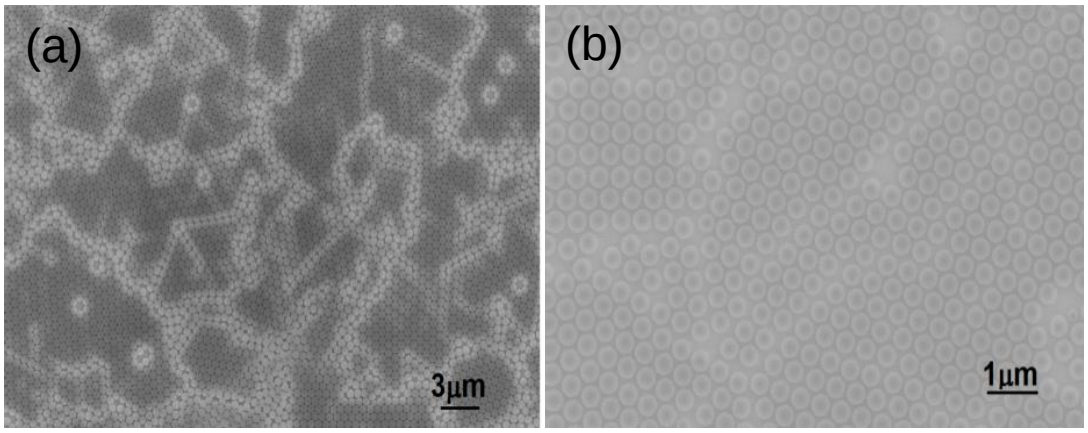

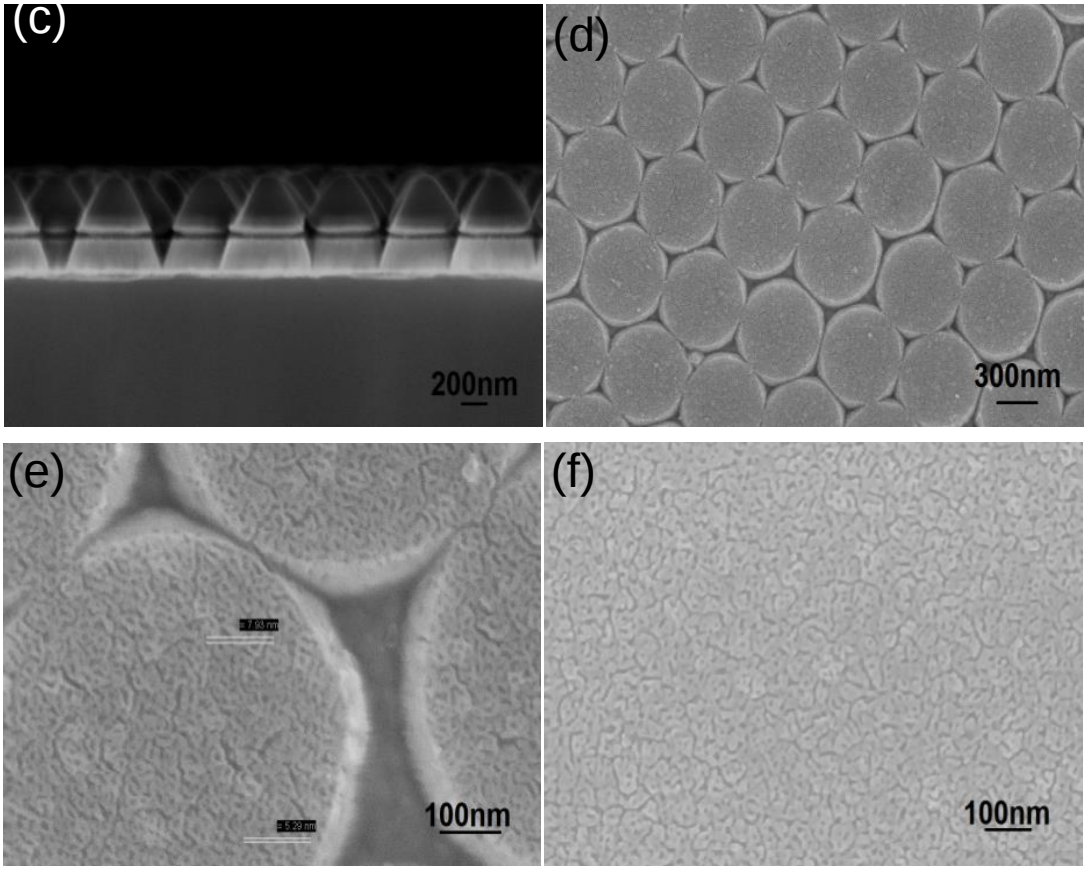

Figure 31. (a)-(e) SEM micrographs for different stages of fabrication, (f) SEM image of un-patterned NPG film with porosity identical to the patterned NPG films.

The improved fabrication technique using an additional hydrophilic parting layer developed and optimized in this work was applied to smaller dimensions as well. The SEM images for 100 nm and 200 nm NPG Disk substrates are as shown in Figure 32.

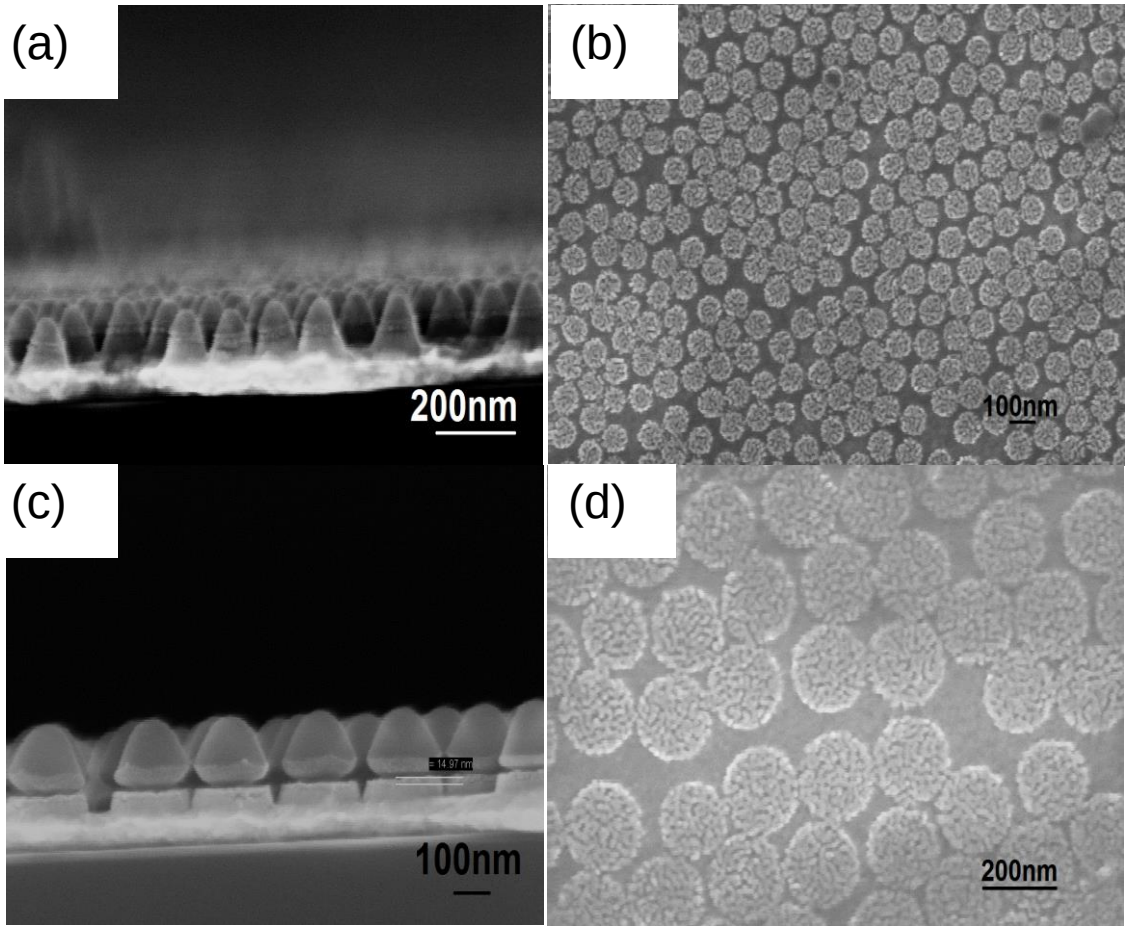

Figure 32. (a) & (c) are cross-sectional SEM images demonstrating the patterning technique, (b) & (d) are SEM images of 100 nm and 200 nm NPG Disks structures.

5.3 Determining the Enhancement Factor for NPG Disks

In order to explore the effect of patterning thin film of nanoporous gold into discrete disk shaped structures on the SERS response, the enhancement factor was estimated. We saw earlier that the enhancement factor for a thin film of nanoporous gold is dependent on the roughness factor as well as the density and size of the pores. For planar NPG films, the roughness factor was easier to estimate due to their in-plane structural features. However, for patterned NPG structures, the shape, the diameter as well as the thickness of the supporting pedestal are significant while estimating the

roughness factor. In order to accurately estimate the enhancement factor, the SERS marker is chosen in a way that the molecules are absorbed on the nanostructure surface using chemical binding or a process called as chemisorption. Thus, thiols are mostly used as the SERS marker, as they have a strong chemical affinity towards gold and silver substrates. These molecules can easily exhibit monolayer coverage and thus can be easily quantifiable, when estimating the contribution of individual units of patterned NPG disk shaped structures to the total SERS response. Also, in order to explore the various applications for NPGDisk structures including bio-medicine when released in the form of colloidal solutions of nanoparticles, the choice of benzenethiol as the analyte molecule favors the use of a 785 nm excitation wavelength typically used for bio-medical applications. This is because, as explained earlier, Benzenethiol does not exhibit an absorption peak near the excitation wavelength used in this work. Thus, a self-assembled monolayer of benzenethiol was formed by immersing the substrates in a 5mM benzenethiol solution with ethanol as the solvent for about 30 minutes followed by a 1 min rinsing in ethanol [40].

As it was discussed earlier, the average enhancement factor can be calculated by estimating the number of molecules that contribute to the observed photon count rate and then dividing this number by the number of molecules that contribute to the normal Raman spectrum using equation [12], from Chapter 2. Thus, in order to estimate the number of contributing molecules, the roughness factor was first estimated. Since the pore distribution in NPG Disk substrates was exactly the same as that for planar NPG thin films, the roughness factor using equation [13], from Chapter 3, was estimated to be 22. However, an additional area factor had to be estimated since the Nanoporous gold is

in isolated and a different form. The porosity was estimated to be 34% using image analysis from the high resolution SEM images. The mean pore size was calculated to be 7 nm. The effect of different pore sizes on the optical response of NPGDisks was kept for future studies. The area factor was estimated to be 6.3 × area of the single disk for NPG in isolated disk shaped structures.

The SERS intensity was estimated for a single disk and for the Raman peak of 1574 cm^{-1}. The effective roughness of the NPG is 6.3 and thus the number of molecules contributing to SERS signal is the product of the area of a single disk, the roughness of the porous structure, the laser spot area and the density of the BT molecules. The density was assumed to be around 6.8×10^{14} molecules/cm^2. Thus, there are ~8.4×10^6 molecules that contribute to the observed SERS intensity of 1.262×10^5 counts/mW. The spot area of the laser is ~1 μm^2 and almost 5 NPG disks can be accommodated in that area. N_{SERS} was thus estimated to be 4.2×10^7 molecules for the SERS intensity of 6.5×10^5 photons s^{-1} mW^{-1}. Placing different values in the equation [12], from Chapter 2, yields the SERS enhancement factor for a single disk as 3-5 × 10^8, depending on the method of obtaining the normal Raman spectrum for Benzenethiol. This shows a promising improvement in the enhancement factor, almost by a factor of ~450, than the enhancements obtained for thin films of unpatterned nanoporous gold. Thus, without any structural modification to the porous network of NPG, just through patterning the NPG film into isolated disk shaped structures, we were able to achieve a very high improvement in the EF, never been observed for NPG. This rise in the enhancement can be explained through the existence of plasmonic coupling between the NPG porous network and the external shape of the patterned NPG disk structure.

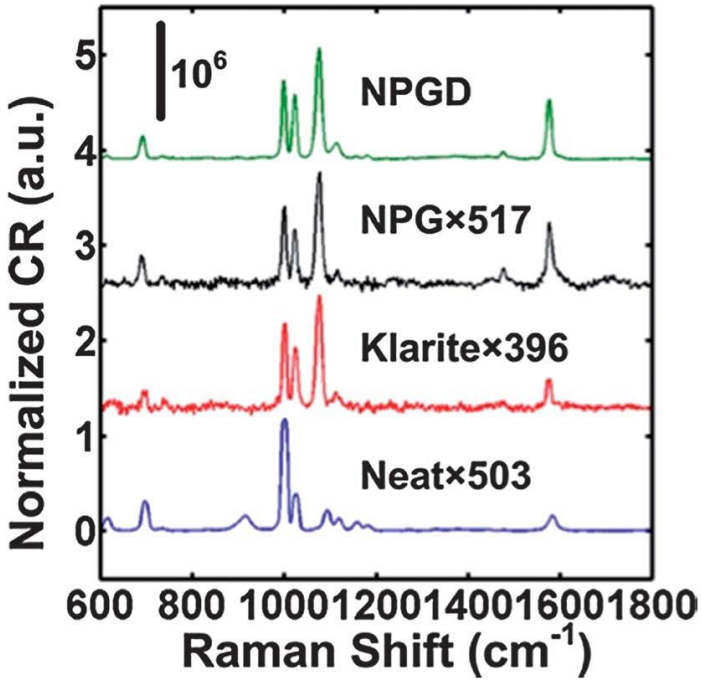

Figure 33. SERS spectra comparing commercial available Klarite® substrates, unpatterned NPG films and patterned NPG Disk substrates [13].

Thus, in conclusion, we have successfully developed a process and discovered a new generation of nanoparticles that exhibit a synergy of large SERS effective area, high density of hot spots and tunable plasmonics. These can open up numerous molecular sensing opportunities as compared to conventional colloidal gold nanoparticles due to their higher sensitivity as well as the additional dimension of tunable porosity. A single NPG disk particle can exhibit an enhancement of ~10^8 which is four orders of magnitude higher than the best colloidal nanoparticle (Silver or Gold). High improvements in the enhancement were achieved through a simple, yet high throughput and less expensive procedure of nanosphere lithography. This methodology makes NPG not just interesting as a thin film substrate, but it can be extended and harvested as nanoparticles with a tunable mesoporous network empowering the applications of modernly used colloidal nanoparticles. This improved enhancement technique will generate a higher interest in

using the various significant advantages of NPG for sensing applications without making it obsolete.

Chapter 6 - Nanoporous Plasmonics on Optical Fibers

6.1 Introduction and Significance

SERS provides a highly sensitive detection platform for the development of next generation bio-sensing devices. Rapid and highly sensitive detection permits point of care applications, early detection of diseases and faster treatment of patients. Additionally, SERS can be used as a multiplex detection tool for simultaneous detection of multiple analyte molecules using a single light source. SERS based techniques have the proficiency to be miniaturized and portable, while being easy to operate, enabling sensitive detection of multiple analyte molecules. Conventionally, optical fibers have been the medium for long distance communication mainly due to their large bandwidth and low attenuation. Optical fibers can confine light inside their core and when coated with protective layers can be made flexible for long distance telecommunication networks. Additionally, they can also significantly enhance the SERS signal when coupled with metallic nanostructures.

Optical fiber substrates are a potential means of extending SERS into practical applications now more than ever. This could not be accomplished a few years ago, but with the advent of new types of nano-materials and new types of in-expensive technologies like nanoskiving [65], nanoimprinting [66] and others for the fabrication of metallic nano-structures, these substrates can be practically realized and be facilitated in a compact sensor platform. The small cross-section of optical fiber substrates provides an unobtrusive platform for remote sensing applications. This advantage of being able to spatially separate the operator from the sensing environment makes optical fiber sensors

highly desirable while sensing toxic or hazardous chemicals. Additionally optical fibers minimize the use of bulk optical instrumentation, thus realizing miniaturized portable analytic devices. Optical fibers also remove the need for optical alignment due to the availability of fiber-based lasers, couplers and spectrophotometers, thus allowing all optical interrogation. In summary, optical fiber sensors can have applications in *Remote and in-vivo sensing, Biomedicine* [67,68] since their small cross section is minimally intrusive for in-vivo interrogation, *Neuroscience* [69] through a combination of optical and electrical multi-functionality, *Plasmonics and beam shaping* [70-73].

Recently, there have been numerous reports about integrating SERS substrates on optical fiber platform to enable in-situ and in-vivo applications, while assembling into a compact low cost system. The first SERS probe was demonstrated by Mullen in 1991[74]. In the following years of research on optical fiber SERS sensors, Stokes [75] reported and developed nanoparticle based optical fiber SERS sensors, where the nanoparticles were coated at the distal ends of the optical fibers. It is already understood for the nanoparticle based planar substrates that nanoparticles tend to form random morphology and there is less control over the spacings between the nanoparticles. This leads to uncertainty in the observed SERS signal. SERS signal intensity obtained from nanoparticle aggregates may be extremely high sometimes but the occurrence of this high enhancement event due to plasmonic coupling of fields close to each other is extremely rare and thus, on average the enhancements are typically low and uncertain. The uncertainty in the SERS signal is similar for nanoparticle based optical fiber SERS sensors as well. Viets and Hill in 2001[76] and 1998 [77] respectively reported similar optical fiber sensors having roughened tips. Polwart in 2000 [78] was able to immobilize

nanorod structures on optical fiber facets using a functional layer of 3-aminopropyltrimethylsiloxane (APTMS). With the advancements in nanofabrication technologies, there have been numerous reports on optical fiber SERS sensors recently. Electron beam lithography is the most common method of fabrication and has been used to fabricate metallic nanorings, nanodots and other types of nanostructures on the distal ends of the probes [64]. Nanoimprint lithography and nanoskiving are the most promising techniques amongst other common fabrication techniques of electron beam lithography and focused ion beam milling. Nanoimprint lithography was recently demonstrated [66] to replicate rod like structures from cicada wings and anodized alumina templates on optical fiber tips. Nanoskiving [65] is a relatively new technique that combines thin film deposition of a metal on a topographically contoured substrate with sectioning using an ultramicrotome. Some of the recently reported techniques used for fabricating nanostructures on optical fibers are as shown in the following figures.

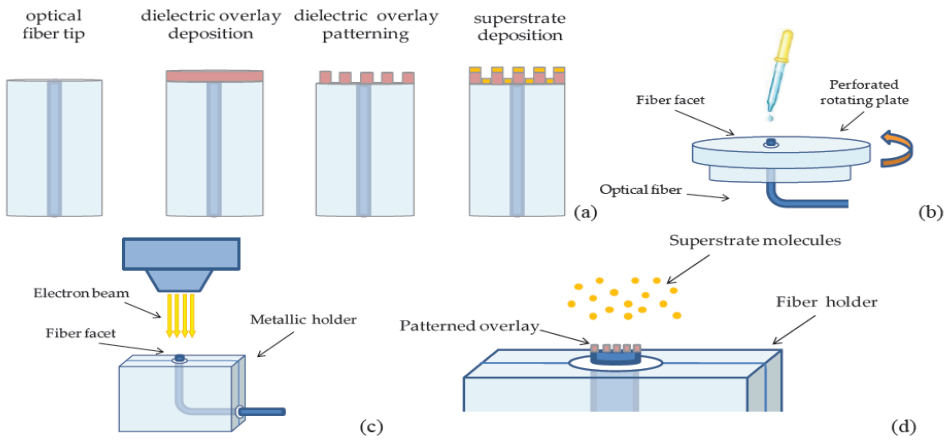

Figure 34. Fabrication process flow for hybrid metallic and dielectric nanostructures using electron beam lithography [64].

Figure 34 describes the technological steps for fabricating hybrid metallo-dielectric nanostructures using e-beam lithography. The figure emphasizes on the design

of a customized chuck and a set of metallic holders developed to enable spin coating process on the flat tips and easier patterning using e-beam lithography.

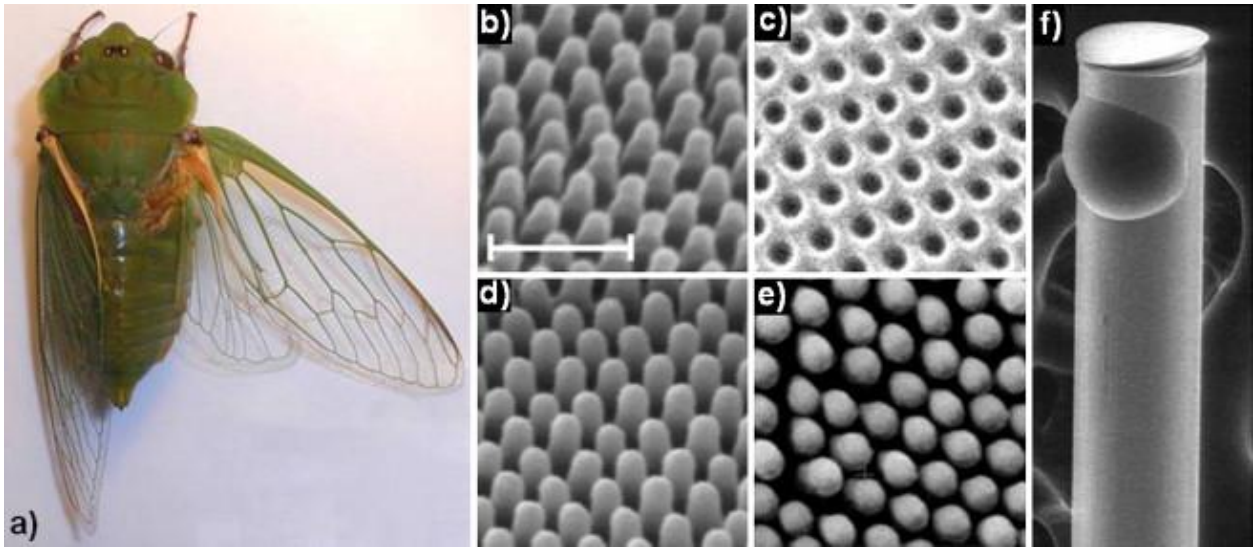

Figure 35. Replicating biological nanostructures from cicada wings using nanoimprinting [66].

Figure 35 demonstrates the technique of nanoimprinting, wherein the antireflection biological nanostructures on cicada wings are replicated on optical fiber facets. The structures are employed as a master template and cast into a silicon rubber to form a mold. Polymer coated on a fiber tip is then imprinted against the silicone mold to form the replica of the nanostructures as shown in scanning electron micrograph in Figure 35(d). The polymer structures are then coated with silver to form a SERS tip sensor.

The Figure 36 below is a demonstration of Nanoskiving. This technique was aimed at fabricating structures at a considerable lower cost than most of the conventional top-down techniques and would replace them in selected applications. The technique can be used to fabricate nanostructures with compositions and geometry that are challenging and expensive to fabricate using conventional techniques. Using this technique, the

structures can be fabricated on arbitrary substrates including curved surfaces very easily, while retaining in-plane positions of the structures. One such surface is fabricated with a periodic array of plasmonic nanorings as shown in the figure below.

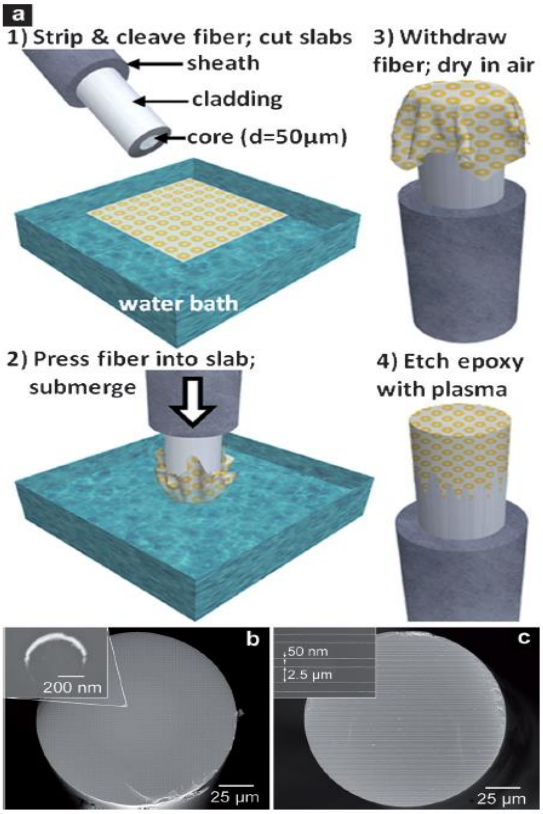

Figure 36. Schematic illustration for the procedure of transferring plasmonic nanostructures to cleaved fiber facets – Nanoskiving[65].

The procedure for the fabrication of nano-rings on optical fiber facets is a combination of thin film metal deposition and thin sectioning using an ultramicrotome. Microtomy was a tool used thin sectioning of biological samples to be images using optical microscopy. With the advancements in electron microscopy and until the invention of transmission electron microscope, microtomy began to be used to slice sections as thin as < 100 nm. Nanoskiving is a technique that utilizes these sections to transfer patterned nanostructures on any type of substrates in a simple manner.

6.2 Fabrication Process and Results

6.2.1 NPG Sensors on Optical Fiber Facets

A DC magnetron sputter deposition system was used for both the deposition of gold and gold-silver alloy films as shown in the previous chapter. Prior to fabricating NPG on silica optical fibers, the process was first performed on flat glass cover slip substrates to better understand the adhesion issues. Optical fibers work under the principle of total internal reflection. They consist of a light carrying core and a cladding layer that surrounds the core acting as mirror walls. Light is bounced back and forth from the mirror cladding walls and thus guided through the length of the fiber. If the core is large then more optical power can be transmitted through it. The core has a higher refractive index than the cladding. Since the cladding layer has a lower refractive index than the core, the cladding layer does not absorb any light and thus it bounces back as it were a mirror.

Silica optical fibers purchased from Polymicro technologies, have a core of 50 micron with a high concentration of hydroxyl (OH) group and a 2.5 micron doped silica cladding with a 5 micron polyimide jacket. The polyimide jacket layer improves the durability and the bending radius of the optical fibers. However, the adhesion between the polyimide jacket layer and the subsequent layers of metal was shown to be poor. Thus, during the fabrication of NPG sensors on optical fiber facets, the polyimide was burnt off in high temperature and ambient conditions using a 4” minibrute tube furnace. The facets of the optical fibers can be treated as flat substrates. However, since the microscopic cross-section of the optical fibers is so small, the substrates were brought

very close to the target in order to decrease the spatial uniformity of the deposition and rotated at 1 revolution per min (rpm) to minimize the deposition on the sides.

After burning the polyimide jacket off, the fibers were coated with a semi-transparent thin layer of supporting gold film, in order to keep the attenuation to a minimum. Thus, ~15 nm of thin gold was deposited on the optical fiber facets using an optimized DC magnetron sputter deposition system. A gold-silver alloy film of 75 nm thickness was then subsequently deposited for the fabrication of NPG. Free corrosion dealloying was then performed in a concentrated nitric acid solution to fabricate NPG on optical fiber facets.

It is known that substrate supported configuration of NPG exhibits a high density of crack distribution. In previous chapter, the deposition conditions of the supporting gold layer film were optimized in order to minimize the crack densities embedded in NPG films during the process of dealloying. However, for light to come out from the core region of the optical fiber without very high attenuation, the metal supporting layer was made extremely thin. The thin bombarded metal films exhibit higher stress than soft and thicker films. The crack defects formed during early stages of dealloying penetrate throughout the thickness of the film. This can be clearly seen from the SEM images shown below. The images shown are for before and after dealloying on the 55 μm optical fiber facet.

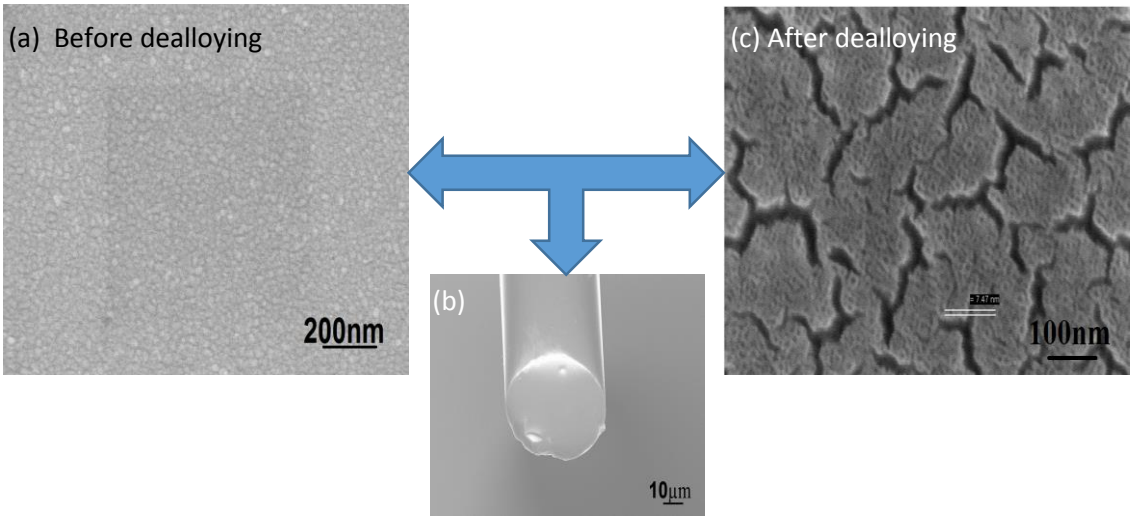

Figure 37. Scanning electron micrographs for NPG sensors on optical fiber facets (a) As deposited gold-silver alloy film on fiber facets, (b) Optical fiber facet coated with NPG, (c) Pore morphology and high density crack distribution of NPG.

6.2.2 NPG Sensors on Tapered Optical Fibers with a Large Cylindrical Interaction Area

Optical fiber sensors with nanostructures on fiber facets, though are easy to fabricate suffer from many limitations. Since light is propagating through the core region of the fiber, only the nanostructures surrounding the core area can be excited for SERS activity. This decreases the detection sensitivity of the fiber SERS sensors. These sensors also exhibit limited transmission efficiency since light is guided only through the core region and there exists a transmission loss between the sensing and the non-sensing portion. Optical fiber sensors with structures fabricated on facets exhibit challenges in obtaining clean defect free tips. Defect free tips can only be obtained using an expensive method of CO_2 laser cutting and polishing. Facets that are defect free for optical fibers are extremely rare in the case of mechanical cleaving using a diamond scribe.

An alternative method is to fabricate nanostructures on tapered probes that also have a cylindrical portion [79]. The tapered fiber sensors with cylindrical ends can provide a leakage free transmission between the sensing and the non-sensing portion, since the tapered portion of the fiber sensor acts as the mode converter that can reduce the transmission loss, thereby increasing the utilization of the excitation as well as the collected light. These sensors can now have higher coverage of the analyte molecules and thus higher interaction area between the laser light and the metallic nanostructures fabricated on them. Thus, the SERS effective area can be improved and thus the sensitivity of the final device would increase. When light is coupled to the back end of the optical fiber, while passing from the tapered portion to the cylindrical area of the probe, light exists in the form of an evanescent wave, which could excite metallic nanostructures, thus generating surface plasmon resonance effect and causing the enhancement of the localized fields. Also, the SERS light radiates isotropically and some of the light is coupled back to the probe and detected as signal. Tapered end fiber sensors can also allow defect free fiber facets. These sensors are minimally invasive and can exhibit easier in-situ penetration for biosensing applications.

One of the most commonly used method for tapering ends of an optical fiber is mechanical pulling of a heated fiber. In this method, a strong CO_2 laser is used to heat the fiber and then pulled until the fiber breaks. This method is usually used when you need a long fiber tip. The method is faster than the chemical etching method but it needs an expensive set-up. Another method that is cheaper than other tip fabrication techniques is chemical etching using buffered HF solution. Chemical etching is carried out using a balanced solution of hydrofluoric acid and ammonium fluoride.

The reaction of the etching method can be written as

$$SiO_2 + 4HF + 2NH_4F \rightleftharpoons 2NH_4^+ + SiF_6^{2-} + 2H_2O\ . \quad (16)$$

The desired tip can be achieved either at the cleaved end of the fiber when the fibers are dipped in the bulk of the solution or in the meniscus region where an etch stop is created by an organic layer and the tip is formed where the fiber enters the etchant solution. However, the tips formed using a simple chemical etching method, tend to exhibit a high degree of surface roughness. This occurs mainly due to environmental changes, vibrations, temperature drifts, etc.

In this work, optical fibers were tapered using the *tube etching* method [80], a chemical etching method with a balanced composition of the hydrofluoric acid and the ammonium fluoride buffer solution, wherein the polyimide jacket is stripped off after the etching. In the tube etching method, the tip formation occurs inside a cylindrical cavity which is created by the polyimide jacket covering the optical fiber. The polyimide coating is not removed prior to tapering the probes in buffered HF solution. This procedure allows a better control over the type of tip formation, the cone angle and the surface roughness during the tip formation. The procedure overcomes the limitations of the conventional etching techniques. The tube etching method is as shown in the figure.

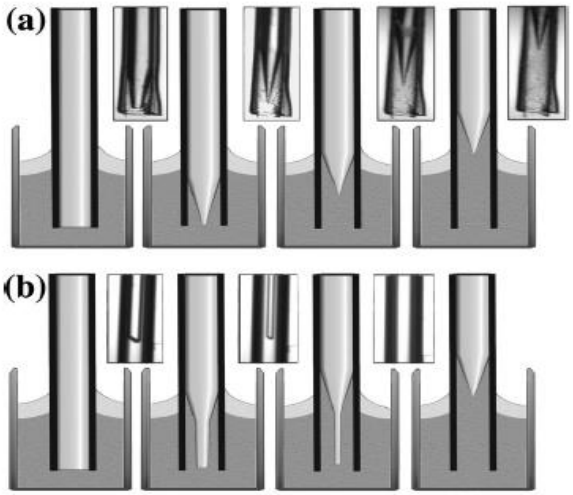

Figure 38. Tube etching method for formation of tapered optical fibers [80].

As shown in the Figure 38(a), the tube acts as the HF impermeable layer. The tube ensures that no HF can penetrate through the jacket above the interface between the acid solution and the organic etch stop layer. Optical fiber inside the jacket however is thinned due to the diffusion of HF through the jacket and thus the tip formation starts at the lower end of the fiber; at the position of the interface between the HF solution and the organic overlayer. HF vapor etching is also stopped using an etch stop layer of oil covering the buffered HF solution. Thus, both the polyimide jacket as well as the etch stop layer prevents any thinning of the glass in the upper end of the fiber and only the lower end is attacked. As soon as the lower end starts to be attacked by the acid solution, the tip begins to form. Once the tip is formed, the shape of the tip is maintained while the tip shortens inside the tube. The tube etching process is a self limiting process. This is significant in obtaining less surface roughness near the tip area as observed in conventional chemical etching methods. The quality of the tip is maintained even if the etching is continued further. The figure below shows that initially, the edges of the optical fibers are etched slightly faster than the center. As soon as a preliminary conical

taper tip is formed, HF starts to diffuse to the upper region of the fiber. Thus, higher taper cone angles can be achieved with negligible surface roughness in a controlled manner, since the taper formation is no longer a sensitive surface phenomenon but occurs inside a plastic protective container.

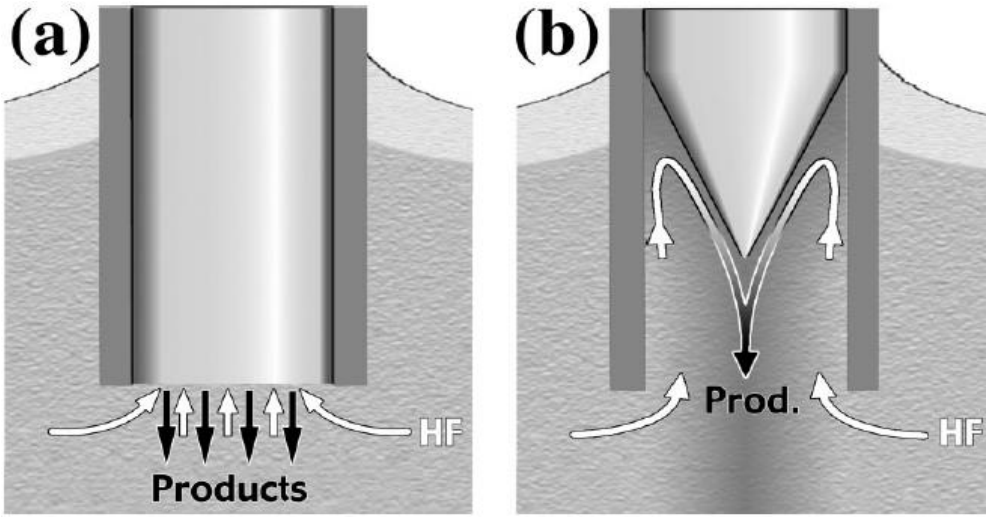

Figure 39. Schematic of the convention controlled mechanism demonstrating the (a) diffusion and (b) convection controlled etching of optical fibers [80].

Following the tube etching method, the polyimide was then burnt off in a 4" minibrute tube furnace at ~600ºC in order to expose the tapered region of the probe. Polymer coatings are responsible for the success of multi-mode silica optical fibers since they provide mechanical and chemical protection to the optical fibers from the surrounding environment and properties that can meet customer requirements. Polyimide in particular permits optical fiber operation over a wide temperature range, from cryogenic temperatures (<-65ºC) to as high as to 400ºC. These coatings are bio-compatible and chemically resistant which open up numerous applications for the optical fibers. However, we found that the optical fibers purchased from Polymicro technologies with polyimide coatings, exhibited poor adhesion with patterned metal. Thus, in order to

not compromise the durability of the probes, a buffer layer of plasma deposited polymer layer of styrene was deposited and then subsequently cross-linked using high energy Helium ions on and around the optical fibers. The conformality of the deposited film prepares a smooth surface for the subsequent deposition of metal.

A supporting layer of gold is then deposited on the polymer coated fiber using a DC magnetron sputter deposition at an Ar pressure of 7 mTorr and a power of 50 W. The source to substrate distance was decreased in order to fabricate thin and smooth films with the help of increased bombardment at smaller source to substrate distances. As explained earlier, thin films deposited using a sputter deposition system are subjected to high energy particle bombardment. These energetic particles can be either excited neutrals or electrons travelling in straight trajectories along the axis of the discharge. The energetic electrons cannot transfer their energy to heavier particles during collision. However, these electrons when bombard the substrate, transfer their energy in the form of heat, causing higher diffusion of atoms on the substrate. A thin film deposited under low bombardment conditions tends to be rough, discontinuous or island like. In order to reduce the attenuation due to a metal film on glass, the thickness was kept to a minimum. Thus, bombardment was preferable for maintaining the pore morphology of NPG films on flat substrates. However, bombardment by energetic particles comes with a price of stress related issues that was shown earlier.

The optical fibers were rotated at 1rpm during the deposition to ensure uniform deposition along the circumference of the fiber. It is already known that substrate supported/constraint NPG films exhibit high density distribution of crack defects. Thus, NPG films supported by a bombarded thin gold layer, exhibit high density of cracks, that

penetrate throughout the thickness of the film. This can be clearly seen from the SEM images as shown below.

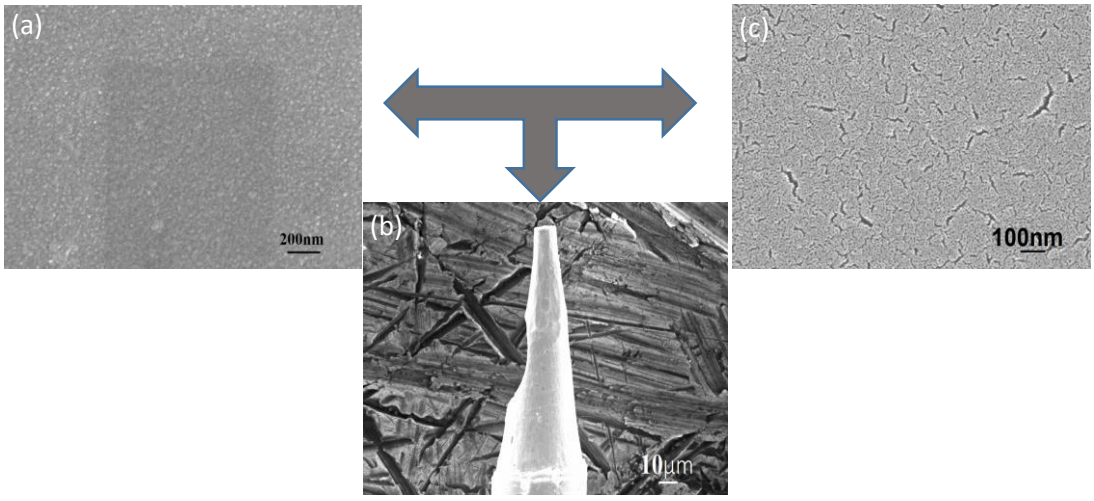

Figure 40. Scanning electron micrographs for NPG sensors on tapered end optical fibers (a) As deposited gold-silver alloy film on fiber tips, (b) Optical fibers coated with NPG, (c) Pore morphology and low density of crack distribution of NPG.

6.2.3 Patterning Sensors on Combined Tapered and Cylindrical Optical Fibers

In the previous section, thin films of NPG were integrated on both optical fiber facets and on the circumference of a tapered optical fiber reproducibly. As we have shown earlier, that even on flat substrates, NPG film without any structural or pore modification cannot exhibit promising improvements in the enhancement factor, when compared to reported and commercialized SERS substrates. We have also shown that when patterned, NPG film exhibits very high enhancements (>500 times) than the unpatterned films. Thus, a pilot optical fiber substrate with gold sensors patterned on them was fabricated using a combination of thin films and ion beam proximity lithography through a silicon stencil mask. As discussed in the previous section and as shown in previous reports, fibers consisting of both tapered region and non-tapered

(cylindrical) region exhibit higher efficiency than only tapered end fibers. Thus, using similar chemical etching conditions, combined tapered and cylindrical optical fibers were fabricated.

Optical fibers tapered using a tube etching method described earlier, were subjected to high temperatures to burn the polyimide off. Bare glass fibers were then coated with a buffer layer of styrene deposited using a Plasma enhanced chemical vapor deposition system with magnetically enhanced plasma. The schematic of the system is as shown below in the figure.

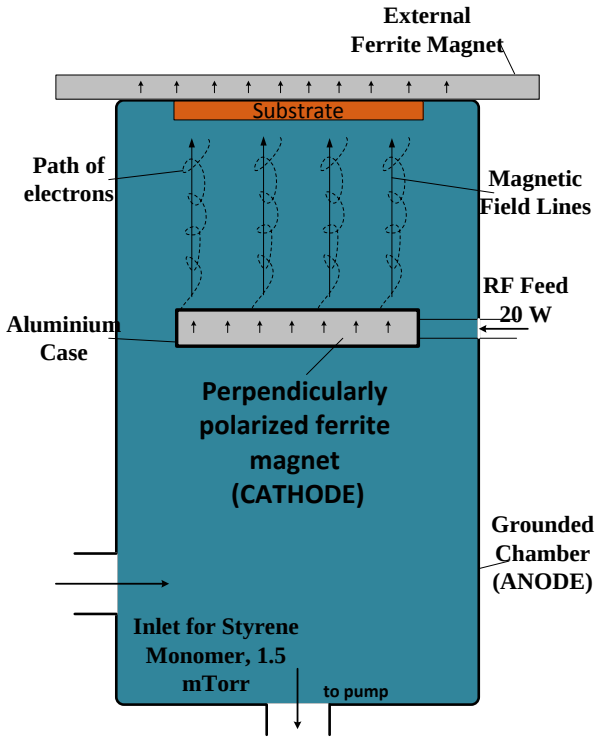

Figure 41 : Schematic diagram for the plasma reactor used to deposit negative tone styrene resist material [80].

The system chamber is pumped by a turbomolecular pump to a pressure of 2×10^{-5} Torr backed by a mechanical dry pump. Styrene is introduced in the chamber at a

pressure of 1.5 mTorr and the deposition is carried out at 31.5 mTorr using a throttle valve. The deposition rate achieved for plasma deposited styrene is ~30 nm/min at a RF

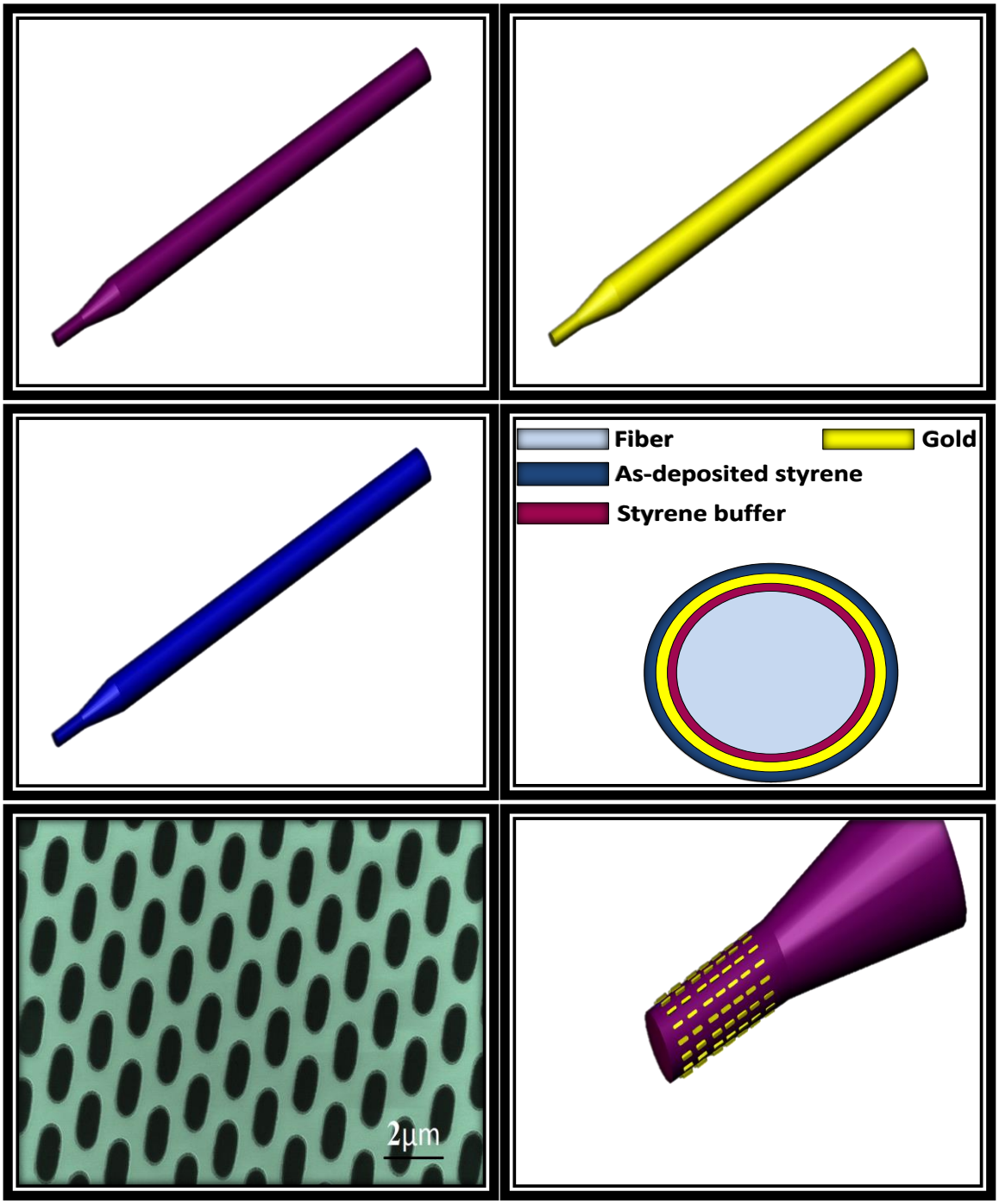

Figure 42. Process flow for the fabrication of isolated periodic metallic structures around optical fibers.

(13.56 MHz) power of 15 W using superposed magnetic fields generated from two perpendicularly polarized ferrite magnets.

The styrene coating on the fibers was then cross-linked using 50kV He ions with a multi-cusp source. As described earlier, due to the removal of the polyimide jacket, bare glass optical fibers tend to be fragile. The polymer coating thus deposited serves the same purpose as the polyimide jacket but conforms to the tapered topography of the fiber convincingly without cracking. This polymer coating also serves as the support layer for the metallic nanostructures to be fabricated. The polymer coated fibers were then coated with a gold film about 100 nm in thickness using a sputter deposition system while rotating them at 1rpm.

A second layer of styrene is then deposited under the same conditions but rather a lower thickness than the buffer layer in order to obtain better selectivity when etching the metal layer. The process flow for the fabrication of patterned sensors on tapered optical fibers is shown in Figure 42.

Ion beam proximity lithography was used to fabricate sensors around the fiber tips. In ion beam proximity lithography, a broad beam of energetic charged particles or ions bombard a stencil mask. The beamlets that transmit through, transfer the mask pattern to resist on a substrate. The stencil mask used for the fabrication is as shown in the Figure 42. The stencil mask consists of arrays of circular windows circumscribing square pads of 150 microns each over an area of 1 inch.sq. The square pads inscribed in the circular windows consist of rectangular holes with a width of 750 nm and a length of 1.5 microns. The tapered tip of the optical fiber was then aligned with the circumscribing

square holes using an optical microscope. The fiber aligned with the mask was then subjected to a broad beam exposure of Helium ions accelerated to energies of 30kV.

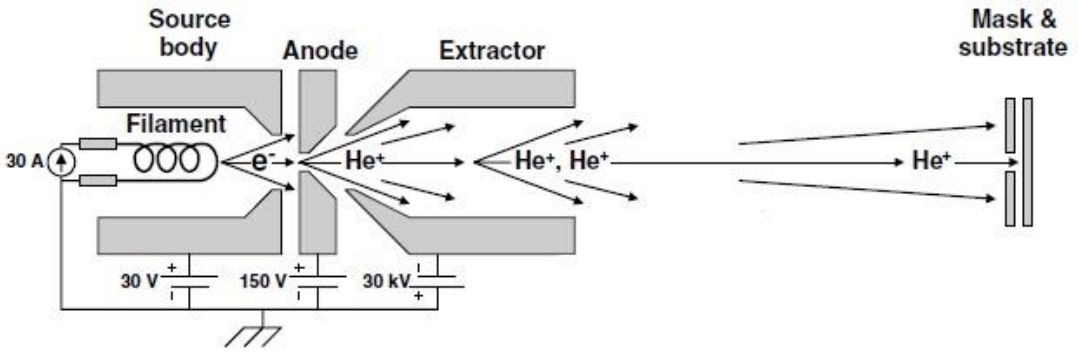

Figure 43. Schematic for an Ion beam proximity lithography used to transfer the mask pattern on optical fiber substrates [48].

With an extraction voltage of 2.3kV, the beam is about 3.5 inches in size at 30kV with a focusing voltage of ~25kV. The exposed fibers were then developed using amyl acetate to expose the patterns. As seen from the SEM images below, the alignment between the square pads opening and the tapered fiber seems to be quite good, which resulted into a dense pattern array right on the tip itself. The patterns were then transferred on the sputtered gold layer underneath, using a plasma etching tool in a reactive ion etch configuration where the substrate is placed on the RF powered electrode (cathode). Gas is fed through a showerhead anode for uniform distribution of gas and thus uniform etching. In order to etch the gold layer underneath, a simple Ar ion sputter etching was performed in the chamber as shown below.

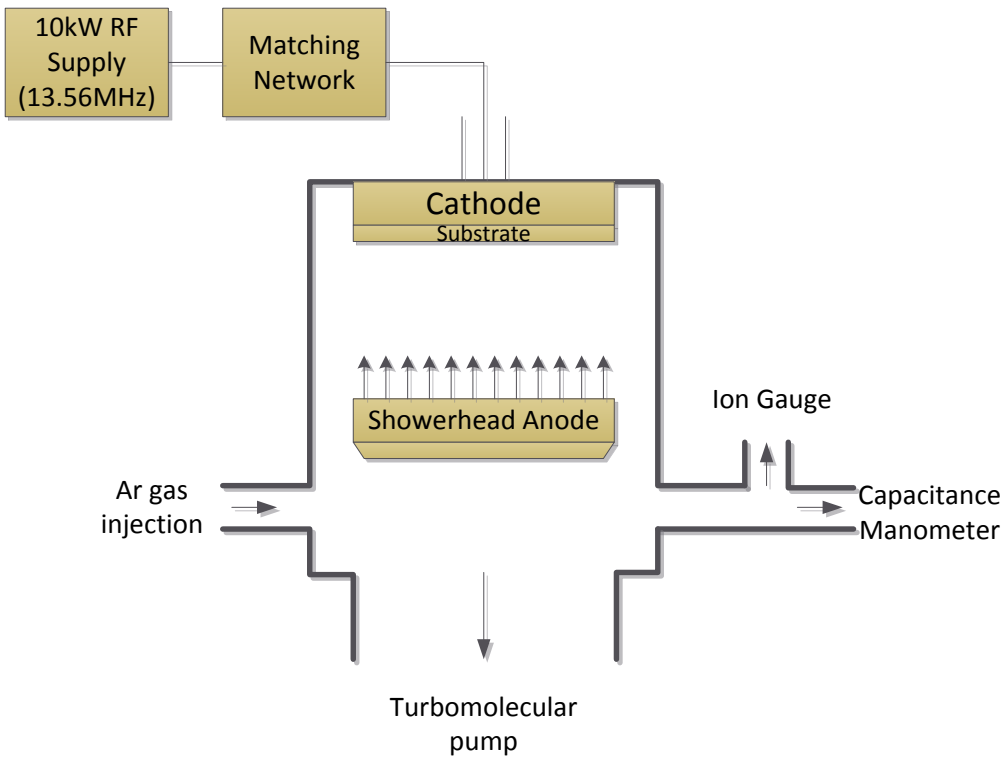

Figure 44. Plasma etching system in RIE configuration developed and optimized for metal and dielectric etching.

The plasma etching system as shown in the figure above was pumped down using a turbomolecular pump to pressures of 5×10^{-6} Torr. The etching was performed at a pressure of 2 mTorr and RF power of 75 W. The etching rate for gold is about 10 nm/min under these working conditions. The transferred pattern was then imaged using a LEO 1525 SEM and the images are as shown below.

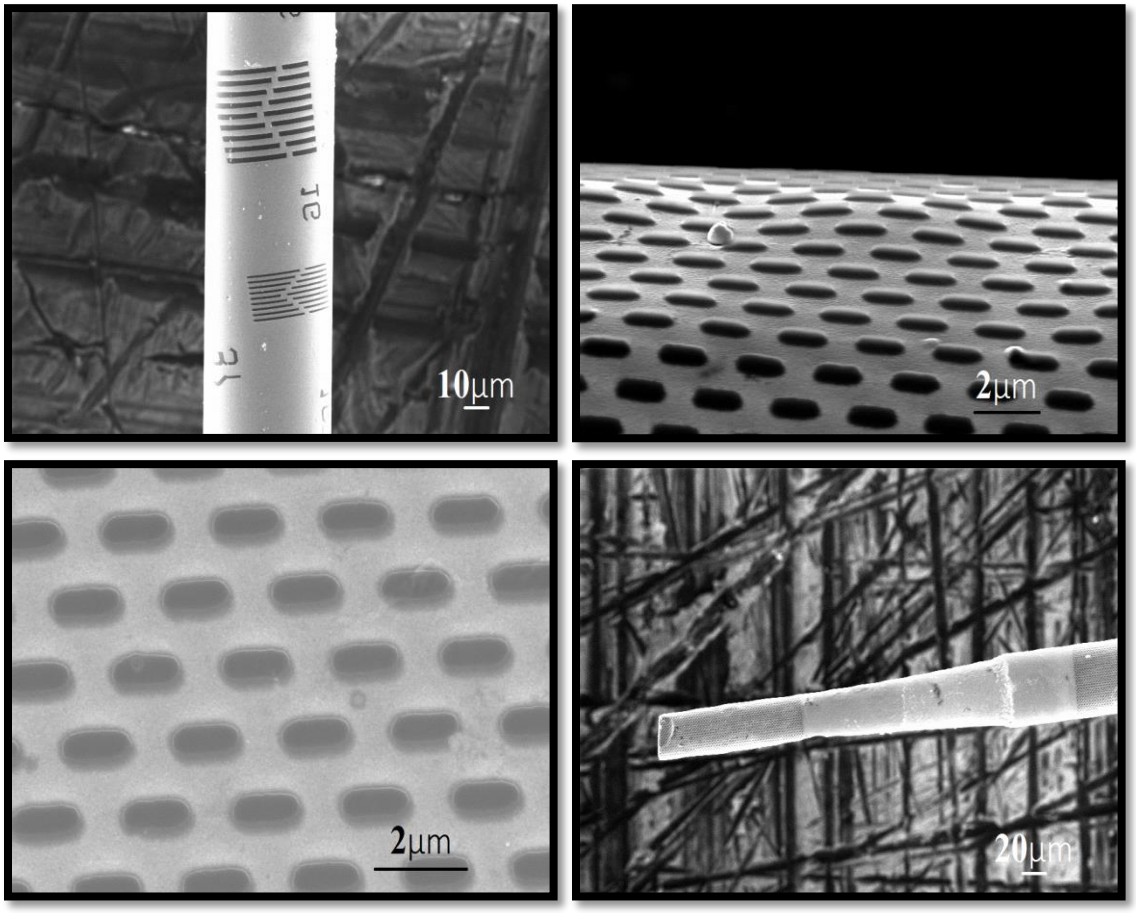

Figure 45. SEM images for resist patterns on probes using Ion beam proximity lithography.

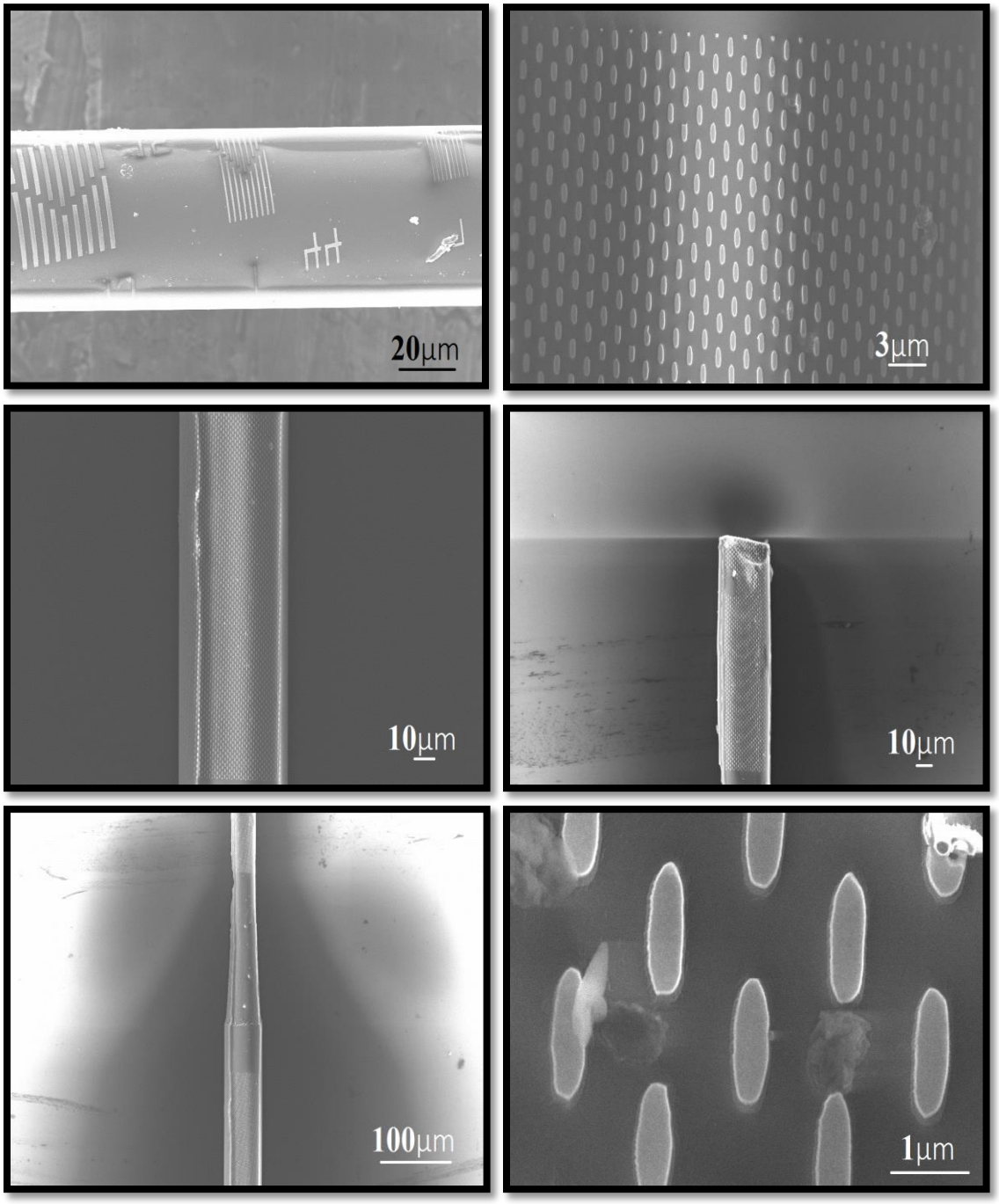

Figure 46. SEM images for gold sensors on optical fibers.

CHAPTER 7 – SUMMARY AND FUTURE WORK

7.1 Summary

In summary, the work presented here portrays significant contributions to the development of a novel generation of sensors that was demonstrated to yield four orders of magnitude higher electromagnetic intensity enhancements. The collaborative use of these nanostructures as planar flat substrates, as colloidal particle solutions and as optical fiber sensors manifested overwhelming applications than that could be achieved using conventionally available SERS substrates. We have been able to develop and optimize inexpensive techniques for the fabrication of this novel generation of plasmonic sensors. Even after more than four decades since the discovery of SERS, its applications have still been limited due to lack of available substrates that can be utilized for practical and real world applications. The key SERS substrate attributes of high density uniform distribution of hot spots, large SERS active area, high surface to volume ratio, reliability and high reproducibility were addressed. Additionally, tunable plasmonic properties that can eliminate molecular sieve effect and enable the same substrate to be used for multiplex detection were also considered and incorporated. Optical fibers that benefit from applications in remote and harsh environments were integrated with sensors having plasmonic properties.

Gold nano-island substrates fabricated using evaporation although known, exhibited poor durability for even solvents like water. Thus, high pressure sputtering was opted and optimized to fabricate gold nano-island substrates with sizes smaller than that could be defined using conventional lithography or particle synthesis techniques.

Sputtering also provided better control over the nucleation of nano-islands than evaporation. This gave us better control over the size of the nano-islands and the spacing between them, ultimately giving us control over the location and density of hot spots. Sputtering also provided higher adhesion due to energetic particle bombardment. By controlling the spacing between the nano-islands, we were able to achieve an enhancement of 5 million which is 5 times higher than the best commercially available substrate; does not involve complicated lithographic techniques and is easily scalable to large areas. Sputter deposited gold nano-island substrates exhibited high degree of structural uniformity over the entire substrate area and also from substrate to substrate.

The high intensity obtained in SERS is attributed to the interaction of molecules with regions of intense localized electric fields (e.g., *hot spots*) in nanostructured metallic substrates. These hot spots were mainly observed in nanoscale gaps between metallic nanostructure dimers and sharp metallic tips and curvatures. High density of hot spots was the major motivation for leaning towards Nanoporous plasmonics and since gold is more stable than silver, Nanoporous gold was the optimum choice. Thus, nanoporous gold (NPG), an inexpensive material was then explored for SERS applications. As reported by several research groups, we were able to demonstrate that Nanoporous gold without any structural or pore modifications are not very promising SERS substrates. We were able to demonstrate ~50 times higher enhancements by altering the porous structure of NPG through simple processing parameters. While studying the evolution of the pore structure, we were able to report smallest pore sizes ever reported in the literature under room temperature conditions.

Another route for improving the enhancements was to explore the effects of making NPG structures. We explored the effect of patterning NPG film into isolated disk shaped sub-wavelength structures that can not only limit the applications of NPG to thin film planar substrates, but can also be integrated on any substrate platforms by releasing them in solution form. In order to keep the cost of fabrication to a minimum, an inexpensive fabrication technique of natural (nanosphere) lithography was developed, optimized and improved upon for the fabrication of isolated NPG disk structures. The effect of patterning the NPG film into sub-wavelength discrete disk (NPGDs) shaped substrates resulted into an improvement of ~500 in the enhancement factor. A single NPGD particle exhibited an enhancement of ~10^8, which is 4 orders of magnitude higher than conventional solid gold or silver colloidal nanoparticles.

Finally, for easier remote sensing and in-vivo applications, optical fibers were explored as the substrate platform. Nanosensors were fabricated on optical fiber facets, tapered end optical fibers and on tapered fibers with a large cylindrical interaction area. In the first two variants of optical fiber sensors, (1) NPG film was integrated on optical fiber facets and also (2) around the circumference of tapered end optical fibers using thin film deposition and a short wet chemical etching process. In the last variant of optical fiber sensors, gold sensors were fabricated on the circumference of the cylindrical portion on a tapered optrode, using ion beam proximity lithography and controlled high throughput approach of conformally deposited resist.

7.2 Future Work

Although plasmonic nanosensors presented in this work incorporate high improvements in the sensitivity for SERS, numerous applications still need to be explored. Synergistic fabrication of nanostructures on different substrate platforms enable them to be used for a range of applications requiring multiplex detection. These involve point of care applications, remote sensing applications in toxic and harsh environments, in-situ and in-vivo applications and applications demanding early diagnosis. Thus, exploring the range of applications for the sensors developed is regarded as the future work here.

The ability to fabricate optical fibers integrated with patterned gold sensors using a reliable and a high throughput approach of ion beam proximity lithography, has led us to believe in easier extension of the approach to Nanoporous plasmonic optical fiber sensors, patterned silver sensors and patterned alloy sensors. Optical fiber NPG sensors, due to the additional dimension of mesoporosity, can exhibit higher sensitivity than the conventional gold sensors. Lastly, an optical fiber with patterned structures containing silver would prove to be highly sensitive in the visible range as seen for silver nanostructures on planar substrates.

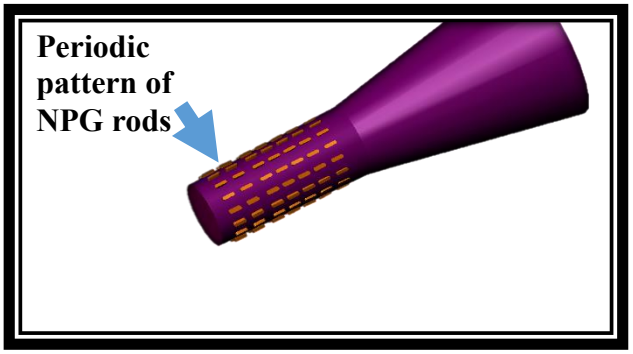

Figure 47 : Periodic arrays of NPG rods on hybrid tapered optical fibers with a large cylindrical area.

REFERENCES

1. Eric C. Le Ru and Pablo G. Etchegoin, "Single-Molecule Surface-Enhanced Raman Spectroscopy" *Annu. Rev. Phys. Chem.,* 63, pp. 65–87 (2012).
2. E. C. Le Ru, M. Meyer, and P. G. Etchegoin., "Proof of Single-Molecule Sensitivity in Surface Enhanced Raman Scattering (SERS) by Means of a Two-Analyte Technique" *J. Phys. Chem. B.*, 110, pp. 1944-1948 (2006).
3. Nie, S. M. & Emery, S. R., "Probing single molecules and single nanoparticles by surface- enhanced Raman scattering," *Science,* 275, pp. 1102–1106 (1997).
4. K. Kneipp, Y. Wang, H. Kneipp, L. T. Perelman, I. Itzkan, R. Dasari, and M. S. Feld, "Single molecule detection using surface-enhanced Raman scattering (SERS)," *Phys. Rev. Lett.*,78, pp. 1667- 1670 (1997).
5. Min Hu, Fung Suong Ou, Wei Wu, Ivan Naumov, Xuema Li, Alexander M. Bratkovsky, R. Stanley Williams, and Zhiyong Li, "Gold Nanofingers for Molecule Trapping and Detection" *Journal of the American Chemical Society*, 132(37), pp. 12820-12822 (2010).
6. Le Ru EC, Etchegoin PG., Principles of Surface Enhanced Raman Spectroscopy and Related Plasmonic Effects, (Elsevier, 2009).
7. Fleischmann M., Hendra P. J., McQuillan A. J., "Raman spectra of pyridine adsorbed at a silver electrode" *Chem. Phys. Lett.*, 26, pp. 163–166 (1974).
8. Jeanmaire D. L., Duyne R. P. Van, "Surface Raman electrochemistry. Part 1. Heterocyclic, aromatic and aliphatic amines adsorbed on the anodised silver electrode" *J. Electroanal. Chem.*, 84, pp. 1–20 (1977).

9. Albrecht M. G., Creighton J. A., "Anomalously intense Raman spectra of pyridine at a silver electrode" *J. Am. Chem. Soc.*,99, pp. 5215–5219 (1977).
10. S. L. Kleinman, R. R. Frontiera, A.-I. Henry, J. A. Dieringer and D. R. P. Van, "Creating, characterizing, and controlling chemistry with SERS hot spots " *Phys. Chem. Chem. Phys.*, 15, pp. 21–36, (2013).
11. M Fleischer, D Zhang, K Braun, S Jäger, R Ehlich, M Häffner, C Stanciu, J K H Hörber, A J Meixner and D P Kern, "Tailoring gold nanostructures for near-field optical applications," *Nanotechnology*, 21, 065301 (2010).
12. F. H. Scholes, T. J. Davis, K. C. Vernon, D. Lau, S. A. Furman, and A. M. Glenn, "A hybrid substrate for surface-enhanced Raman scattering spectroscopy: coupling metal nanoparticles to strong localised fields on a micro-structured surface," *J. Raman Spectrosc.*,43, 2, pp. 196–201 (2012).
13. J. Qi, P. Motwani, M. Gheewala, C. Brennan, J. C. Wolfe and W.-C. Shih, "Surface-enhanced Raman spectroscopy with monolithic nanoporous gold disk substrates," *Nanoscale*, 5, pp. 4105-4109 (2013).
14. C. V. Raman, K. S. Krishnan, "A New type of secondary radiation," *Nature*, 121, 501 (1928).
15. P. G. Etchegoin and E. C. Le Ru, "Basic Electromagnetic Theory of SERS in Surface-Enhanced Raman Spectroscopy: Analytical, Biophysical and Life Science Applications, ed. S. Schlücker, Wiley-VCH, Weinheim, Germany, pp. 1–38, (2011).
16. Schatz GC, Young MA, Van Duyne RP. , "Electromagnetic mechanism of SERS in Surface-Enhanced Raman Scattering: Physics and Applications," ed. K Kneipp,M Moskovits, H Kneipp, pp. 19–46. Berlin: Springer- Verlag (2006).

17. Stefan A. Maier, Plasmonics: Fundamentals and applications, (Springer, 2007).
18. Ricardo F. Aroca, "Plasmon enhanced spectroscopy," *Phys. Chem. Chem. Phys.*, 15, pp. 5355-5363 (2013).
19. P.L. Stiles, J.A. Dieringer, N.C. Shah, R.R. Van Duyne., "Surface-enhanced Raman spectroscopy," *Annual Review of Analytical Chemistry*,1, pp. 601(2008).
20. William L. Barnes, Alain Dereux and Thomas W. Ebbesen, "Surface plasmon subwavelength optics," *Nature*, 424, pp. 824-830 (2003).
21. K. Kneipp, H. Kneipp, I. Itzkan, R. R. Dasari, and M. S. Feld, "Surface-enhanced Raman scattering and biophysics" *J. Phys. Condens. Matter.,* 14, 18, pp. 597–624 (2002).
22. Stuart DA, Yonzon CR, Zhang X, Lyandres O, Shah NC, Glucksberg MR, Walsh JT, Van Duyne RP, "Glucose sensing using near-infrared surface-enhanced Raman spectroscopy: gold surfaces, 10-day stability, and improved accuracy," *Anal. Chem.*, 77, pp. 4013-4019 (2005).
23. Lyandres O., Shah NC., Yonzon CR., Walsh JT., Glucksberg MR., Van Duyne RP., "Real-time glucose sensing by surface-enhanced Raman spectroscopy in bovine plasma facilitated by a mixed decanethiol/mercaptohexanol partition layer," *Anal. Chem.*, 77, pp. 6134-6139 (2005).
24. Douglas A. Stuart, Jonathan M. Yuen, Nilam Shah,Olga Lyandres, Chanda R. Yonzon, Matthew R. Glucksberg, Joseph T. Walsh, and Richard P. Van Duyne, "In Vivo Glucose Measurement by Surface-Enhanced Raman Spectroscopy," *Analytical Chemistry*, 78 (20), pp. 7211-7215 (2006).

25. Stuart DA, Biggs KB, Van Duyne RP., "Surface-enhanced Raman spectroscopy of half-mustard agent," *Analyst*, 131, pp. 568-572 (2006).
26. Stokes DL, Alarie JP, Ananthanarayanan V, Vo-Dinh T., "Fiber optic SERS sensor for environmental monitoring," *Proc.SPIE.*, 3534, pp. 647-654 (1999).
27. Leona M., "Microanalysis of organic pigments and glazes in polychrome works of art by surface-enhanced Resonance Raman scattering," *PNAS*, 106, pp. 14757-14762 (2009).
28. Lau, D., Livett, M. & Prawer, S., "Application of Surface-enhanced Raman spectroscopy (SERS) to the analysis of natural resins in artworks," *Journal of Raman spectroscopy*, 39, pp. 545-552 (2008).
29. Chen, K., Leona, M. & Vo-Dinh, T., "Surface-enhanced Raman scattering for identification of organic pigments and dyes in works of art and cultural heritage material," *Sensor Review*, 27, pp. 109-120 (2007).
30. Feng S1, Lin J, Cheng M, Li YZ, Chen G, Huang Z, Yu Y, Chen R, Zeng H, "Gold nanoparticle based surface-enhanced Raman scattering spectroscopy of cancerous and normal nasopharyngeal tissues under near-infrared laser excitation," *Appl Spectrosc*, 63(10), pp. 1089-1094 (2009).
31. El-Ansary A1, Faddah LM, "Nanoparticles as biochemical sensors," *Nanotechnol Sci Appl.*, 3, pp. 65-76 (2010).
32. A. Campion and P. Kambhampati, "Surface-enhanced Raman scattering," *Chem. Soc. Rev.*, 27, pp. 241 (1998).
33. Kazuhiro Fukami, Mohamed L. Chourou, Ryohei Miyagawa, Álvaro Muñoz Noval, Tetsuo Sakka, Miguel Manso-Silván, Raúl J. Martín-Palma and Yukio H. Ogata,

"Gold Nanostructures for Surface-Enhanced Raman Spectroscopy, Prepared by Electrodeposition in Porous Silicon**,"** *Materials*,4, 4,pp. 791-800 (2011).

34. A. J. Haes, J. Zhao, S. Zou, C. S. Own, L. D. Marks, G. C. Schatz, and R. P. Van Duyne, "Solution-Phase, Triangular Ag Nanotriangles Fabricated by Nanosphere Lithography," *J. Phys. Chem. B.*,109, pp. 11158- 11162 (2005).
35. Osawa , M.; Ataka , K.; Yoshii, K.; Nishikawa , Y., "Surface-Enhanced Infrared Spectroscopy: The Origin of the Absorption Enhancement and Band Selection Rule in the Infrared Spectra of Molecules Adsorbed on Fine Metal Particles," *Appl. Spectrosc.*, *47*, pp. 1497-1502, (1993).
36. Doron-Mor, I., Barkay, Z., Filip-Granit, N., Vaskevich, A., and Rubinstein, I., "Ultrathin Gold Island Films on Silanized Glass. Morphology and Optical Properties," *Chem. Mater.*, 16, pp. 3476- 3483 (2004).
37. B. Chapman, Glow Discharge Processes: Sputtering and Plasma Etching, 2nd edition. (Wiley-Interscience, 1980).
38. Ji Qi, Pratik Motwani, Jianbo Zeng, John C. Wolfe, and Wei-Chuan Shih, "Morphological, plasmonic, and SERS characterization of DC-sputtered gold nanoislands," *Biomedical Spectroscopy and Imaging*, 4(1), pp. 95-103 (2015).
39. Lieberman, M. A., Lichtenberg, A. J., Principles of Plasma Discharges and Materials Processing, 2nd edition (Wiley-Interscience, 2005).
40. Mamdouh E. Abdelsalam, Philip N. Bartlett, Jeremy J. Baumberg, Suzanne Cintra, Tim A. Kelf, Andrea E. Russell**,** " Electrochemical SERS at a structured gold surface," *Electrochemistry Communications*, 7, pp. 740-744 (2005)

41. Eric Le Ru, Pablo Etchegoin, "Quantifying SERS enhancements," *MRS Bulletin*, 38, pp.631-640 (2013).
42. J. Qi, P. Motwani, J. C. Wolfe and W.-C. Shih, "High-throughput Raman and surface-enhanced Raman microscopy," *Proceedings of SPIE, San Francisco*, 2012.
43. E. Seker, Y. Berdichevsky, M. R. Begley, M. L. Reed, K. J. Staley and M. L. Yarmush, "The fabrication of low-impedance nanoporous gold multiple-electrode arrays for neural electrophysiology studies," *Nanotechnology*, 21, 125504, (2010).
44. C. L. Haynes, A. D. McFarland and R. P. Van Duyne, "Surface-Enhanced Raman Spectroscopy,"*Anal. Chem.*, 77,pp. 338A-346A (2005).
45. Jonah Erlebacher, Michael J. Aziz, Alain Karma, Nikolay Dimitrov and Karl Sieradzki, " Evolution of nanoporosity in dealloying," *Nature*, 410, pp. 450 (2001).
46. Xiuling Yan, Fanhui Meng, Yun Xie, Jianguo Liu, and Yi Ding, "Direct N2H4/H2O2 Fuel Cells Powered by Nanoporous Gold Leaves," *Scientific Reports*, 2,pp. 941 (2012).
47. Seker E, Gaskins J, Bart-Smith H, Zhu J, Reed M, Zangari G, Kelly R, Begley M, "The effects of post-fabrication annealing on the mechanical properties of freestanding nanoporous gold structures," *Acta Mater.*, 55, pp. 4593-4602 (2007).
48. Barry Paul Craver, "Neutral Particle Lithography," PhD dissertation, Department of ECE, University of Houston (2008).
49. Fang Yu, Stefanie Ahl, Anne-Marie Caminade, Jean-Pierre Majoral, Wolfgang Knoll, and Jonah Erlebacher, "Simultaneous Excitation of Propagating and Localized Surface Plasmon Resonance in Nanoporous Gold Membranes," *Anal. Chem.*, 78,pp. 7346 (2006).

50. L. Zhang, X. Lang, A. Hirata and M. Chen, "Wrinkled nanoporous gold films with ultrahigh surface-enhanced Raman scattering enhancement," *ACS Nano*, 5, 4407 (2011).

51. Y. Jiao, D. Ryckman, P. N. Ciesielski, C. A. Escobar, G. K. Jennings and S. M. Weiss, "Patterned nanoporous gold as an effective SERS template," *Nanotechnology*, 22, pp. 295302 (2011).

52. L. H. Qian and M. W. Chen, "Ultrafine nanoporous gold by low-temperature dealloying and kinetics of nanopore formation," A*pplied physics letters,* 91, 083105 (2007).

53. L. H. Qian, X. Q. Yan, T. Fujita, A. Inoue, and M. W. Chen, "Surface enhanced Raman scattering of nanoporous gold: Smaller pore sizes stronger enhancements," A*pplied physics letters,* 90, 153120 (2007).

54. S. O. Kucheyev, J. R. Hayes, J. Biener, T. Huser,b_ C. E. Talley, and A. V. Hamza, "Surface-enhanced Raman scattering on nanoporous Au," *Applied physics letters*, 89, 053102 (2006).

55. H. W. Deckman, J. H. Dunsmuir, "Natural lithography," *Appl. Phys. Lett.*,41, 377(1982).

56. R. C. Newman, S. G. Corcoran, J. Erlebacher, M. J. Aziz, and K. Sieradzki, "Alloy corrosion," *MRS Bulletin*, 24(7):24–28, 1999.

57. Neus G. Bastús, Joan Comenge, and Víctor Puntes, "Kinetically Controlled Seeded Growth Synthesis of Citrate-Stabilized Gold Nanoparticles of up to 200 nm: Size Focusing versus Ostwald Ripening," *Langmuir*, 27 (17), pp 11098–11105 (2011).

58. Jill E. Millstone, Wei Wei, Matthew R. Jones, Hyojong Yoo and Chad A. Mirkin, "Iodide Ions Control Seed-Mediated Growth of Anisotropic Gold Nanoparticles," *Nano Lett*., 8 (8), pp. 2526–2529 (2008).

59. Wenxin Niu, Shanliang Zheng, Dawei Wang, Xiaoqing Liu, Haijuan Li, Shuang Han, Jiuan Chen, Zhiyong Tang and Guobao Xu, "Selective Synthesis of Single-Crystalline Rhombic Dodecahedral, Octahedral, and Cubic Gold Nanocrystals," *J. Am. Chem. Soc.*, 131 (2), pp. 697–703 (2009).

60. Tapan K. Sau, Andrey L. Rogach,Markus Döblinger and Jochen Feldmann, "One-Step High-Yield Aqueous Synthesis of Size-Tunable Multispiked Gold Nanoparticles," *Small,* 7: 2188–2194 (2011).

61. Xia X, Zeng J, Zhang Q, Moran CH, Xia Y., "Recent Developments in Shape-Controlled Synthesis of Silver Nanocrystals," *J Phys Chem C Nanomater Interfaces*, 116(41), pp. 21647-21656 (2012).

62. Ji Qi and Wei-Chuan Shih, "Performance of line-scan Raman microscopy for high-throughput chemical imaging of cell population," *Applied Optics,* 53(13), pp. 2881-2885 (2014).

63. Jung-Sub Wi, Satoshi Tominaka, Kohei Uosaki and Tadaaki Nagao, "Porous gold nanodisks with multiple internal hot spots," *Phys. Chem. Chem. Phys.*, 14, pp. 9131–9136 (2012).

64. John C. Hulteen and Richard P. Van Duyne, "Nanosphere lithography: A materials general fabrication process for periodic particle array surfaces," *J. Vac. Sci. Technol. A*, 13(3), pp. 1553-1558 (1995).

65. Darren J. Lipomi , Ramses V. Martinez , Mikhail A. Kats , Sung H. Kang , Philseok Kim , Joanna Aizenberg , Federico Capasso , and George M. Whitesides, "Patterning the Tips of Optical Fibers with Metallic Nanostructures Using Nanoskiving," *Nano Lett.*, 11(2), pp. 632-636 (2011).
66. G. Kostovski, D.J. White, A Mitchell, MW Austin, PR Stoddart, "Nanoimprinted optical fibres: Biotemplated nanostructures for SERS sensing," *Biosensors and Bioelectronics,* 24 (5), pp. 1531-1535 (2009).
67. K. Totsu , Y. Haga , M. Esashi , "Ultra-miniature fiber-optic pressure sensor using white light interferometry," *J. Micromech. Microeng.*,15 , pp. 71-75 (2005).
68. N. Ma , P. C. Ashok , D. J. Stevenson , F. J. Gunn-Moore , K. Dholakia, "Integrated optical transfection system using a microlens fiber combined with microfluidic gene delivery," *Biomed.Opt. Expr.,* 1 , pp. 694-705 (2010).
69. K. Deisseroth, "Optogenetics," *Nature Methods,* 8, 1, pp. 26-29 (2011).
70. C. Pang , F. Gesuele , A. Bruyant , S. Blaize , G. Lérondel , P. Royer , "Enhanced light coupling in sub-wavelength single-mode silicon on insulator waveguides," *Opt Express.*, 17(9), pp. 6939-6945 (2009).
71. S. Cabrini , C. Liberale , D. Cojoc , A. Carpentiero , M. Prasciolu , S. Mora , V. Degiorgio , F. De Angelis , E. Di Fabrizio, "Axicon lens on optical fiber forming optical tweezers, made by focused ion beam milling," *Microelectronic Engineering*, 83, pp. 804-807 (2006).
72. Claire Gu, Chao Shi, He Yan, Debraj Ghosh, Leo Seballos, Shaowei Chen, Jin Z. Zhang, "Recent advance in fiber SERS sensors," *Proc. SPIE 7056, Photonic Fiber*

and Crystal Devices: Advances in Materials and Innovations in Device Applications II, 7056, pp. 70560H-1-70560H-12 (2008).

73. P. R. Stoddart and D. J. White, "Optical fibre SERS sensors," *Anal Bioanal Chem.*, 394, pp. 1761–1774 (2009).
74. Ken I. Mullen and Keith T. Carron, "Surface-Enhanced Raman Spectroscopy with Abrasively Modified Fiber Optic Probes," *Analytical Chemistry*, 63, pp. 2197-2199 (1991).
75. Stokes, D.L.; Vo-Dinh, T, "Development of an integrated single-fiber SERS sensor," *Sens. Actuat.B-Chem.*, 69, pp. 28-36 (2000).
76. Carmen Viets and Wieland Hill, "Laser Power Effects in SERS Spectroscopy at Thin Metal Films," *J. Phys. Chem. B*, 105, pp. 6330-6336 (2001).
77. C. Viets, W. Hill, "Comparison of fibre-optic SERS sensors with differently prepared tips," *Sensors and Actuators B: Chemical*, 51, pp. 92-99 (1998).
78. E. Polwart , R. L. Keir , C. M. Davidson , W. E. Smith , D. A. Sadler, "Novel SERS-Active Optical Fibers Prepared by the Immobilization of Silver Colloidal Particles," *Applied Spectroscopy*, 54, pp. 522-527 (2000).
79. Ting Liu, Lei Zhou, Zhonghuan Zhang, Xiaosheng Xiao, Minjuan Zhou, Changxi Yang, "Combined taper-and-cylinder optical fiber probes for highly sensitive surface-enhanced Raman scattering," *Appl. Phys. B*,116, pp. 799–803 (2014).
80. Raoul Stockle, Christian Fokas, Volker Deckert, Renato Zenobia, Beate Sick, Bert Hecht, and Urs P. Wild, "High-quality near-field optical probes by tube etching," *Appl. Phys. Lett.*, 75(2), pp. 160-162 (1999).

81. Dhara Parikh, "Microelectrode Cuff for Neuronal Sensing in the Locust," Master's thesis, Department of ECE, University of Houston (2007).